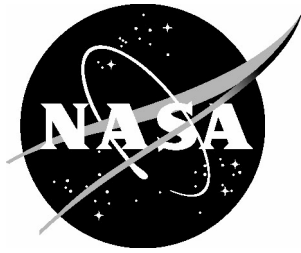# Motion Cueing Algorithm Development: Human-Centered Linear and Nonlinear Approaches

Robert J. Telban and Frank M. Cardullo
State University of New York, Binghamton, New York

Since its founding, NASA has been dedicated to the advancement of aeronautics and space science. The NASA Scientific and Technical Information (STI) Program Office plays a key part in helping NASA maintain this important role.

The NASA STI Program Office is operated by Langley Research Center, the lead center for NASA's scientific and technical information. The NASA STI Program Office provides access to the NASA STI Database, the largest collection of aeronautical and space science STI in the world. The Program Office is also NASA's institutional mechanism for disseminating the results of its research and development activities. These results are published by NASA in the NASA STI Report Series, which includes the following report types:

- TECHNICAL PUBLICATION. Reports of completed research or a major significant phase of research that present the results of NASA programs and include extensive data or theoretical analysis. Includes compilations of significant scientific and technical data and information deemed to be of continuing reference value. NASA counterpart of peer-reviewed formal professional papers, but having less stringent limitations on manuscript length and extent of graphic presentations.

- TECHNICAL MEMORANDUM. Scientific and technical findings that are preliminary or of specialized interest, e.g., quick release reports, working papers, and bibliographies that contain minimal annotation. Does not contain extensive analysis.

- CONTRACTOR REPORT. Scientific and technical findings by NASA-sponsored contractors and grantees.

- CONFERENCE PUBLICATION. Collected papers from scientific and technical conferences, symposia, seminars, or other meetings sponsored or co-sponsored by NASA.

- SPECIAL PUBLICATION. Scientific, technical, or historical information from NASA programs, projects, and missions, often concerned with subjects having substantial public interest.

- TECHNICAL TRANSLATION. English-language translations of foreign scientific and technical material pertinent to NASA's mission.

Specialized services that complement the STI Program Office's diverse offerings include creating custom thesauri, building customized databases, organizing and publishing research results ... even providing videos.

For more information about the NASA STI Program Office, see the following:

- Access the NASA STI Program Home Page at *http://www.sti.nasa.gov*

- E-mail your question via the Internet to help@sti.nasa.gov

- Fax your question to the NASA STI Help Desk at (301) 621-0134

- Phone the NASA STI Help Desk at (301) 621-0390

- Write to:
  NASA STI Help Desk
  NASA Center for AeroSpace Information
  7121 Standard Drive
  Hanover, MD 21076-1320
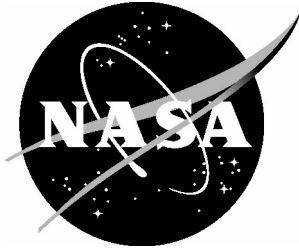
Motion Cueing Algorithm Development: Human-Centered Linear and Nonlinear Approaches

Robert J. Telban and Frank M. Cardullo
State University of New York, Binghamton, New York

Acknowledgments

Jacob Houck of the Flight Simulation and Software Branch at the NASA Langley Research Center assisted in the preparation of this report.

Abstract

While the performance of flight simulator motion system hardware has advanced substantially, the development of the motion cueing algorithm, the software that transforms simulated aircraft dynamics into realizable motion commands, has not kept pace. Prior research identified viable features from two algorithms: the nonlinear "adaptive algorithm", and the "optimal algorithm" that incorporates human vestibular models. A novel approach to motion cueing, the "nonlinear algorithm" is introduced that combines features from both approaches. This algorithm is formulated by optimal control, and incorporates a new integrated perception model that includes both visual and vestibular sensation and the interaction between the stimuli. Using a time-varying control law, the matrix Riccati equation is updated in real time by a neurocomputing approach.

Preliminary pilot testing resulted in the optimal algorithm incorporating a new otolith model, producing improved motion cues. The nonlinear algorithm vertical mode produced a motion cue with a time-varying washout, sustaining small cues for longer durations and washing out large cues more quickly compared to the optimal algorithm. The inclusion of the integrated perception model improved the responses to longitudinal and lateral cues. False cues observed with the NASA adaptive algorithm were absent. The neurocomputing approach was crucial in that the number of presentations of an input vector could be reduced to meet the real time requirement without degrading the quality of the motion cues.

The new cueing algorithms are implemented on the NASA Langley Visual Motion Simulator (VMS), and will ultimately be implemented on the new Cockpit Motion Facility (CMF) currently being erected at NASA Langley.

Table of Contents

List of Tables

This page intentionally left blank.

List of Figures

Nomenclature

Symbols

a	acceleration $\mathbf{a} = \begin{bmatrix} a_x & a_y & a_z \end{bmatrix}^{\mathbf{T}}$
A_0, B_0, B_1	otolith sensation model break frequencies
$\mathbf{A_j}$	coordinates of the upper bearing block of the j-th actuator
$\mathbf{B_j}$	coordinates of the lower bearing block of the j-th actuator
A, B, C, D, H	matrices of the state-space model of a control system
$\mathbf{A'}$	system matrix of the standard form optimal control system
c_0, c_1, c_2, c_3	coefficients of the nonlinear scaling polynomial
$d, e, \delta, \gamma, \lambda$	NASA adaptive algorithm washout parameters
$E\{\ \}$	mathematical mean of a statistical variable
E	objective function or energy norm for neurocomputing approach
e	pilot sensation error
Fr	reference frame
f	specific force
$\hat{f}$	sensed specific force
G_O, G_S	gain sensitivities in the otolith and semicircular canals models
G	turbulence gust vector $\mathbf{G} = \begin{bmatrix} p_G & q_G & r_G & u_G & v_G & w_G \end{bmatrix}^{\mathbf{T}}$
g	acceleration due to gravity
H_G	augmented turbulence transfer function
J	system cost function
K	state feedback gain matrix

K_{sub}	NASA adaptive algorithm steepest descent parameters
l_j	length of the j-th motion platform actuator
$\mathbf{L_{SI}}$	transformation matrix from simulator into inertial frame
$\mathbf{P}$	solution of the algebraic Riccati equation
$\mathbf{Q}, \mathbf{R}, \mathbf{R_d}$	weighting matrices in a cost function (tracking form)
$\mathbf{Q_2}$	weighting matrix for nonlinear algorithm control law
$\mathbf{R_1'}, \mathbf{R_2}, \mathbf{R_{12}}$	weighting matrices in a cost function (standard form)
$\mathbf{R}$	radius vector
$\mathbf{S}$	simulator centroid displacement
s	Laplace variable
s_0, s_1	slopes of the nonlinear gain polynomial
$\mathbf{T_S}$	transformation matrix from angular velocity to Euler angle rates
T_0, T_1, T_2, T_3, T_4	coefficients in the semicircular canal sensation model
$\mathbf{u}$	input to a control system
$\mathbf{u'}$	input to the standard form optimal control system
$\mathbf{v}$	error output of neurocomputing solver
$\mathbf{w}$	white noise
$\mathbf{W(s)}$	optimal algorithm transfer function matrix
$\mathbf{x}$	system state vector
$\mathbf{y}$	desired state space system output
$\mathbf{z}$	excitatory input signal for neurocomputing system
α	prescribed degree of nonlinearity for nonlinear algorithm
$\boldsymbol{\beta}$	Euler angles $\boldsymbol{\beta} = \begin{bmatrix} \phi & \theta & \psi \end{bmatrix}^{\mathbf{T}}$

δ	pilot control input vector
γ	filtered white noise break frequency
μ	learning parameter for neurocomputing solver
τ	time constants in the semicircular and otolith sensation models
ρ	density of the otoconial membrane
$\boldsymbol{\omega}$	angular velocity about the body frame $\boldsymbol{\omega} = \begin{bmatrix} p & q & r \end{bmatrix}^{\mathrm{T}}$
$\hat{\boldsymbol{\omega}}$	sensed angular velocity

Subscripts

Subscripts indicate to what the main symbol is related.

$(\ )_A$	aircraft
$(\ )_{CG}$	center of gravity of aircraft
$(\ )_d$	simulator states included in the cost function
$(\ )_e$	sensation or perceptual error
$(\ )_I$	inertial reference frame
$(\ )_j$	j-th actuator of the motion platform
$(\ )_n$	white noise input states
$(\ )_{OTO}$	otolith model
$(\ )_{PS}$	pilot in the simulator
$(\ )_S$	simulator
$(\ )_{SR}$	simulator rotation
$(\ )_{SCC}$	semicircular canals sensation model
$(\ )_{ST}$	simulator tilt coordination channel
$(\ )_V$	pilot's vestibular model

$(\ )_{\text{VEST}}$ human vestibular system

$(\ )_{\text{VIS}}$ human visual system

$(\ )_{x,y,z}$ x,y, or z component

$(\ )_{\alpha}$ relates to system with nonlinearity

Superscripts

Superscripts indicate which reference frame the main symbol is in

$(\ )^{A}$ in aircraft reference frame Fr_A

$(\ )^{I}$ in inertial reference frame Fr_I

$(\ )^{S}$ in simulator reference frame Fr_S

1. Introduction

1.1. Effect of Simulator Motion on Human Performance

The objective of a motion system, when used in conjunction with a visual system, is to stimulate the pilot so that he or she can perceive the required motion and force information (i.e., cues) necessary to fly the simulator within the same performance and control activity as the actual aircraft. An example of a motion system is the six-degree-of-freedom hexapod shown in Figure 1.1.

Figure 1.1. Six-Degree-of-Freedom Hexapod Motion System. Delft University, The Netherlands.

Buckingham [1] reported that the inclusion of motion cues allows the pilot to become aware of the aircraft response before visual cues are detected, noting that without motion cues, the pilot's perception of motion is degraded and the aircraft feels slower in responding. Buckingham noted that in extreme cases, the pilot might be unable to control the aircraft when the absence of motion cues introduces a 90-degree phase lag into the control loop. Buckingham cited one case in which the motion system was disabled while

1

unbeknown to the pilot; the pilot described the simulation as inferior to the previous configuration with motion, as it took longer to respond to control inputs.

Gundry [2] reported that Douvillier, et al., Fedderson, Mathney, Perry and Naish, and Tremblay, et al. observed that when motion cues were provided, there was an increase in high-frequency, low-amplitude control movements that appeared more like movements observed during flight as compared to activity in a fixed-base simulator. Gundry noted that Perry and Naish compared pilot control activity of both fixed-base and moving-base simulation of a flight through heavy turbulence, and observed a considerable reduction in the simulated aircraft roll angle with motion present. The presence of motion produced pilot responses with more rapid and accurate control. These results show that when an aircraft is subjected to turbulence in flight, the pilot uses roll and pitch motion as information to correct the aircraft attitude. It was observed that platform motion in response to external disturbances and maneuvering allowed the operator to control the simulator using sensory cues similar to those used in flight.

Gundry also reported that Dinsdale, Meiry, Shirley, and Stapleford investigated the effects of roll motion upon compensatory tracking error. In these investigations, the presence of motion was observed to reduce the phase lag of the simulated aircraft roll angle relative to the command input, increase mid-frequency gain and crossover frequency, and reduce the size of the remnant. This showed that the presence of roll motion cues provide the operator with lead information that is used to track the disturbance input more accurately, especially at frequencies greater than 0.5 Hz (as noted by Shirley).

Scanlon [3] conducted a piloted simulation study on the NASA Langley Visual Motion System to determine the effects of motion cues during the performance of complex curved approach and landing tasks in the signal environment of the Microwave Landing System (MLS). Comparisons of pilot tracking performance and workload were made on approach tasks of low, medium, and high complexity conducted with and without motion, with and without turbulence, and with three different wind models. With motion cues, smaller lateral tracking errors resulted for the most complex approach in the presence of wind and turbulence. The effect of motion was insignificant for lateral tracking errors for low and medium complexity approaches, and for vertical tracking error for all levels of complexity. Motion cues, most noticeably with turbulence, yielded a higher physical workload as measured by pilot control activity, with higher column and wheel input rates measured for all levels of task complexity. All pilots indicated a preference for motion over no motion, commenting that flying was easier and more realistic with the addition of motion.

Schroeder [4] conducted an evaluation on the NASA Ames Vertical Motion System with experienced test pilots performing single-axis vertical and directional (yaw) maneuvers of a hovering helicopter with varying degrees of fidelity in the motion cueing algorithm, i.e., from nearly full motion to fixed-base. For the vertical maneuver full-motion case, Schroeder reported that "well-damped, accurate bob-ups are achieved with the vertical velocity staying within 10 ft/s", but for the fixed-base case, the pilot had to adjust his compensation with the remaining cues, recovering over time, but taking longer to achieve final repositioning. Schroeder noted that the pilots were "stunned" by the total loss of motion, reporting that motion cues were "certainly perceived" by all pilots for all

test conditions with motion cues, but not with the fixed-base configuration. Schroeder commented, "Until the value of motion was demonstrated, pilot subjective impression was that the vertical task was primarily visual". Schroeder reported for the directional maneuver, no performance degradation was noticed for the fixed-base case, noting that visual yaw cues, depending on the visual scene, may be very compelling in inducing motion perception, possibly overwhelming the yaw motion stimulus.

Hall [5] noted that platform motion remains the only currently available technology that can provide motion cueing of both direction and magnitude without requiring additional learning, because the pilot's proprioceptive sensors are stimulated in the short term in the same manner as in flight. The presence of motion will allow the pilot to achieve a task closer to that seen in the aircraft since he uses a similar set of sensory cues, especially when forced to operate in a high gain manner. Hall then summarizes that motion becomes less important when the vehicle is easy to fly, the task can be performed with low pilot workload and gain, and disturbance motion is either absent or does not require corrective action. Platform motion becomes increasingly important as task difficulty and pilot control gain increase, and are essential in the absence of good, wide field of view visual cues (e.g., flying in clouds, at night), and necessary for high gain tasks even with strong visual cues. Hall concluded that motion cueing is essential when a pilot must either react quickly in response to an unexpected disturbance, or when the pilot must control a vehicle with low stability.

1.2. Vehicle Simulation Structure

The vehicle simulation structure for a motion system is shown in Figure 1.2. The operator control inputs drive a mathematical model of the vehicle dynamics, generating

the vehicle states. Passing the vehicle states through the motion cueing algorithm produces the desired motion cues and platform states. The desired platform states are then transformed from degree-of-freedom space to actuator space, generating the realized commands to the six actuators. The actuator motion commands serve as input to the platform dynamics, resulting in the actual simulator motion.

```
┌──────────────┐          ┌──────────────────┐
│  Simulator   │─────────▶│ Vehicle Dynamics │
│ Control Input│          │      Model       │
└──────────────┘          └──────────────────┘
                                   │
                                   │  Vehicle States
                                   ▼
                          ┌──────────────────┐
                          │  Motion Cueing   │
                          │    Algorithm     │
                          └──────────────────┘
                                   │
                                   │  Desired
                                   │  Platform States
                                   ▼
                          ┌──────────────────┐
                          │    Kinematic     │
                          │ Transformation   │
                          └──────────────────┘
                                   │
                                   │  Actuator Extension
                                   │  Commands
                                   ▼
                          ┌──────────────┐      ┌──────────────┐
                          │   Platform   │─────▶│   Platform   │
                          │   Dynamics   │      │    Motion    │
                          └──────────────┘      └──────────────┘
```
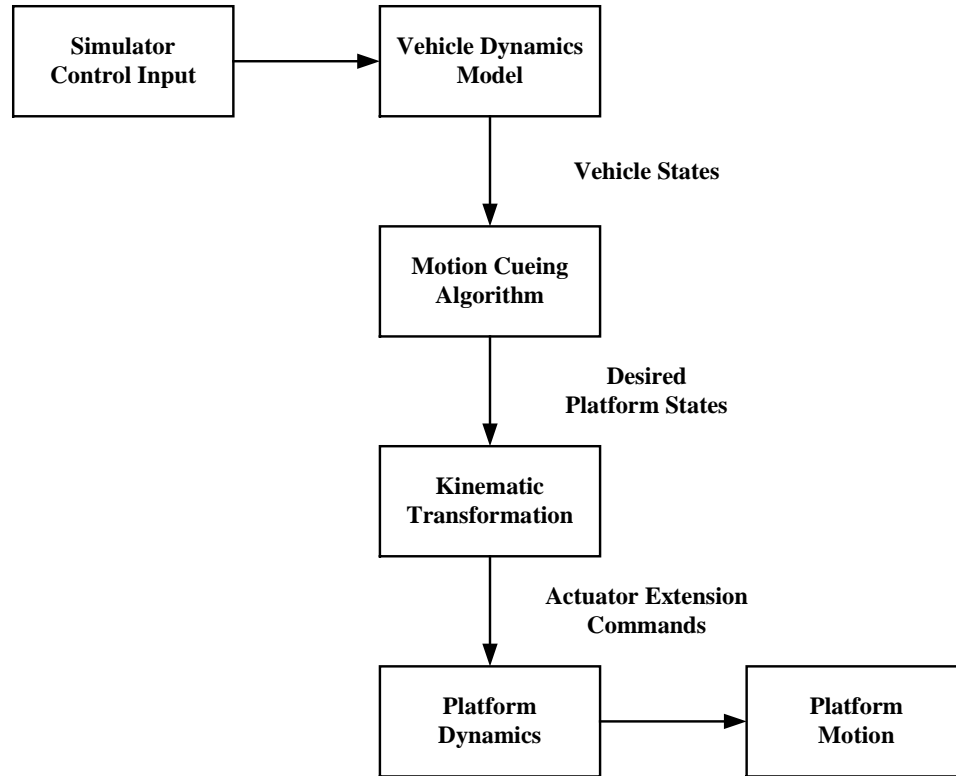
Figure 1.2. Vehicle Simulation Structure.

The motion cueing algorithm generates the desired motion cues that are constrained within the physical limits of the motion system. Figure 1.3 shows a typical motion cueing algorithm implementation. Vehicle states are transformed from a body reference frame to an inertial reference frame. Scaling and limiting the vehicle states reduces the magnitude of the motion cues. The duration of the cues are limited by the physical dimensions of the motion system. A method to overcome this limitation is a

technique known as "washout". Washout involves returning the platform state to a neutral position following the initial, or "onset" portion of a motion cue, thus "washing out" the resulting cue at levels below the pilot's perceptual threshold. This is accomplished by passing the vehicle state through a high-pass filter, removing long-duration (low-frequency) motion components. Figure 1.4 shows the response of a high-pass washout filter to an acceleration ramp to step input.
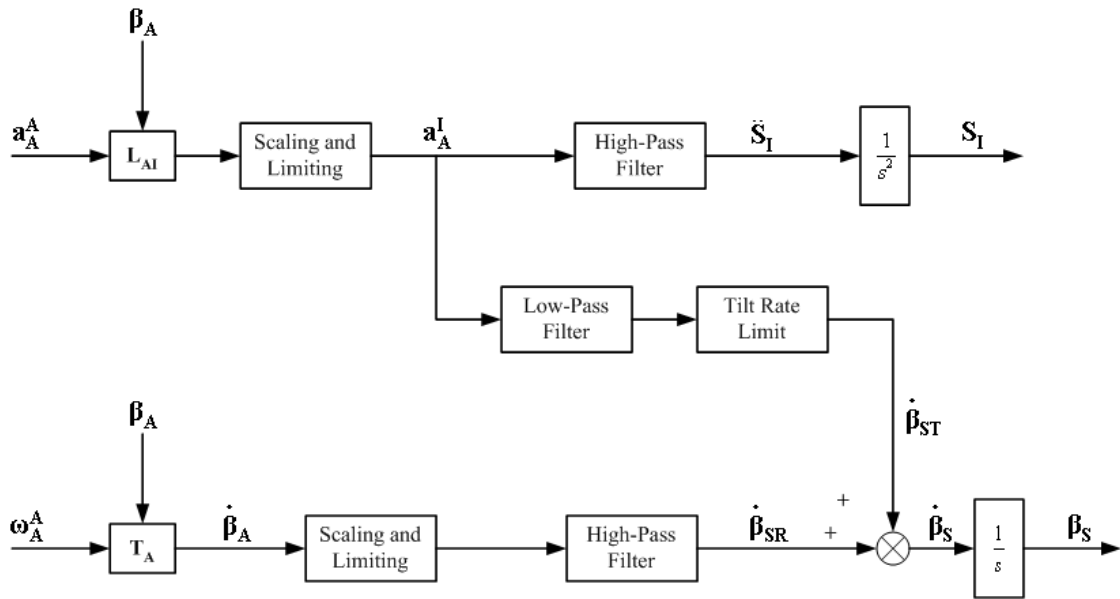
Figure 1.3. Motion Cueing Algorithm Implementation.

The otolith organs in the human vestibular system sense both acceleration and tilting of the pilot's head with respect to the gravity vector. Since the otoliths cannot discriminate between acceleration and tilt, this phenomenon, known as tilt coordination, can be used to advantage in motion simulation. For long-term specific force simulation, tilting the motion platform at a rate below the pilot's perceptual threshold augments the short-duration acceleration cues produced by high-pass washout filters. This additional cue results from passing the vehicle acceleration through a low-pass filter to produce the desired long-duration tilt cue. Tilt coordination is implemented in a motion cueing

6

algorithm by adding additional cross-feed channels with low-pass filters in the longitudinal (pitch/surge) and lateral (roll/sway) modes that produce the additional rotational cues as shown in Figure 1.3. For this reason four separate modes are implemented in a motion cueing algorithm: longitudinal, lateral, yaw, and heave.
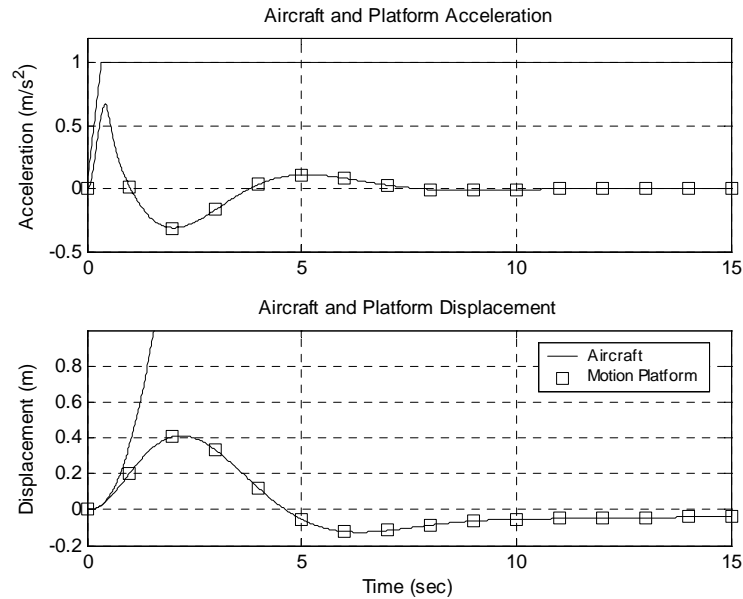
Figure 1.4. Response of a High-Pass Washout Filter to a Ramp to Step Input.

1.3. Scope of Research

In recent years, the performance of the hardware used to create the sensation of motion in flight simulators has improved substantially. However, development of the motion cueing algorithm, the software that transforms the simulated aircraft dynamics into realizable commands to the motion system hardware, has not kept pace with the hardware development. Wu and Cardullo [6] reported that early approaches to motion cueing using simple (first- and second-order) linear washout filters, for which the ratio of onset to washout duration was fixed, resulted in poor motion cues. This was a consequence of the ratios of onset to washout duration and magnitude being fixed,

thereby limiting the duration of low-magnitude cues to that of the maximum cue. In addition, most existing algorithms are oriented towards minimizing the state error between the aircraft and simulator rather than the perceptual error between the aircraft and simulator pilot. Wu and Cardullo [6] identified the two most viable approaches to motion cueing, the nonlinear "adaptive algorithm", for which the ratios of onset to washout duration and magnitude vary with time, and the linear, human-centered "optimal algorithm".

The coordinated adaptive washout algorithm, or "adaptive algorithm" was developed at NASA [7]. The objective of this algorithm is to adjust the motion platform response based upon its current motion states by adjusting filter gains through a process of minimizing a cost function in real time. The cost function is minimized by continuously adjusting a set of adaptive parameters by the method of steepest descent. This technique has at its basis the minimization of state error between the aircraft and simulator. This algorithm is described in further detail in Section 2.7.

The "optimal algorithm" was developed by Sivan, et al. [8], and later implemented at the University of Toronto Institute of Aerospace Studies (UTIAS) [9, 10]. This algorithm uses higher-order linear filters that are developed, prior to real time implementation, using optimal control methods. This method incorporates a mathematical model of the human vestibular system, constraining the pilot sensation error between the simulated aircraft and motion platform dynamics. Wu and Cardullo [6] reported that the optimal algorithm showed the most potential for future research, although the time-varying feature of the adaptive algorithm was also desirable.

A primary component in motion simulator design is the determination of the motion information that is relevant to the task and has an impact on human performance. This requires knowledge of human motion perception that, when integrated in the cueing algorithm development can provide the most necessary and beneficial motion cues. To that end, an integral part of this research involved the modeling of the human vestibular and perceptual systems. Literature studies in motion sensation and the vestibular system have been conducted to develop vestibular system sensation models that are most consistent with both experimental and theoretical analyses. New models of both the semicircular canals and the otoliths are proposed. Literature studies of the characteristics of visually induced motion sensation and the visual-vestibular interaction have also been conducted. A new integrated human perception model is proposed that includes both visual and vestibular sensation and incorporates the interaction between the stimuli.

The new vestibular models are incorporated in an improved development of the linear optimal algorithm. The development of this algorithm is presented along with results that demonstrate the effects of implementing the new vestibular models. The nonlinear algorithm is a novel approach to motion cueing that combines features of the nonlinear adaptive and linear optimal algorithms. This algorithm incorporates the human vestibular models along with the new integrated human perception model. The algorithm is formulated as an optimal control problem with a nonlinear control law, resulting in a set of nonlinear cueing filters that are adjusted in real time based on the motion platform states. A neurocomputing approach to solve the matrix Riccati equation in real time is discussed. Responses to single degree-of-freedom aircraft inputs for the nonlinear

algorithm are presented in comparison with the NASA adaptive algorithm and the optimal algorithm.

2. Background Information

2.1. NASA Langley Visual Motion Simulator (VMS)

The NASA Langley Visual Motion Simulator (VMS), shown in Figure 2.1, is a general-purpose flight simulator consisting of a two-crewmember cockpit mounted on a 60-inch stroke six-degree-of-freedom synergistic motion base [11], [12].

Figure 2.1. NASA Langley Visual Motion Simulator (VMS). NASA Langley Research Center, Hampton, Virginia.

Motion cues are provided in the simulator by the extension or retraction of the six hydraulic actuators of the motion base relative to the simulator neutral position. The NASA adaptive algorithm and the new optimal and nonlinear algorithms were used to drive the motion base during the tuning of the new algorithms and the piloted test evaluation.

The cockpit of the VMS, shown in Figure 2.2, is designed to accommodate a generic transport aircraft configuration on the left side and a generic fighter or rotorcraft configuration on the right side. Both sides of the cockpit are outfitted with three heads-down CRT displays (primary flight display, navigation/map display, and engine display), a number of small standard electromechanical circular instruments and a landing gear handle mounted in the instrument panel. The left side contains a two-axis side stick

control loader, and the right side contains a control loaded two-axis center stick. Both sides contain control loaded rudder systems. The center aisle stand is outfitted with a control display unit, a four-lever throttle quadrant, a flap handle, a speed brake handle, and a slats handle. The cockpit is outfitted with four collimated window display systems to provide an out-the-window visual scene. During the piloted evaluations, the test subject flew from the left seat, while an observer/test conductor rode in the right seat.

Figure 2.2. Visual Motion Simulator Cockpit. NASA Langley Research Center, Hampton, Virginia.

The simulator includes a high fidelity, highly nonlinear mathematical model of a Boeing 757-200 aircraft, complete with landing gear dynamics, gust and wind models, flight management systems, and flight control computer systems. For this study, the test subjects flew the simulated aircraft in the manual control mode (without the autopilot), and with manual throttle control (without the autothrottle).

The out-the window visual scene is driven by an Evans and Sutherland ESIG 3000/GT computer generated image system. The visual database represented the Dallas/Fort Worth airport and its surrounding terrain. The study utilized runways 18L and 18R for approach maneuvers and runway 18R for takeoff maneuvers. The runways were equipped with approach lights, precision approach path indicator lights, runway

markings, and signage. The database included all runways and taxiways, and all airport structures and buildings. All tests were conducted in a daylight environment with full visibility.

2.2. Reference Frames

A series of reference frames are used in the definition of the motion cueing algorithms. These reference frames are defined below and are shown in Figure 2.3.

2.2.1. *Aircraft Center of Gravity*

The aircraft center of gravity reference frame Fr_{CG} has its origin at the center of gravity of the aircraft. Frame Fr_{CG} has an orientation for X_{CG}, Y_{CG}, and Z_{CG} that is parallel to reference frames Fr_S and Fr_A.

2.2.2. *Simulator*

The simulator reference frame Fr_S has its origin at the centroid of the simulator payload platform, i.e. the centroid of the upper bearing attachment points. The origin is fixed with respect to the simulator payload platform. X_S points forward and Z_S points downward with respect to the simulator cockpit, and Y_S points toward the pilot's right hand side. The x-y plane is parallel to the floor of the cockpit.

2.2.3. *Aircraft*

The aircraft reference frame Fr_A has its origin at the same relative cockpit location as the simulator reference frame Fr_S. Fr_A has the same orientation for X_A, Y_A, and Z_A with respect to the cockpit as the simulator frame Fr_S.

2.2.4. Inertial

The inertial reference frame Fr_I is earth-fixed with Z_I aligned with the gravity vector **g**. Its origin is located at the center of the fixed platform motion base. X_I points forward and Y_I points to the right hand side with respect to the simulator pilot.

2.2.5. Reference Frame Locations

In Figure 2.3 are four vectors that define the relative location of the reference frames. R_I defines the location of Fr_S with respect to Fr_I. R_S defines the location of Fr_{PS} with respect to Fr_S. Similarly, R_A defines the location of Fr_{PA} with respect to Fr_A, where $R_A = R_S$. R_{CG} defines the location of Fr_A with respect to Fr_{CG}.
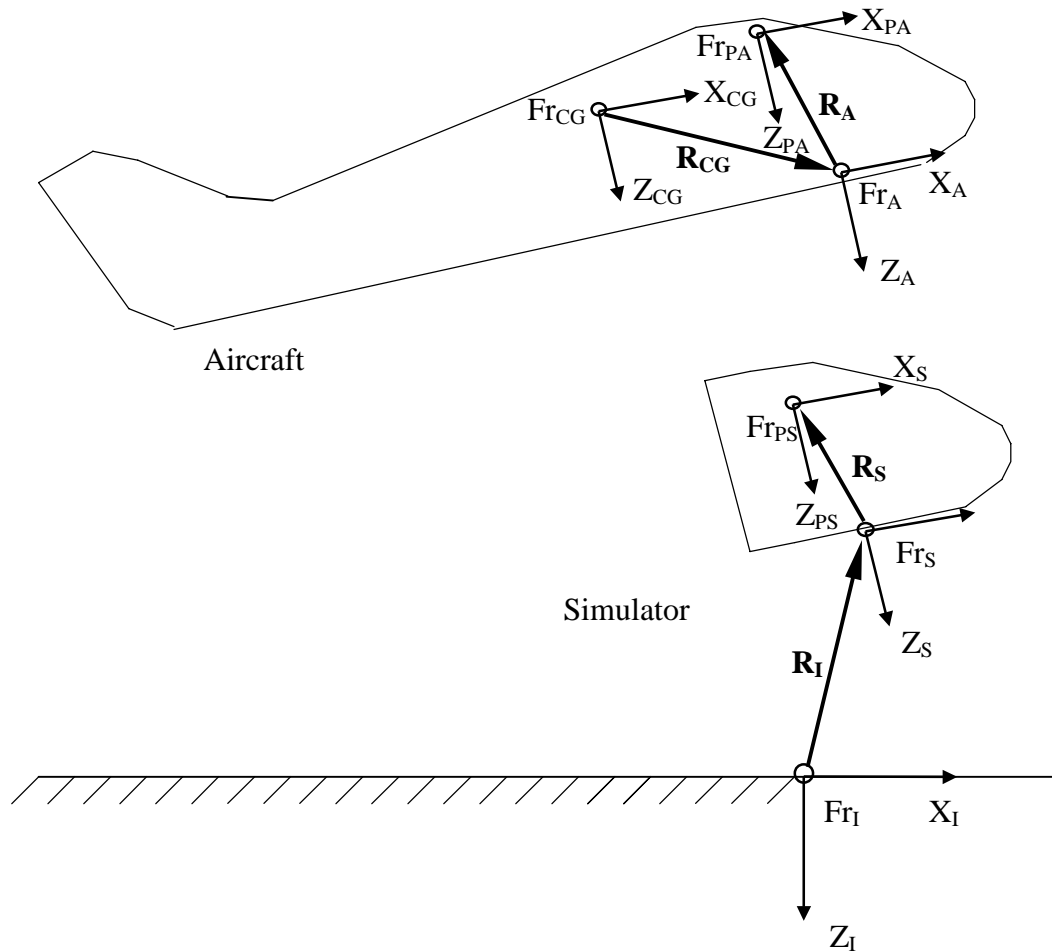
Figure 2.3. Reference Frame Locations. Adapted from Wu [13].

14

2.3. Coordinate Transformations

The orientation between the body-fixed simulator reference frame Fr_S and the inertial reference frame Fr_I can be specified by three Euler angles: $\boldsymbol{\beta} = [\phi \ \theta \ \psi]^T$ that define a sequence of rotations that carry Fr_S into Fr_I. A vector $\mathbf{V}$ expressed in the two frames can be related by the transformation matrix $\mathbf{L_{IS}}$ (Fr_I to Fr_S) or $\mathbf{L_{SI}}$ (Fr_S to Fr_I), with $\mathbf{V^S} = \mathbf{L_{IS}}\mathbf{V^I}$ and $\mathbf{V^I} = \mathbf{L_{SI}}\mathbf{V^S}$, where $\mathbf{L_{IS}} = \mathbf{L_{SI}^{-1}} = \mathbf{L_{SI}^T}$, and

$$\mathbf{L_{SI}} = \begin{bmatrix} \cos\theta\cos\psi & \sin\phi\sin\theta\cos\psi - \cos\phi\sin\psi & \cos\phi\sin\theta\cos\psi + \sin\phi\sin\psi \\ \cos\theta\sin\psi & \sin\phi\sin\theta\sin\psi + \cos\phi\cos\psi & \cos\phi\sin\theta\sin\psi - \sin\phi\cos\psi \\ -\sin\theta & \sin\phi\cos\theta & \cos\phi\cos\theta \end{bmatrix}. \tag{2.1}$$

The angular velocity of Fr_S with respect to Fr_I can be related to the Euler angle rates $\dot{\boldsymbol{\beta}}$ by the following expression. Let $\boldsymbol{\omega}_S^S$ represent the components of this angular velocity in frame Fr_S, then $\dot{\boldsymbol{\beta}} = \mathbf{T_S}\,\boldsymbol{\omega}_S^S$, where

$$\mathbf{T_S} = \begin{bmatrix} 1 & \sin\phi\tan\theta & \cos\phi\tan\theta \\ 0 & \cos\phi & -\sin\phi \\ 0 & \sin\phi\sec\theta & \cos\phi\sec\theta \end{bmatrix}, \tag{2.2}$$

and $\boldsymbol{\omega}_S^S = \mathbf{T_S^{-1}}\,\dot{\boldsymbol{\beta}}$, where

$$\mathbf{T_S^{-1}} = \begin{bmatrix} 1 & 0 & -\sin\theta \\ 0 & \cos\phi & \sin\phi\cos\theta \\ 0 & -\sin\phi & \cos\phi\cos\theta \end{bmatrix}. \tag{2.3}$$

Note that in this example, the body-fixed aircraft reference frame Fr_A can replace the body-fixed simulator reference frame Fr_S.

2.4. Actuator Geometry

The geometry of a six-degree-of-freedom synergistic motion system is given in Figure 2.4. The relevant vectors relating the locations of the upper and lower bearings of the j-th actuator are shown below in Figure 2.5.
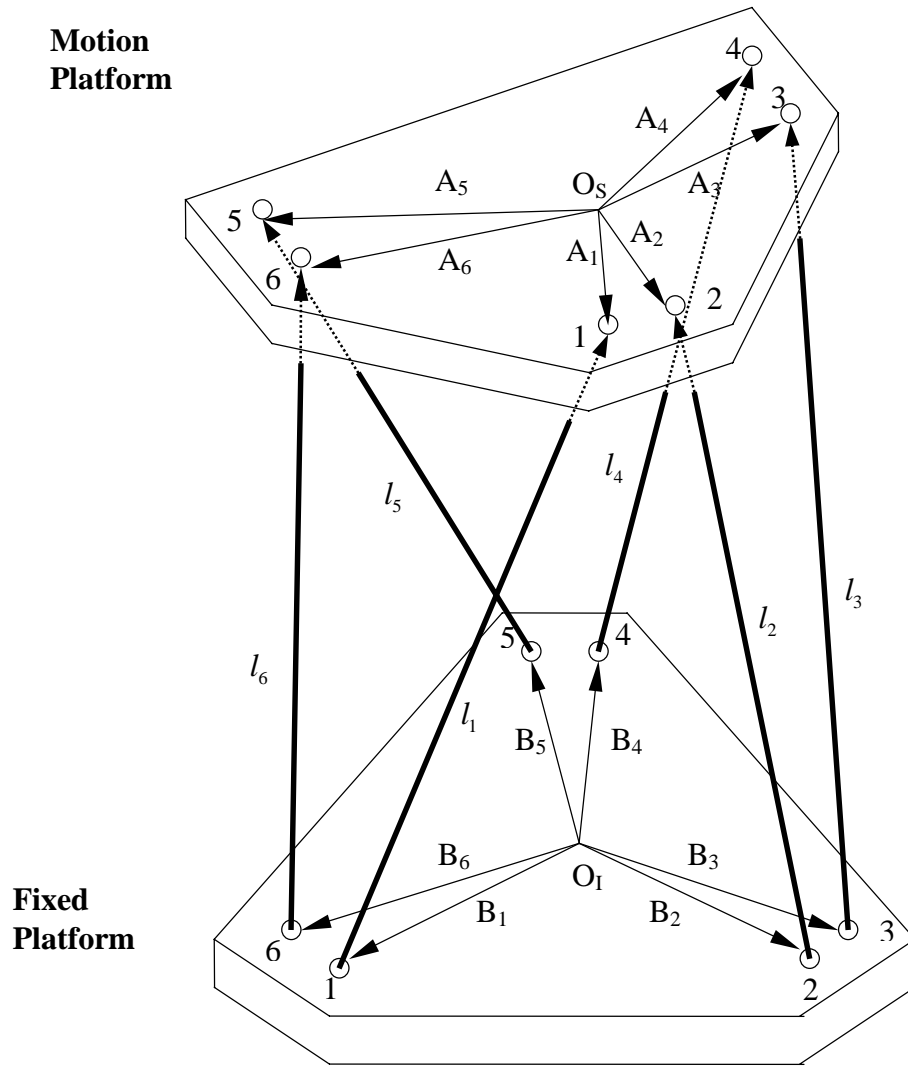
Figure 2.4. Geometry of a Six-Degree-of-Freedom Motion System. Adapted from Wu [13].
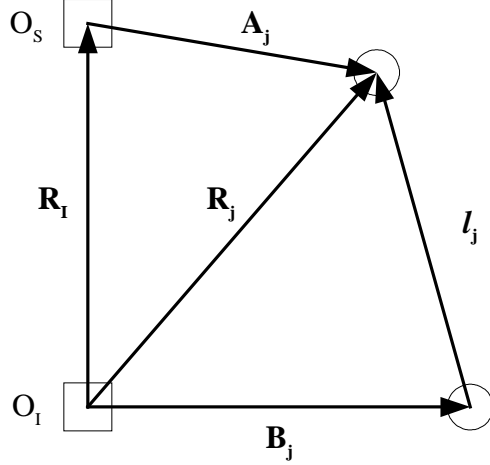
Figure 2.5. Vectors for the j-th Actuator.

In Figure 2.5, O_S and O_I are the centroids of the motion platform and fixed platform respectively, and are also respectively the origins for Fr_S and Fr_I. It can be seen that the relation among those vectors is

$$\mathbf{R_I} + \mathbf{A_j^I} = \mathbf{R_j} = \mathbf{B_j^I} + l_j. \tag{2.4}$$

The actuator length vector can then be found from

$$l_j = \mathbf{A_j^I} + \mathbf{R_I} - \mathbf{B_j^I}. \tag{2.5}$$

The expression of l_j in the inertial reference frame Fr_I is desired:

$$\begin{aligned} l_j^I &= \mathbf{A_j^I} + \mathbf{R_I} - \mathbf{B_j^I} \\ &= \mathbf{L_{SI}} \mathbf{A_j^S} + \mathbf{R_I} - \mathbf{B_j^I}, \end{aligned} \tag{2.6}$$

where $\mathbf{A_j^S}$ are the coordinates of the upper bearing attachment point of the j-th actuator in Fr_S and $\mathbf{B_j^I}$ are the coordinates of the lower bearing attachment point of the j-th actuator in Fr_I. The actuator extensions can then be found from

$$\begin{aligned} \Delta l_j^I &= l_j^I(t) - l_j^I(0) \\ &= \left(\mathbf{L_{SI}}(t) - \mathbf{L_{SI}}(0) \right) \mathbf{A_j^S} + \left(\mathbf{R_I}(t) - \mathbf{R_I}(0) \right). \end{aligned} \tag{2.7}$$

Usually the actuator extension is computed from a neutral platform position, where $\mathbf{L_{SI}}(0) = \mathbf{I}$ ($\mathbf{I}$ is the identity matrix), and $\mathbf{R_I} = \mathbf{0}$, therefore $\Delta l_j^I = \mathbf{L_{SI}} \mathbf{A}_j^S + \Delta \mathbf{R_I}$.

2.5. Nonlinear Input Scaling

Limiting and scaling are applied to both aircraft translational input signals $\mathbf{a_A^A}$ and rotational input signals $\mathbf{\omega_A^A}$. Limiting and scaling modify the amplitude of the input uniformly across all frequencies. Limiting is a nonlinear process that clips the signal so that it is limited to be less than a given magnitude. Limiting and scaling can be used to reduce the motion response of a flight simulator. A third-order polynomial scaling was developed [13] and has been implemented in the new simulator motion cueing algorithms.

When the magnitude of input to the simulator motion system is small, the gain is desired to be relatively high, or the output may be below the pilot's perception threshold. When the magnitude of input is high, the gain is desired to be relatively low or the simulator may attempt to go beyond its hardware limits. Let us define the input as x and the output as y. Now define x_{max} as the expected maximum input and y_{max} as the maximum output, and s_0 and s_1 as the slopes at $x = 0$ and $x = x_{max}$ respectively. Four desired characteristics for the nonlinear scaling are expressed as:

(1) $x = 0 \Rightarrow y = 0,$
(2) $x = x_{max} \Rightarrow y = y_{max},$
(3) $y'|_{x=0} = s_0,$
(4) $y'|_{x=x_{max}} = s_1,$

A third-order polynomial is then employed to provide functions with all the desired characteristics. This polynomial will be of the form

$$y = c_3 x^3 + c_2 x^2 + c_1 x + c_0 , \tag{2.8}$$

where

$$c_0 = 0,$$
$$c_1 = s_0,$$
$$c_2 = x_{max}^{-2} \left(3 y_{max} - 2 s_0 x_{max} - s_1 x_{max} \right),$$
$$c_3 = x_{max}^{-3} \left(s_0 x_{max} - 2 y_{max} + s_1 x_{max} \right).$$

One example of this polynomial gain is shown in Figure 2.6, with parameters set as

$x_{max} = 10, \ y_{max} = 6, \ s_0 = 1.0, \ s_1 = 0.1.$
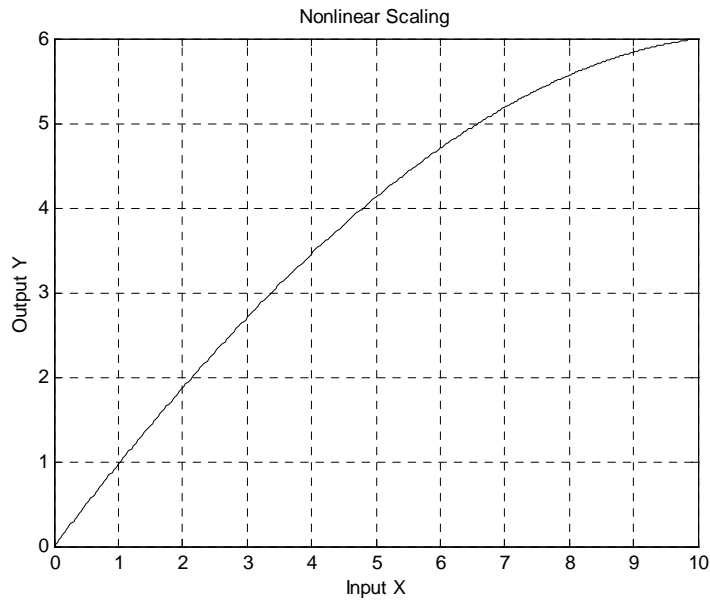
Figure 2.6. Nonlinear Input Scaling.

2.6. Specific Force at the Pilot's Head

The purpose of the motion cueing algorithm is to create a specific force vector and an angular velocity vector at the pilot's location in the simulator that approximates the stimulus that the pilot would experience in an actual aircraft. The relation between the specific force acting on the simulator pilot and the specific force at the origin of the simulator reference frame can be found from

$$\mathbf{f}_{PS}^S = \mathbf{a}_{PS}^S - \mathbf{g}^S$$
$$= \mathbf{a}_S^S + \dot{\boldsymbol{\omega}}_S^S \times \mathbf{R}_S + \boldsymbol{\omega}_S^S \times (\boldsymbol{\omega}_S^S \times \mathbf{R}_S) - \mathbf{g}^S \qquad (2.9)$$
$$= \mathbf{f}_S^S + \dot{\boldsymbol{\omega}}_S^S \times \mathbf{R}_S + \boldsymbol{\omega}_S^S \times (\boldsymbol{\omega}_S^S \times \mathbf{R}_S).$$

Both $\mathbf{f}_{PS}^S$ and $\boldsymbol{\omega}_S^S$ are used to compute sensed responses using the vestibular models discussed in Chapter 3. Similar expressions can be obtained for the specific force and angular velocity at the aircraft pilot's head.

2.7. Coordinated Adaptive Washout Algorithm

The intent of the NASA adaptive algorithm [7] is to adjust the response of the simulator washout filters in real time according to the current state of the simulator. The block diagram for this algorithm is shown in Figure 2.7. There are separate filtering channels for the translational and rotational degrees of freedom with a cross-feed path to provide the steady-state tilt coordination cues.
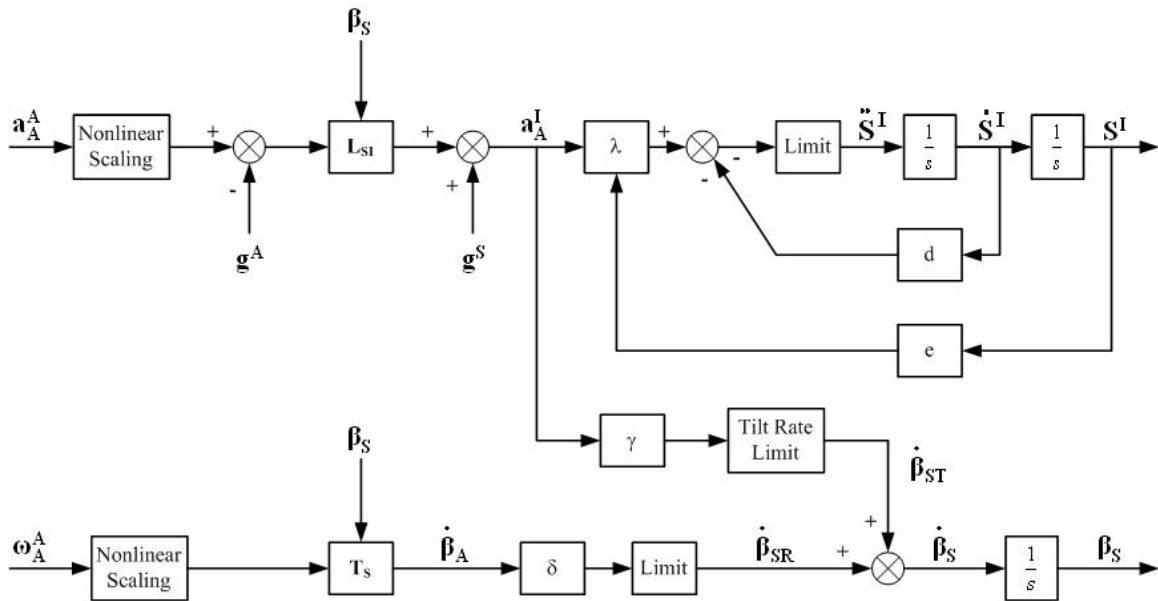
Figure 2.7. Coordinated Adaptive Washout (NASA Adaptive) Algorithm.

The aircraft acceleration vector $\mathbf{a}_A^A$ is first transformed from the center of gravity of the aircraft to the motion base centroid. After nonlinear scaling and limiting, the gravity vector is subtracted to produce a simulator frame specific force vector. The simulator specific force is transformed from the simulator frame Fr_S into the inertial frame Fr_I, resulting in the inertial specific force command $\mathbf{f}_A^I$. The specific force command $\mathbf{f}_A^I$ is passed through a translational channel with a time-varying gain λ to produce a simulator translational acceleration command $\ddot{\mathbf{S}}^I$. This acceleration is integrated to produce the velocity $\dot{\mathbf{S}}^I$, which is then integrated to produce the simulator translational position command $\mathbf{S}^I$. Both the velocity and position commands are employed as feedback.

The aircraft angular velocity vector $\boldsymbol{\omega}_A^A$ is limited and scaled similar to the translational channel, with the resulting vector being transformed to the Euler angular rate vector $\dot{\boldsymbol{\beta}}_A$. This vector is passed through the rotational channel with a time-varying gain δ to produce the vector $\dot{\boldsymbol{\beta}}_{SR}$. The tilt coordination rate $\dot{\boldsymbol{\beta}}_{ST}$ is formed from the acceleration $\mathbf{a}_A^I$ being passed through the cross-feed channel with a fixed gain γ. The summation of $\dot{\boldsymbol{\beta}}_{ST}$ and $\dot{\boldsymbol{\beta}}_{SR}$ will yield $\dot{\boldsymbol{\beta}}_S$, which is then integrated to generate $\boldsymbol{\beta}_S$, the simulator angular position command.

$\mathbf{L}_{SI}$ and $\mathbf{T}_S$ are formed by Eqs. (2.1) and (2.2). The simulator translational position $\mathbf{S}^I$ and the angular position $\boldsymbol{\beta}_S$ are used to transform the simulator motion from degree-of-freedom space to actuator space as given in Eqs. (2.6) and (2.7), generating the actuator commands required to achieve the desired platform motion.

The control law for the longitudinal mode is given by the following expressions:

$$\ddot{S}_x^I = \lambda_x f_{Ax}^I - d_x \dot{S}_x^I - e_x S_x^I$$
$$\dot{\theta}_S = \gamma_x f_{Ax}^I + \delta_x \dot{\theta}_A,$$
(2.10)

where d_x, e_x, and γ_x are fixed parameters, and λ_x and δ_x are the time-varying parameters that are continuously adjusted in an attempt to minimize the instantaneous value of the cost function. The cost function is defined as

$$J_x = \frac{1}{2}\left(f_{Ax}^I - \ddot{S}_x^I\right)^2 + \frac{W_X}{2}\left(\dot{\theta}_A - \dot{\theta}_S\right)^2 + \frac{b_x}{2}\left(S_x^I\right)^2 + \frac{C_x}{2}\left(\dot{S}_x^I\right)^2,$$
(2.11)

where W_X, b_x, and C_x are constant weights that penalize the difference in response between the aircraft and simulator, as well as restraining the translational velocity and displacement in the simulator.

The time-varying parameters λ_x and δ_x are adjusted by steepest descent as given by

$$\dot{\lambda}_x = -K_{\lambda_x}\frac{\partial J_x}{\partial \lambda_x} + K_{i\lambda_x}\left(\lambda_{x0} - \lambda_x\right)$$
$$\dot{\delta}_x = -K_{\delta_x}\frac{\partial J_x}{\partial \delta_x} + K_{i\delta_x}\left(\delta_{x0} - \delta_x\right),$$
(2.12)

where K_{λ_x}, $K_{i\lambda_x}$, K_{δ_x}, and $K_{i\delta_x}$ are constants. The first right-hand side term of each equation defines the change of the time-varying parameter is to be toward a minimum, and together with the second term defines the rate of change. The second term also restrains the deviation of either λ_x or δ_x respectively from their original values.

3. Vestibular System Modeling

This chapter discusses the development of vestibular system sensation models that are most consistent with both experimental and theoretical analyses and can be readily implemented into a motion cueing algorithm. These results are based on the literature presented by several researchers who investigated the physiology of the semicircular canals and the otolith organs, and also studied rotational and linear motion sensation. The development of the semicircular canals sensation model follows a previous presentation [13]. In addition, research on motion thresholds was surveyed in order to produce values to be used in the motion cueing algorithm development.

The vestibular system is located in the inner ear and consists of the semicircular canals and otolith organs that sense angular and linear motion respectively. The location and orientation of the vestibular system in the head is shown in Figure 3.1.
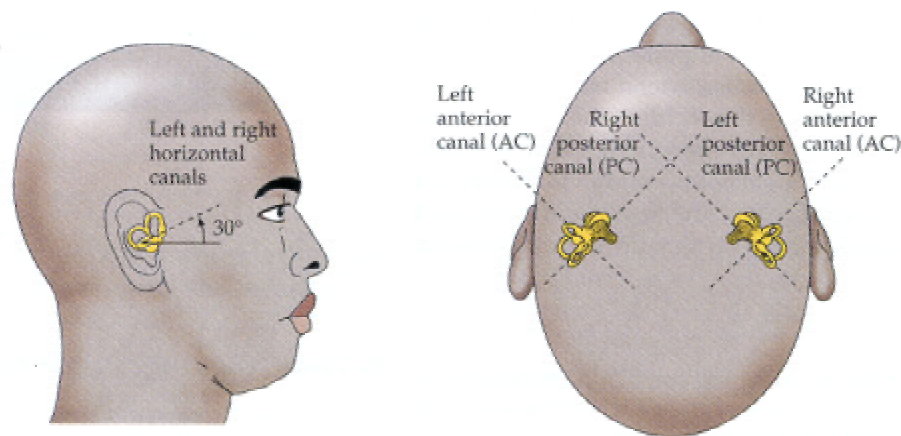
Figure 3.1. Location and Orientation of the Semicircular Canals. Reproduced with Permission from Purves, et al. [14].

3.1. Semicircular Canals

3.1.1. Physiological Description

The semicircular canals consist of two sets of three elliptical cavities or canals that are filled with a fluid known as endolymph. The orientation of the canals in the head is shown in Figure 3.1. With the head in its normal erect position, the plane through the diameter of each horizontal canal is inclined about thirty degrees above an earth-horizontal plane. The posterior vertical canal lies in an almost vertical plane, forming a 45-degree angle with the frontal plane of the head. The anterior canal is also at a 45-degree angle with the frontal plane, forming a right angle with the posterior canal.

At one point on each canal, the canal cavity swells to form a bulbous expansion called the ampulla that contains the sensory ephithelium or crista. The crista contains bundles of sensory hair cells that extend into a gelatinous mass called the cupula as shown in Figure 3.2. The cupula bridges the width of the ampulla cavity, forming a seal through which endolymph cannot circulate. When the head turns in the plane of one of the canals, the inertia of the endolymph produces a force across the cupula, deflecting it in the opposite direction of head movement and causing a displacement of the hair bundles in each hair cell. Each hair cell has about 70 stereocilia and one kinocilium [15], with the stereocilia graded in length towards the kinocilium. Within one cupula, each kinocilium is on the same side as its stereocilia, forming a direction of polarization. When the cupula deflection is in the direction of the kinocilium, the hair cells will be maximally excited; whereas when the deflection is in the opposite direction the cells will be maximally inhibited.
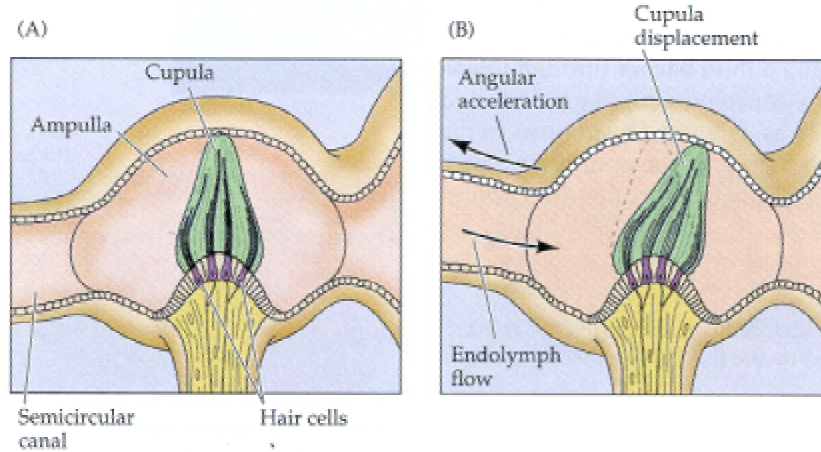
Figure 3.2. Physiology of the Semicircular Canals Cupula. Reproduced with Permission from [14].

There are two types of sensory cells located in the cupula. The type I cells are contained in a nerve chalice and are innervated by fibers with a large diameter. The type II cells are cylindrical and are innervated by fibers with a small diameter. Both types of cells have a series of small hairs that penetrate into the cupula mass.

3.1.2. Mathematical Model

Zacharias [16] reported that Steinhausen first developed a linear second-order model of canal dynamics to explain the observed characteristics of vestibular-induced eye movements in fish (pike). This model was further refined by the "torsion-pendulum" model of Van Egmond, et al., [17], and was later developed from a systems approach by Mayne [18]. The transfer function for this overdamped system is

$$\frac{\theta_e(s)}{\alpha(s)} = \frac{\tau_1 \tau_2}{(1 + \tau_1 s)(1 + \tau_2 s)},$$ (3.1)

Further studies showed that the torsion-pendulum model does not completely represent rotational sensation. Young and Oman [19] formulated an adaptation operator and cascaded it with the torsion-pendulum model to resolve the conflicts between the

response predicted by the torsion-pendulum model and the perceptual responses measured in experiments. The addition of the adaptation operator resulted in the following transfer function:

$$\frac{\phi_c(s)}{\alpha(s)} = K_{SCC} \left[\frac{\tau_a s}{(1 + \tau_a s)} \right] \left[\frac{1}{(1 + \tau_1 s)(1 + \tau_2 s)} \right], \tag{3.2}$$

where the gain K_{SCC} noted by Zacharias [16] is proportional to $\tau_1 \tau_2$.

Zacharias [16] reported several experiments suggesting an additional lead component. With the addition of this component, a model representing both the semicircular canal dynamics and the neural transduction dynamics was established:

$$\frac{\phi_c(s)}{\alpha(s)} = K_{SCC} \left[\frac{\tau_a s}{(1 + \tau_a s)} \right] \left[\frac{(1 + \tau_L s)}{(1 + \tau_1 s)(1 + \tau_2 s)} \right]. \tag{3.3}$$

Parameters for man are difficult to measure because direct measurement of the afferent response of the semicircular canals cannot be obtained. Therefore, most early experiments to determine the torsion-pendulum model parameters were based on subjective responses. Van Egmond [17] reported that the long time constant τ_1 and short time constant τ_2 had values of about 10 seconds and 0.1 seconds respectively. The values were based on the verbal response of humans subjected to various motion inputs in both a rotating chair and a torsion swing. Zacharias [16] noted that Meiry, measuring detection latency as a function of angular acceleration step size, obtained a 7-second long time constant for roll-axis rotation about the earth-vertical axis, and that Guedry, using a short period rotational stimulus consisting of an acceleration pulse doublet, and a response measure of apparent displacement, found values of 16 seconds for yaw-axis rotation and 7 seconds pitch-axis rotation about the earth-vertical axis. Zacharias [16] then reported

that Malcolm and Melvill-Jones investigated the response to earth-vertical rotation about all three axes by using a velocity step as the stimulus, and measured the elapsed time to zero perceptual response. They obtained values of 6.1 seconds for the roll axis, 5.3 seconds for pitch, and 10.2 seconds for yaw.

Goldberg and Fernandez [20] determined average parameters for the semicircular canals of the squirrel monkey by direct measurement of the afferent nerves due to various angular acceleration inputs of different amplitudes and frequencies. Their transfer function related the afferent firing rate of the vestibular nerve to the angular acceleration input:

$$\frac{AFR(s)}{\alpha(s)} = 3.44 \left[\frac{80s}{(1+80s)} \right] \left[\frac{(1+0.049s)}{(1+5.7s)(1+0.003s)} \right]. \tag{3.4}$$

The model parameters were estimated with the exception of the short time constant τ_2, which was determined analytically based on the physiology of the endolymph. Goldberg and Fernandez [20] noted that the short time constant τ_2 is estimated to be 0.005 seconds for humans.

It can be inferred that the long time constant τ_1 measured by Van Egmond, et al., Meiry, Guedry and Malcolm and Melvill-Jones, as reported by Zacharias [16], does not actually represent the semicircular canal parameter in the model, but is an overall dynamics parameter representing the rotational sensation response to an angular velocity input. Zacharias [16] suggested that each axis of rotation has an equivalent "body axis" canal pair with a distinct time constant. The psychophysical results show each of the three axes having a distinct value for τ_1.. However, physiological results based on afferent responses by Goldberg and Fernandez show the same value for τ_1 for the three

canal pairs. Zacharias [16] suggested the differences shown in the psychophysical results could occur at a central origin at the perceptual level.

From subjective pilot measurements of angular acceleration thresholds on a moving base platform, Hosman and Van der Vaart [21] obtained the following semicircular canals transfer function, neglecting gain sensitivity and adaptation:

$$H_{SCC}(s) = \frac{1 + 0.1097s}{(1 + 5.924s)(1 + 0.005s)}.$$

(3.5)

These results are based upon roll and pitch acceleration thresholds; yaw thresholds were not measured. The value for τ_1 agrees well with the value obtained by Goldberg and Fernandez [20]. The value obtained for τ_L compares to a value of 0.06 seconds that Zacharias [16] reported that Benson and Ormsby obtained in experiments measuring nystagmus or involuntary eye movement due to motion.

Zacharias [16] assumed that the angular velocity $\hat{\omega}$ from the semicircular canals that is sensed by human subjects is proportional to the cupula deflection ϕ_c, and is expressed by the transfer function

$$\frac{\hat{\omega}(s)}{\omega(s)} = \frac{\tau_1 s}{(1 + \tau_1 s)(1 + \tau_2 s)},$$

(3.6)

where Zacharias [16] noted that the sensitivity gain is equal to the magnitude of the long time constant τ_1. Goldberg and Fernandez [20] obtained gain sensitivity between the input stimulus and the afferent firing rate that was estimated at 3.44 spikes/sec per deg/sec^2. Zacharias [16] noted that Ormsby suggested that the sensed angular velocity $\hat{\omega}$ is proportional to the afferent firing rate. While no one to date has experimentally obtained this parameter, Zacharias [16] reported that Curry, et al. provided an estimate of

the overall gain between perceived and input angular velocity based on angular acceleration thresholds.

From this research, a transfer function that can best relate the sensed angular velocity to the acceleration stimulus is employed in the motion cueing algorithm development:

$$\frac{\hat{\omega}(s)}{\alpha(s)} = 5.73 \left[\frac{80s}{(1+80s)} \right] \left[\frac{(1+0.06s)}{(1+5.73s)(1+0.005s)} \right]. \tag{3.7}$$

The frequency response of the transfer function given in Eq. (3.7) is shown in Figure 3.3. Both the torsion-pendulum model and the complete model with the lead and adaptation mechanisms included are shown.
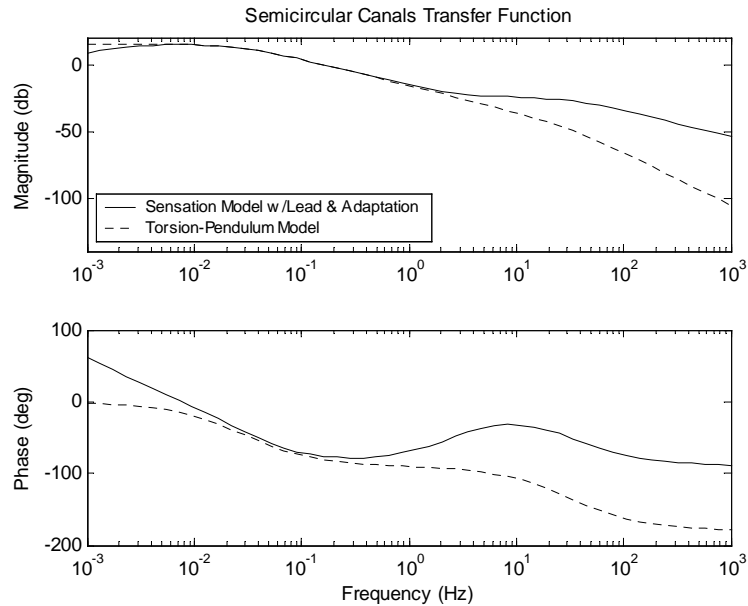
Figure 3.3. Frequency Response of Semicircular Canals Transfer Function.

The sensory function of the semicircular canals can be described by observing the frequency response of the torsion-pendulum model. In the range of normal head movement from 0.1 to 1.0 Hz [22], the gain response decreases by 20 dB/decade with the

phase close to minus 90 degrees. In this frequency range, the semicircular canals function as "integrating accelerometers" or angular velocity transducers. At very low frequencies less than 0.01 Hz, the phase approaches zero degrees, thus functioning as an accelerometer. At very high frequencies greater than 100 Hz, the phase approaches minus 180 degrees, thus functioning as an angular displacement transducer. The effects of adaptation and lead on rotational sensation are apparent; adaptation influences the afferent response at low frequencies below 0.01 Hz while the lead component influences high frequencies greater than 10 Hz.

For implementation into the optimal cueing algorithm, angular velocity is employed as a stimulus, requiring the following transfer function:

$$\frac{\hat{\omega}(s)}{\omega(s)} = 5.73 \frac{80s^2}{(1+80s)} \frac{(1+0.06s)}{(1+5.73s)(1+0.005s)}. \tag{3.8}$$

In addition, numerical stability problems may result when integrating the transfer function due to the small magnitude of the short time constant τ_2 in the denominator relative to the simulation time step. Solely neglecting the short time constant would result in an unrealizable transfer function, but the lead time constant τ_L in the numerator could also be neglected since its order of magnitude is the same as the cueing algorithm time step. For numerical integration, the step size should be at least ten times smaller than the smallest time constant. The effect of both τ_2 and τ_L is also well above the range of normal head movements. For these reasons a reduced-order transfer function can be utilized:

$$\frac{\hat{\omega}(s)}{\omega(s)} = 5.73 \frac{80s}{(1+80s)(1+5.73s)} \tag{3.9}$$

30

3.1.3. Physiological Interpretation

Wu [13] presented a physiological interpretation of the behavior of the semicircular canals. He noted that the cupula-endolymph system first transforms an acceleration input to the head into a displacement of the cupula. This displacement then becomes an afferent response through a "mechano-neural" transduction system consisting of sensory hair cells and both efferent and afferent nerves.

Many researchers have shown that an overdamped torsion-pendulum model could represent the cupula-endolymph system. Wu [13] reported that the remaining terms represent an adaptation-lead mechanism, noting the controversy over whether its origins lie in either the cupula-endolymph or the mechano-neural system. Wu reported that Goldberg and Fernandez [20] assumed that the origin of the adaptation mechanism might be centered on the physiology of the hair cells and/or the afferent neurons. Wu then noted that Goldberg and Fernandez suggested the lead mechanism may originate from sensory hair cells that are sensitive to both cupula displacement and velocity, which is reflected in the time constant τ_L. Wu [13] presented an interpretation by Schmid, et al. in which the lead mechanism is represented by efferent pathways that modify the feed-forward afferent dynamics by means of a negative feedback. Wu [13] demonstrated that this approach would justify the difference in order-of-magnitude of the adaptation time constant τ_A and the lead time constant τ_L.

3.2. Otoliths

3.2.1. Introduction

The otolith organs are the elements of the vestibular system that provide linear motion sensation in humans and mammals. These organs are responsive to specific

force, responding to both linear acceleration and tilting of the head with respect to the gravity vector. However, the otoliths cannot discriminate between acceleration and tilt, requiring additional sensory information to resolve this ambiguity. There are two otolith organs, the utricle and saccule, in each inner ear. The utricle primarily senses motion in the horizontal plane, while the saccule primarily senses motion in the vertical plane. The otolith organs are inclined by about 20 to 30 degrees above the earth-horizontal plane as shown in Figure 3.1.

3.2.2. *Physiological Description*

The otolith organs consist of a two-layer structure known as the otolithic membrane that is attached to a base containing sensory cells. The otolithic membrane is composed of an upper layer, the otoconial layer, and a lower layer, the gelatinous layer. The endolymph fluid is in contact with the upper surface of the otoconial layer. The otoconial layer consists of calcium carbonate crystals embedded in a gelatinous material that rests on a less dense and extremely deformable gelatinous layer. This gelatinous layer is in turn attached to the sensory cell base known as the macula that is incorporated into the membranous tissue walls of the inner ear. The macula is rigidly attached to the skull and therefore moves with the head.

There are two types of sensory cells located in the macula. The Type I cells are enclosed in a nerve chalice and are innervated by fibers with a large diameter. The Type II cells are cylindrical and are innervated by fibers with a small diameter. Fernandez and Goldberg [23] reported that cells in the outer (peripheral) otolith region are primarily Type II cells, and in the central (striolar) region cells are primarily Type I. Both types of cells have a series of small hairs that penetrate the lower portion of the gelatinous layer.

Each hair cell has about 70 stereocilia and one kinocilium [15], with the stereocilia graded in length toward the kinocilium.

The resulting displacement of the otolithic membrane due to forward linear acceleration is illustrated in Figure 3.4. The arrow in the figure shows the direction of the specific force acting upon the head. With a forward acceleration or backward tilting of the head, the denser otoliths tend to lag behind the macula, with the relative motion resulting in deformation of the gelatinous and otoconial layers in shear. When the shear deformation is in the direction of the kinocilium, the cell will be excited, whereas when the deformation is in the opposite direction, the cell will be inhibited. The directions of the maximum excitation and inhibition of a hair cell are defined by its polarization axis. In each macula, the central parting known as the striola separates oppositely polarized regions. For each position due to translational movement, some cells will be maximally excited, while others will be maximally inhibited.
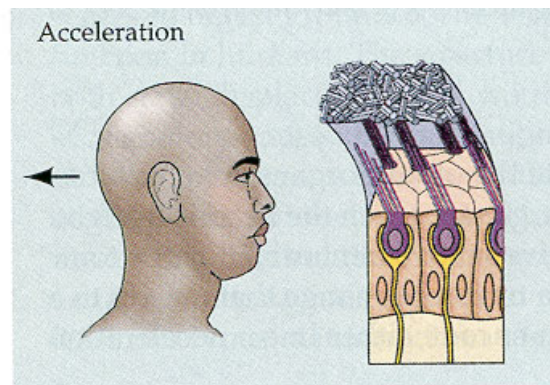
Figure 3.4. Displacement of the Otolithic Membrane due to Forward Acceleration. Reproduced with Permission from Purves, et al. [14].

Fernandez and Goldberg [24] identified two types of neurons that are characterized by their variance or regularity of discharge, hereafter referred to as regular and irregular units. From a sample population of units, they identified a ratio of regular

to irregular units to be approximately three to one. The response of a neuron is the afferent firing rate (AFR).

3.2.3. Mathematical Modeling

Zacharias [16] reported that Meiry first investigated subjective responses to linear motion by using a cart to produce longitudinal sinusoidal motion. By measuring the subjective indication of direction, he obtained a transfer function relating perceived velocity $\hat{v}$ to stimulus velocity v:

$$\frac{\hat{v}(s)}{v(s)} = \frac{K_{OTO}\tau_1 s}{(\tau_1 s + 1)(\tau_2 s + 1)}, \tag{3.10}$$

where the long time constant τ_1 and short time constant τ_2 are 10 and 0.66 seconds respectively, and the gain K_{OTO} is undetermined since amplitude measurements were not taken. Zacharias [16] then noted that Peters suggested the subjective response measured by Meiry was perceived acceleration and not perceived velocity, since in response to an acceleration step, the model predicted a perceived response that decays to zero with a time constant of 10 seconds.

Young and Meiry [25] noted that the model proposed by Meiry correctly predicted the phase of perceived velocity for lateral oscillation and time to detect motion under constant acceleration, but failed to predict the otoliths' response to sustained tilt angle as indicated by behavioral and physiological data. They noted that the model agreed with dynamic counter-rolling data (of the eye) at high frequencies, but experimental counter-rolling at zero frequency showed a static component of otolith output with no phase lag (the model assumed no static output and at zero frequency approached 90 degrees of lead). They proposed the following revised model of specific force sensation:

34

$$\frac{\hat{f}(s)}{f(s)} = \frac{1.5(s+0.076)}{(s+0.19)(s+1.5)},$$

(3.11)

which, when rearranged in terms of the time constants, yields

$$\frac{\hat{f}(s)}{f(s)} = \frac{0.4(13.2s+1)}{(5.33s+1)(0.66s+1)}.$$

(3.12)

With a smaller long time constant (5.33 seconds) and an additional lead term, they modeled both perceived tilt and acceleration in response to acceleration input. They noted that the model acts as a velocity transducer over the frequency range of 0.19 to 1.5 rad/s, with the transfer function from specific force to perceived tilt or lateral acceleration having a static sensitivity of 0.4. This model presumes the equivalence of linear acceleration sensation with that of tilt.

Zacharias [16] noted that a lumped parameter model of otolith motion could be used to represent the two lag time constants, similar to the torsion-pendulum model for the semicircular canals. Ormsby [26] first developed this model, and Grant, et al. [27-30] later refined the model as part of their theoretical analysis of the otolithic membrane. Grant and Best [30] obtained the following transfer function for the model:

$$\frac{x(s)}{f(s)} = \left(1 - \frac{\rho_e}{\rho_o}\right)\frac{\tau_1 \tau_2}{(1+\tau_1 s)(1+\tau_2 s)},$$

(3.13)

where x is the relative displacement of the otoconial layer with respect to the head, ρ_e is the density of the endolymph, ρ_o is the density of the otoconial membrane, with $\rho_o > \rho_e$. For the otoliths, we again have an overdamped system with $\tau_1 \gg \tau_2$.

In determining the value of the short time constant τ_2, Grant and Best [30] first examined the maximum displacement of the otoconial layer in response to a step change

in linear velocity. The acceleration for a linear velocity step U is $a_x = -U\delta(t)$, with $g_x =$

0, where $\delta(t)$ is the unit impulse function. The transient response to Eq. (3.13) is then

$$x(t) = U\left(1 - \frac{\rho_o}{\rho_e}\right)\tau_2(e^{-t/\tau_1} - e^{-t/\tau_2}). \qquad (3.14)$$

By assuming that the short exponential term in Eq. (3.14) has reached zero and

the long exponential term remains close to unity, the maximum displacement of the

otoconial layer x_{max} can be approximated as

$$x_{\text{max}} \cong U\left(1 - \frac{\rho_e}{\rho_o}\right)\tau_2, \qquad (3.15)$$

The theoretical continuum mechanics analysis performed by Grant and Best [29]

first indicated that this short time constant τ_2 is 0.002 seconds or less. They later

demonstrate that this value turns out to be too large when reasonable values of the

maximum otolith displacement are considered. For $\rho_o = 2.0$ and $U = 25$ cm/sec (a

reasonable value for normal head velocity), Eq. (3.15) becomes $x_{\text{max}} = 12.5\tau_2$. For $\tau_2 =$

0.002 sec, the maximum displacement of the otolithic membrane resulted in $x_{\text{max}} = 250$

μm. It was assumed for shear deformation the maximum displacement should not exceed

the thickness of the otoconial layer (25 μm), indicating the short time constant should be

one order of magnitude smaller, $\tau_2 = 0.0002$ sec. This indicated that more damping was

needed in the lumped parameter model. Grant and Best [30] showed that additional

damping could be introduced by the inclusion of a viscoelastic gelatinous layer in the

continuum mechanics model.

Ormsby [26] neglected the short time constant τ_2 in Eq. (3.15), and after

rearranging terms, approximated the otolith mechanical dynamics by

$$\frac{x(s)}{f(s)} = \frac{A}{s+A}, \tag{3.16}$$

and then proposed a model for the response of the otolith afferent dynamics:

$$\frac{AFR(s)}{f(s)} = \frac{Bs + (B+C)A}{s+A}, \tag{3.17}$$

where *AFR* is the change in afferent firing rate from the resting discharge, and the constants *A*, *B*, and *C* are undetermined. This model assumes that higher centers process the afferent response optimally to estimate the perceived specific force $\hat{f}$ as shown in Figure 3.5.
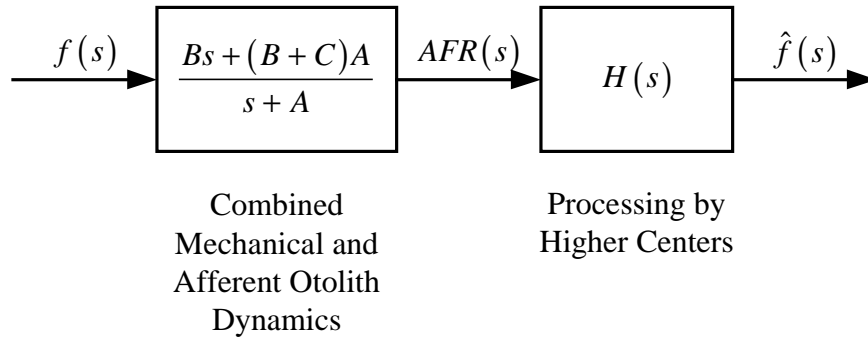
Figure 3.5. Model of Otolith Specific force Sensation. Adapted from Ormsby [26]**.**

The steady-state optimal processor *H(s)* is then determined by solving the associated Wiener-Hopf equation [31], yielding a solution of the form

$$H(s) = M \frac{s+A}{(s+F)(s+G)}, \tag{3.18}$$

where *F*, *G*, and *M* are nonlinear functions of the independent variables *A*, *B*, and *C* in Eq. (3.17). *H(s)* is then cascaded with the otolith afferent dynamics to estimate the perceptual dynamics associated with the otoliths:

$$\frac{\hat{f}}{f} = BK\frac{\left(s + \dfrac{(B+C)A}{B}\right)}{(s+F)(s+G)},$$
(3.19)

which is equivalent to the Young-Meiry [25] model given in Eq. (3.11). Ormsby [26] noted that Fernandez, Goldberg, and Abend found an average steady-state change in afferent firing rate from the utricle due to a 1-g step to be 45 impulses per second (ips), resulting in the condition that $B + C = 45$. Setting Eq. (3.19) equal to Eq. (3.11) and including this constraint results in the following model for the afferent response:

$$\frac{AFR(s)}{f(s)} = 90\,\frac{s+0.1}{s+0.2},$$
(3.20)

This transfer function, when rearranged in terms of its time constants, becomes

$$\frac{AFR(s)}{f(s)} = 45\,\frac{10s+1}{5s+1}.$$
(3.21)

Ormsby [26] noted the following about this model:

> The approach taken here can yield a model which accounts reasonably well for the available subjective data, the known physiological structure of the sensor and makes reasonable predictions concerning the afferent processes and the associated central processing.

Fernandez and Goldberg [23] studied the discharge of peripheral otolith neurons in response to sinusoidal force variations in the squirrel monkey. Both regularly and irregularly discharging neurons were measured. The gain curves for the regular units were flat, with a small phase lead at low frequencies and a larger phase lag at higher frequencies. The irregular units showed a larger gain enhancement and phase lead at high frequencies, which could not be represented by a first-order lead operator. They noted on average, there is an increase by a factor of eighteen in gain enhancement in irregular units but only an increase of a factor of two for regular units.

The frequency responses of regular and irregular units resulted in a transfer function of the form

$$H(s) = K_{OTO} \frac{1 + k_A \tau_A s}{1 + \tau_A s} \frac{1 + k_v \left(\tau_v s\right)^{k_v}}{1 + \tau_M s} = K_{OTO} \; H_A(s) \frac{H_v(s)}{H_M(s)}. \tag{3.22}$$

In Eq. (3.22), the term H_v is a velocity-sensitive operator with a fractional exponent ($k_v <$ 1) and provides most of the gain enhancement and phase lead found in the irregular units. The value of k_v reflects the effectiveness of the lead operator and is closely related to the slope of the gain curve. The term H_A is an adaptation operator that contributes to low frequency phase leads and increases of gain from static or zero frequency to 0.006 Hz. The term H_M is a first-order lag operator that Fernandez and Goldberg [23] noted might reflect the mechanics of otolith motion. This lag term accounts for the high frequency phase lags observed in regular units and for high frequency phase leads in irregular units being smaller than would be predicted solely by a fractional lead operator. The term K_{OTO} defines the static sensitivity in terms of afferent firing rate per unit of acceleration, i.e., in units of impulses per second per g (ips/g).

Fernandez and Goldberg [23] estimated parameters for the transfer function, obtaining nearly equal results for various values of τ_v. The median parameters for both regular and irregular units for $\tau_v = 40$ seconds are given in Table 3.1.

Table 3.1. Median Parameters for Regular and Irregular Units.

	k_v	k_A	τ_A	τ_M	K_{OTO}
Regular	0.188	1.12	69 sec	16 msec	25.6 ips / g
Irregular	0.440	1.90	101 sec	9 msec	20.5 ips / g

Because of the fractional exponent in the transfer function of Eq. (3.22), an elementary solution to its response cannot be readily obtained. However, an approximate

solution to the response can be derived through the application of fractional calculus [32]. The derivation to obtain a response to a transfer function with fractional exponents is given in Appendix A. Applying this derivation with the regular unit parameters given in Table 3.1 results in the response to a unit step:

$$
\begin{aligned}
x(t) = {}& 25.601 - 28.673e^{-62.5t} + 3.073e^{-0.014493t} \\
& - 10.786E_t\left(-0.188, -62.5\right) + 1.156E_t\left(-0.188, -0.014493\right) \\
& + 9.629\frac{t^\nu}{\Gamma(\nu+1)},
\end{aligned}
\tag{3.23}
$$

where Γ is the gamma function.

Eq. (3.23) is an infinite series. For ν equal to zero, Eq. (3.23) will reduce to the Taylor series expansion of the exponential function. When ν is not equal to zero, $E_t\left(\nu, a\right)$ is a transcendental function that can only be approximated. A recursion formula was derived, where the solution to the function $E_t\left(\nu, a\right)$ is given as

$$
E_t\left(\nu, a\right) = \frac{t^\nu}{\Gamma(\nu+1)} + \frac{at^{\nu+1}}{\Gamma(\nu+2)} + \frac{a^2 e^{at}}{\Gamma(\nu+2)}\int_0^t e^{-au}u^{\nu+1}du.
\tag{3.24}
$$

Similarly, the unit step response for the irregular unit parameters is derived:

$$
\begin{aligned}
x(t) = {}& 20.308 - 35.588e^{-111.1111t} + 18.280e^{-0.009901t} \\
& - 86.063E_t\left(-0.44, -111.1111\right) + 40.769E_t\left(-0.44, -0.009901\right) \\
& + 45.294\frac{t^\nu}{\Gamma(\nu+1)}.
\end{aligned}
\tag{3.25}
$$

Hosman [33] noted that the fractional exponent models are not easy to implement in motion cueing algorithms due to the fractional exponent in the lead term. He reported a simplified model of the same form developed by both Ormsby [26] and Grant and Best [29]:

$$\frac{AFR(s)}{f(s)} = 33.3\frac{(s+1)}{(0.5s+1)(0.016s+1)}. \tag{3.26}$$

Note that the gain terms for the Fernandez-Goldberg model [23] from Table 3.1 are about one half that of the gain value used by Ormsby [26] to develop his model. Hosman [33] proposed a gain term of less magnitude than that used by Ormsby [26] that may provide an improved approximation to the Fernandez-Goldberg responses. Due to the adaptation mechanism in the Fernandez-Goldberg model [23], these gains will require a long duration step input to be realized in steady state. Hosman [33] chose the short time constant τ_2 to be equal to the otolith mechanics time constant τ_M reported by Fernandez and Goldberg [23] for the regular units. No basis, however, was given for the values selected for the long time constant τ_1 and the lead time constant τ_L, which are one order of magnitude less than those resulting from the model developed by Ormsby [26].

By using the long and lead time constants reported by Ormsby [26] in Eq. (3.21), and selecting the short time constant and gain reported by Hosman [33] in Eq. (3.26), the following transfer function results for the afferent otolith dynamics:

$$\frac{AFR(s)}{f(s)} = 33.3\frac{(10s+1)}{(5s+1)(0.016s+1)}. \tag{3.27}$$

The response to a step input of 1-g magnitude (9.81 m/s^2) will now be examined for the Fernandez-Goldberg model [23] with both the regular and irregular unit parameters. Figure 3.6 compares the step responses to the response for the proposed afferent dynamics model given in Eq. (3.27) for both 1-second and 30-second durations. Note that the onset for the proposed model is faster than the regular unit, but slower than the irregular unit. There is no large overshoot as observed with the irregular unit response. The steady-state response for the proposed model is less than the irregular unit

response but greater than the regular unit response, and approaches the regular unit response for the given time duration. Both the regular and irregular unit response will slowly approach their respective gain values, and beyond about 80 seconds the irregular unit response will decrease below that of the proposed model. The model more closely represents the population-dominant regular units with a faster onset and higher magnitude steady state effects that occur in the less prevalent irregular units.
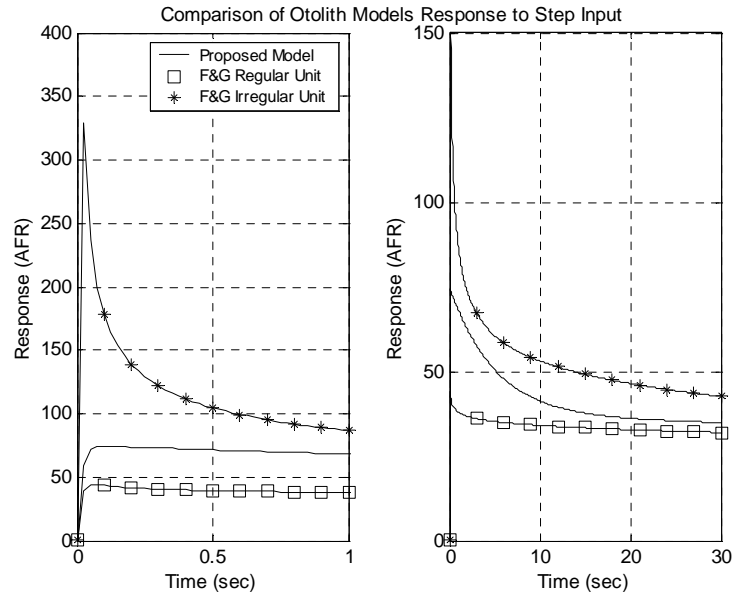
Figure 3.6. Comparison of Otolith Models Response to a 1-g Step Input.

From this research, a transfer function that can best relate the sensed response to the specific force stimulus is proposed:

$$\frac{\hat{f}}{f} = K_{OTO} \frac{(\tau_L s + 1)}{(\tau_1 s + 1)(\tau_2 s + 1)},$$

(3.28)

with $K_{OTO} = 0.4$, $\tau_1 = 5$ sec, $\tau_2 = 0.016$ sec, and $\tau_L = 10$ sec. For implementation into the motion cueing algorithms, Eq. (3.28) can be rewritten as

$$\frac{\hat{f}}{f} = K'_{OTO} \frac{(s + A_0)}{(s + B_0)(s + B_1)},$$

(3.29)

where $A_0 = 1/\tau_L$, $B_0 = 1/\tau_1$, $B_1 = 1/\tau_2$, and $K'_{OTO} = K_{OTO}\tau_1\tau_2/\tau_L$.

The frequency response of the proposed transfer function in Eq. (3.28) compared to the Young-Meiry model [25] of Eq. (3.11) is shown in Figure 3.7. Note that the gain and phase lag for the Young-Meiry model [25] occur at a much lower frequency as compared to the proposed model. This is due to the magnitude of the short time constant τ_2 for the Young-Meiry model [25] being an order of magnitude larger than the value used in the proposed model that was obtained by Fernandez and Goldberg [23]. In the range of normal head movements from 0.1 to 1.0 Hz [22], the gain for the proposed model remains constant, with the phase close to zero degrees. In this frequency range, the otolith functions as a specific force transducer.
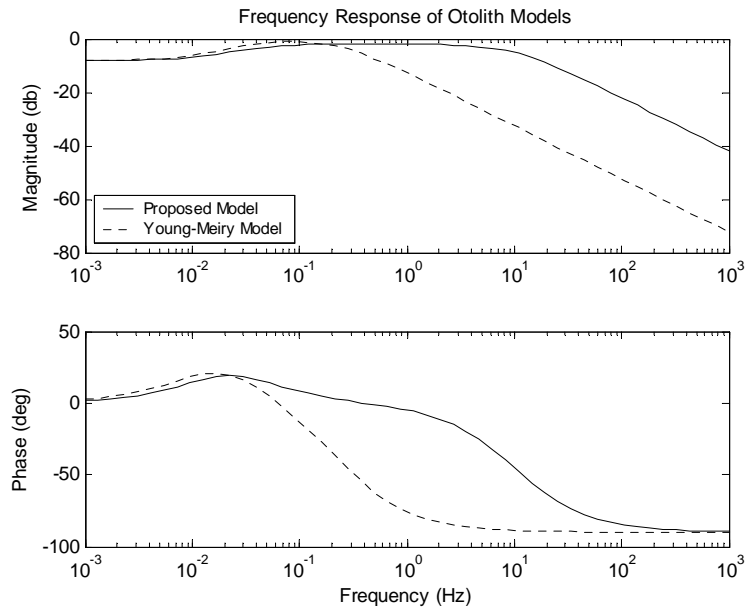
Figure 3.7. Frequency Response of Proposed and Young-Meiry Otolith Models.

3.2.4. *Physiological Interpretation*

Modern theories of the operation of the otolith receptors are based on the assumption that the afferent responses are generated by the deflection of hairs in the

sensory cells as a result of the otolith displacement. A specific force input, in the form of either linear acceleration or tilt, is transformed by the otolith-endolymph system into a displacement of the otolith. This displacement is further transformed into an afferent response by the mechano-neural transduction system consisting of sensory hair cells and both efferent and afferent nerves.

Many researchers have shown that the otolith-endolymph system could be represented by an overdamped mass-spring-damper system. Grant and Best [29] reported that the magnitude of the long time constant τ_1 is considered correct by most investigators because the overall system (otolith organ, neural transmission, central nervous system processing, and involuntary eye motion) could easily follow such a slow time constant. The value Grant and Best [29] obtained for the short time constant τ_2 is a two order-of-magnitude decrease in time constant as compared to the value obtained from the ocular torsion responses measured by Young and Meiry [25]. This value is also a one order-of-magnitude decrease as compared to the value of τ_M that Fernandez and Goldberg [23] attribute to the afferent dynamics. The fast dynamic response of the otolith will decrease to the slower ocular torsion response due to losses in neural transmission and central nervous system processing.

Young and Meiry [25] first noted that the origin of the lead term could be neurological, either in central processing of the otolith displacement signals or through the presence of two types of hair cells in the macula. One type of hair cell would respond to displacement and the other would respond to the rate of change of otolith displacement. These hair cells could produce the lead term if they were of the slowly adapting type postulated by several researchers. Fernandez and Goldberg [23] later show

that the degree of sensitivity to the otolith velocity is a function of the fractional derivative in the lead operator, i.e., irregular units are more velocity-sensitive than regular units. They noted that this difference in sensitivity might be due to discrepancies that are more noticeable in irregular units.

Fernandez and Goldberg [23] suggested that the difference between the expected otolith displacement and afferent firing rate for both regular and irregular units may be attributed to the mechanical linkages between the sensory hair bundles and the gelatinous layer. They reported that these sensory hair bundles are not rigidly embedded in the membrane, but are enclosed in a fluid-filled meshwork between the membrane and the sensory epithelium. Motion could be transferred to the hairs either by directly contacting the meshwork or indirectly by viscous coupling with the fluid. They also noted that the irregular units correspond to thick afferents that stimulate the Type I hair cells in the striola. Grant and Best [30] also suggested that the nonlinear stiffness of the gelatinous layer could also contribute to these differences as well.

3.3. Motion Thresholds

Zacharias [16] reported that Clark reviewed twenty-five earlier studies that attempted to define an absolute threshold for angular acceleration. Clark noted the wide range in rotational devices, stimuli waveforms, psychophysical methods, and threshold definitions employed by various researchers. The threshold measurements reported showed a two order-of-magnitude range for yaw-axis earth-vertical rotation. Zacharias also noted that of the twenty-five studies that Clark reviewed, only one study was reported for pitch and one for roll rotation.

Clark and Stewart [34] later conducted a study with angular acceleration step input stimuli. Using fifty-three test subjects, they found a mean threshold for the perception of the yaw-axis earth-vertical rotation to be 0.41 deg/sec^2. In a separate study, Clark and Stewart [35] studied thresholds about all three earth-vertical axes for eighteen subjects. The mean threshold for yaw and roll was about the same (0.41 deg/sec^2), and was found to be larger for pitch (0.67 deg/sec^2).

Zacharias [16] reported that Mulder first recognized that the product of acceleration magnitude with detection or latency time (Mulder product) is approximately a constant, thus suggesting the existence of an angular velocity threshold. Zacharias [16] noted that Van Egmond demonstrated that the Mulder product could be derived from the torsion-pendulum model, resulting in an estimated value of about 2 deg/sec. Meiry [36] employed a step-response technique to measure latency time of subjects in a motion simulator. For yaw-axis earth-vertical rotation, Meiry [36] obtained a value of 2.6 deg/sec. For roll-axis earth-vertical rotation, a value of 3.0 deg/sec was obtained.

Zacharias [16] then demonstrated that given an infinite detection time corresponding to acceleration below an absolute threshold, the velocity threshold is equal to the acceleration threshold multiplied by the semicircular canals long time constant. He then showed that multiplying the measured accelerations obtained by Clark and Stewart [35] by the long time constants for the corresponding axis obtained by Melvill-Jones, et al. resulted in estimated angular velocity thresholds for each earth-vertical body axis. Zacharias noted that these values were in general agreement with those obtained by Meiry [36].

Benson, et al. [37] reported that threshold measurements were never made with an angular motion stimulus having a trajectory similar to that of a natural head movement. To address this, they performed threshold experiments on a turntable driven by a precision torque motor that generated rotational stimuli about an earth-vertical axis, carrying either a seat with the subject seated upright, or a stretcher that allowed the subject to lay either supine or on their right side. The following results in Table 3.2 were obtained for all three earth-vertical axes, and are compared to the thresholds reported by Reid and Nahon [9] that include the roll and yaw thresholds reported by Meiry [36] and the pitch threshold Zacharias [16] estimated from the acceleration thresholds obtained by Clark and Stewart [35].

Table 3.2. Comparison of Body Axis Angular Velocity Thresholds in deg/sec.

Reference	Roll	Pitch	Yaw
Reid and Nahon	3.0	3.6	2.6
Benson, et al.	2.0	2.0	1.6

Zacharias [16] reported a review of linear acceleration threshold studies by Peters, in which Peters noted a one order-of-magnitude range in measured threshold (0.002 to 0.02 g). Possible contributions to this variation included the variability between subjects, the type of stimulus used (e.g., sinusoidal vs. step), the definition of threshold, and the head axis orientation with respect to the stimulus. Zacharias [16] noted that only one of the reviewed studies used a linear acceleration stimulus in the earth-vertical direction, in which Mach obtained an acceleration threshold of 0.012 g. Subsequent vertical motion threshold measurements reported by Zacharias [16] show almost a one order-of-magnitude difference, from 0.0085 g to 0.005 g.

Zacharias [16] also reported threshold measurements with a linear acceleration stimulus in the horizontal plane with subjects lying supine, noting that similar thresholds to vertical motion are expected since this geometry implies an alignment of the stimulus acceleration vector with the vertical body axis. Zacharias [16] noted that these results are confirmed by an estimate of 0.01g obtained by Meiry [36] (using a linear motion cart and acceleration step inputs). However, Zacharias [16] then noted that the most common test protocol for threshold measurements of horizontal stimuli has been with subjects seated upright. Meiry [36] noted that with the utricle inclined at about 30 degrees above the horizontal head plane, horizontal thresholds might be expected to be lower than vertical thresholds by a factor of cos 30/sin 30, or about a factor of 1.7.

Benson, et al. [38] performed threshold experiments with a test stimulus consisting of a single discrete movement having an acceleration trajectory that approximated a sine wave. This stimulus is similar to the trajectory used by Benson, et al. [37] in determining rotational thresholds. Motion stimuli were generated by a horizontal linear oscillator guided by externally pressurized aerostatic bearings, supporting a seat assembly that could be adjusted so that the stimuli axis was parallel to the axis of motion of the carriage. Benson, et al. [38] obtained thresholds for the x-, y-, and z-axes that are noted in Table 3.3, and are compared to thresholds reported by Reid and Nahon [9]. Reid and Nahon [9] reported acceleration threshold values that were based on the studies reported by Zacharias [16]. The z-axis threshold is about the same as that Zacharias [16] reported was obtained from the Mach study reported by Peters. The x- and y-axis acceleration is about a factor of 1.7 less than that noted for the z-axis, which is consistent with the observation noted by Meiry [36]. Benson, et al. [38] noted

that these thresholds are within the ranges reported in other studies; in particular the results obtained by Meiry [36], who employed a step acceleration stimulus. The significantly higher threshold for the z-axis was noted by Benson, et al. to be consistent with the findings of studies employing sustained oscillatory or step acceleration stimuli.

Table 3.3. Body Axis Linear Acceleration Thresholds in m/sec^2.

Reference	X-Axis	Y-Axis	Z-Axis
Benson, et al.	0.0625	0.0569	0.154
Reid and Nahon	0.17	0.17	0.28

The linear and angular motion thresholds presented in Tables 3.2 and 3.3 respectively are effective, or "indifference" thresholds that are more appropriate for the pilot-vehicle environment than absolute thresholds that result from the detection of a single task in an ideal laboratory environment. Zacharias [16] noted that higher indifference thresholds during active tracking are justified because of less attention given to motion cues due to workload. Gundry [2] showed an increase of 40% when the subject is loaded with an arithmetic task. Hosman and Van der Vaart [21] observed a similar increase in roll and pitch thresholds when their subjects were loaded with either a control task or an auditory discrimination task.

Zacharias [16] noted that a latency dependence on angular acceleration is observed, and a velocity threshold model similar to angular motion can be proposed. Meiry [36] measured detection latencies as a function of linear acceleration step size. This model assumed a velocity threshold exists such that acceleration thresholds required T seconds to be detected. In response to a velocity ramp input, the model predicted a perceived velocity. For subjects seated upright, the model resulted in a linear velocity threshold of 0.02 g-sec or about 0.2 m/sec for longitudinal motion. Zacharias [16] noted

that Melvill-Jones and Young used a similar analysis of detection time and acceleration from both their own experiments and those of Meiry [36]. Based on Meiry's data, they proposed a value of 0.22 m/sec for both longitudinal and vertical motion.

The angular velocity and linear acceleration thresholds given in Tables 3.2 and 3.3 are used in the development of the linear optimal algorithm discussed in Chapter 4. The linear velocity thresholds mentioned in the last paragraph are incorporated in the integrated human perception model discussed in Chapter 5 and implemented in the nonlinear motion cueing algorithm developed in Chapter 6. The integrated perception model also includes the angular velocity thresholds of Table 3.2.

4. Linear Optimal Motion Cueing Algorithm

4.1. Problem Description

In developing a set of linear washout filters, the problem is to determine a transfer function matrix $\mathbf{W(s)}$ that relates the desired simulator motion input to the aircraft input such that a cost function constraining the pilot sensation error (between simulator and aircraft) is minimized. The structure of this problem is illustrated in Figure 4.1.
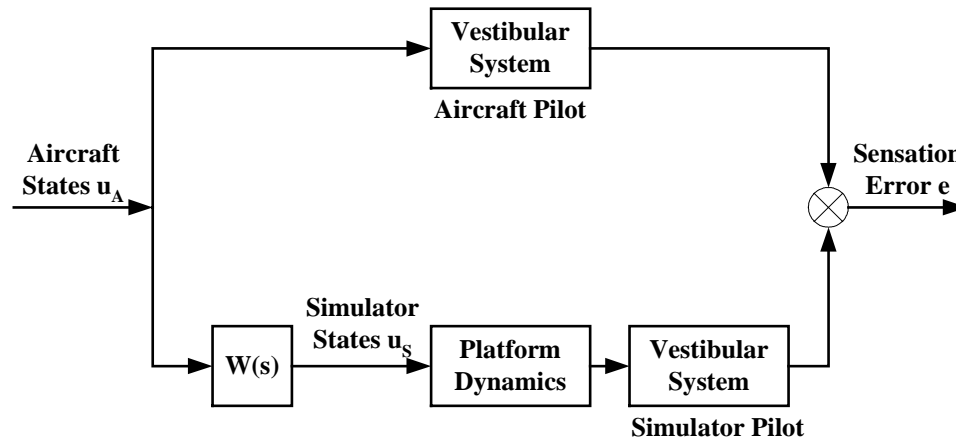
Figure 4.1. Linear Optimal Algorithm Problem Structure.

A mathematical model of the human vestibular system is used in the filter development. The optimal algorithm generates the desired transfer functions $\mathbf{W(s)}$ by an off-line program, which are then implemented on-line. $\mathbf{W(s)}$ will relate the simulator motion states to the aircraft states by $\mathbf{u_S} = \mathbf{W(s)} \times \mathbf{u_A}$. The simulator states $\mathbf{u_S}$ are then used to generate the desired motion platform commands.

In the original development, the washout filters were applied in the pilot head reference frame. Reid and Nahon [9] noted that this frame selection was chosen to eliminate sensation cross-couplings that made the development of $\mathbf{W(s)}$ more complicated. Wu [13] demonstrated that this location of the center of rotation at the pilot's head resulted in excessively large actuator extensions in some input cases. He

suggested that the optimal algorithm be reformulated in the simulator reference frame with the center of rotation located at the centroid of the simulator motion-base.

The question has arisen as to what aircraft and simulator control inputs are the most appropriate for the optimal algorithm. The previous developments suggested a control input for either the longitudinal or lateral mode with linear acceleration and angular displacement as control inputs. Wu [13] developed an approach using linear acceleration and angular acceleration for the longitudinal mode. This approach showed advantages in controlling additional modes that were not available in the original development. In addition, since the semicircular canals behave as a transducer for angular velocity input in the range of normal head movements, an approach using angular velocity as an input is desired. In this research an optimal algorithm based on simulated aircraft angular velocity inputs is developed.

4.2. Algorithm Development

4.2.1. Longitudinal Mode

The algorithm development with angular velocity input for the longitudinal (pitch/surge) mode is given below. The input **u** is formulated as

$$\mathbf{u} = \begin{bmatrix} \dot{\theta} \\ a_x \end{bmatrix} = \begin{bmatrix} u_1 \\ u_2 \end{bmatrix}, \tag{4.1}$$

where $\dot{\theta}$ is angular velocity, and a_x is the translational acceleration, with each term respectively set equal to u_1 and u_2.

The sensed rotational motion $\hat{\dot{\theta}}$ is related to u_1 by the semicircular canals model of Eq. (3.8):

$$\hat{\theta} = \frac{G_{SCC}\tau_1\tau_a s^2 (1 + \tau_L s)}{(1 + \tau_a s)(1 + \tau_1 s)(1 + \tau_2 s)} u_1, \tag{4.2}$$

where the semicircular canals time constants τ_1, τ_2, τ_a, and τ_L are given in Eq. (3.8), and G_{SCC} is the angular velocity threshold that scales the response to threshold units. Eq. (4.2) can be rewritten as

$$\hat{\theta} = \frac{T_4 s^3 + T_3 s^2}{s^3 + T_2 s^2 + T_1 s + T_0} u_1, \tag{4.3}$$

where

$$T_0 = \frac{1}{\tau_a \tau_1 \tau_2}, \; T_1 = \frac{\tau_a + \tau_1 + \tau_2}{\tau_a \tau_1 \tau_2}, \; T_2 = \frac{\tau_1 \tau_2 + \tau_a(\tau_1 + \tau_2)}{\tau_a \tau_1 \tau_2}, \; T_3 = G_{SCC}/\tau_2, \; \text{and } T_4 = G_{SCC}\tau_L/\tau_2,$$

and can be defined in state space notation as

$$\dot{\mathbf{x}}_{SCC} = \mathbf{A}_{SCC}\mathbf{x}_{SCC} + \mathbf{B}_{SCC}\mathbf{u}$$
$$\hat{\theta} = \mathbf{C}_{SCC}\mathbf{x}_{SCC} + \mathbf{D}_{SCC}\mathbf{u}, \tag{4.4}$$

where in observer canonical form,

$$\mathbf{A}_{SCC} = \begin{bmatrix} -T_2 & 1 & 0 \\ -T_1 & 0 & 1 \\ -T_0 & 0 & 0 \end{bmatrix}, \; \mathbf{B}_{SCC} = \begin{bmatrix} T_3 - T_2 T_4 & 0 \\ -T_1 T_4 & 0 \\ -T_0 T_4 & 0 \end{bmatrix}, \; \mathbf{C}_{SCC} = \begin{bmatrix} 1 & 0 & 0 \end{bmatrix}, \text{ and } \mathbf{D}_{SCC} = \begin{bmatrix} T_4 & 0 \end{bmatrix}.$$

The sensed specific force $\hat{f}_x$ is related to the stimulus specific force f_x by the otolith model of Eq. (3.29):

$$\hat{f}_x(s) = G_{OTO} K'_{OTO} \frac{(s + A_0)}{(s + B_0)(s + B_1)} f_x(s), \tag{4.5}$$

where A_0, B_0, B_1, and K'_{OTO} are computed parameters of the otolith model as given in Eq. (3.29), and G_{OTO} is the linear acceleration threshold that scales the response to threshold units.

For the center of rotation at the centroid of the motion platform, the specific force is

$$f_x = a_x + g\theta - R_{Sz}\ddot{\theta}, \tag{4.6}$$

where R_{Sz} is the radius from the motion platform centroid to the pilot's head. In terms of u_1 and u_2, Eq. (4.6) is transformed into the Laplace domain, where

$$f_x(s) = u_2(s) + \left(g\frac{1}{s} - R_{Sz}s \right) u_1(s). \tag{4.7}$$

Substituting (4.7) into (4.5) results in

$$
\begin{aligned}
\hat{f}_x(s) &= G_{OTO} K'_{OTO} \frac{(s + A_0)}{(s + B_0)(s + B_1)} \left[u_2 + \left(g\frac{1}{s} - R_{Sz}s \right) u_1 \right] \\
&= G_{OTO} K'_{OTO} \frac{(s + A_0)}{(s + B_0)(s + B_1)} \left[\left(g\frac{1}{s} - R_{Sz}s \right) \quad 1 \right] \mathbf{u} \\
&= G_{OTO} K'_{OTO} \left[\frac{-R_{Sz}s^3 - R_{Sz}A_0 s^2 + gs + gA_0}{s(s + B_0)(s + B_1)} \quad \frac{(s + A_0)}{(s + B_0)(s + B_1)} \right] \mathbf{u}.
\end{aligned} \tag{4.8}
$$

Note that in Eq. (4.8) the system equation becomes realizable with the inclusion of the otolith break frequency B_1, which was neglected by both Reid and Nahon [9] and Wu [13] in their respective optimal algorithm formulations. Rearranging and taking derivatives results in the differential equation

$$
\begin{aligned}
\dddot{\hat{f}}_x + (B_0 + B_1)\ddot{\hat{f}}_x + B_0 B_1 \hat{f}_x &= \\
G_{OTO} K'_{OTO} \Big[R_{Sz}(B_0 + B_1 - A_0)\dot{u}_1 + (g + R_{Sz}B_0 B_1)u_1 &+ gA_0 \int u_1 dt + \dot{u}_2 + A_0 u_2 \Big],
\end{aligned} \tag{4.9}
$$

which can be rewritten as

$$\dddot{\hat{f}}_x + a\ddot{\hat{f}}_x + b\hat{f}_x = c\dot{u}_1 + du_1 + e\int u_1 dt + f\dot{u}_2 + gu_2, \tag{4.10}$$

and can then be defined in state space notation as

$$\dot{\mathbf{x}}_{\text{OTO}} = \mathbf{A}_{\text{OTO}}\mathbf{x}_{\text{OTO}} + \mathbf{B}_{\text{OTO}}\mathbf{u}$$
$$\hat{f}_x = \mathbf{C}_{\text{OTO}}\mathbf{x}_{\text{OTO}} + \mathbf{D}_{\text{OTO}}\mathbf{u},$$

(4.11)

where $\mathbf{x}_{\text{OTO}}$ are the otoliths states, and

$$\mathbf{A}_{\text{OTO}} = \begin{bmatrix} 0 & 1 & 0 & 0 & 0 \\ -b & -a & 1 & 0 & 0 \\ 0 & 0 & 0 & 0 & 0 \\ 0 & 0 & 0 & 0 & 1 \\ 0 & 0 & 0 & -b & -a \end{bmatrix}, \quad \mathbf{B}_{\text{OTO}} = \begin{bmatrix} c & 0 \\ d - ac & 0 \\ e & 0 \\ 0 & f \\ 0 & h - af \end{bmatrix},$$

$$\mathbf{C}_{\text{OTO}} = \begin{bmatrix} 1 & 0 & 0 & 1 & 0 \end{bmatrix}, \quad \mathbf{D}_{\text{OTO}} = \begin{bmatrix} -G_{OTO}K'_{OTO}r_{Sz} & 0 \end{bmatrix}.$$

The representations in Eqs. (4.4) and (4.11) can be combined to form a single representation for the human vestibular model:

$$\dot{\mathbf{x}}_V = \mathbf{A}_V\mathbf{x}_V + \mathbf{B}_V\mathbf{u}$$
$$\hat{\mathbf{y}}_1 = \mathbf{C}_V\mathbf{x}_V + \mathbf{D}_V\mathbf{u},$$

(4.12)

where $\mathbf{x}_V$ and $\hat{\mathbf{y}}_V$ are, respectively, the combined states and sensed responses, and $\mathbf{A}_V$, $\mathbf{B}_V$, $\mathbf{C}_V$, and $\mathbf{D}_V$ represent the vestibular models as one set of state equations:

$$\mathbf{A}_V = \begin{bmatrix} \mathbf{A}_{\text{SCC}} & \mathbf{0} \\ \mathbf{0} & \mathbf{A}_{\text{OTO}} \end{bmatrix}, \quad \mathbf{B}_V = \begin{bmatrix} \mathbf{B}_{\text{SCC}} \\ \mathbf{B}_{\text{OTO}} \end{bmatrix}, \quad \mathbf{C}_V = \begin{bmatrix} \mathbf{C}_{\text{SCC}} & \mathbf{0} \\ \mathbf{0} & \mathbf{C}_{\text{OTO}} \end{bmatrix}, \quad \mathbf{D}_V = \begin{bmatrix} \mathbf{D}_{\text{SCC}} \\ \mathbf{D}_{\text{OTO}} \end{bmatrix}.$$

It is assumed that the same sensation model can be applied to both the pilot in the aircraft and the pilot in the simulator as shown in Figure 4.1. We then define the vestibular state error $\mathbf{x}_e = \mathbf{x}_S - \mathbf{x}_A$ (where $\mathbf{x}_S$ and $\mathbf{x}_A$ are the respective vestibular states for the simulator and aircraft), and the pilot sensation error $\mathbf{e}$, resulting in

$$\dot{\mathbf{x}}_e = \mathbf{A}_V\mathbf{x}_e + \mathbf{B}_V\mathbf{u}_S - \mathbf{B}_V\mathbf{u}_A$$
$$\mathbf{e} = \mathbf{C}_V\mathbf{x}_e + \mathbf{D}_V\mathbf{u}_S - \mathbf{D}_V\mathbf{u}_A,$$

(4.13)

where $\mathbf{u}_S$ and $\mathbf{u}_A$ represent the simulator and aircraft inputs as given in Eq. (4.1).

In order to constrain the simulator motion, it is necessary for the control algorithm to explicitly access states such as the linear velocity and displacement of the simulator that will appear in the cost function. For this purpose, additional terms are included in the state equations:

$$\dot{\mathbf{x}}_\mathbf{d} = \mathbf{A}_\mathbf{d}\mathbf{x}_\mathbf{d} + \mathbf{B}_\mathbf{d}\mathbf{u}_\mathbf{S}, \tag{4.14}$$

where $\mathbf{x}_\mathbf{d}$ represents the additional simulator states:

$$\mathbf{x}_\mathbf{d} = \begin{bmatrix} \iiint a_x dt^3 & \iint a_x dt^2 & \int a_x dt & \theta \end{bmatrix}^\mathrm{T},$$

and is related to the simulator input $\mathbf{u}_\mathbf{S}$ by

$$\mathbf{A}_\mathbf{d} = \begin{bmatrix} 0 & 1 & 0 & 0 \\ 0 & 0 & 1 & 0 \\ 0 & 0 & 0 & 0 \\ 0 & 0 & 0 & 0 \end{bmatrix}, \quad \mathbf{B}_\mathbf{d} = \begin{bmatrix} 0 & 0 \\ 0 & 0 \\ 0 & 1 \\ 1 & 0 \end{bmatrix}.$$

The aircraft input $\mathbf{u}_\mathbf{A}$ consists of filtered white noise, and can be expressed as

$$\begin{aligned} \dot{\mathbf{x}}_\mathbf{n} &= \mathbf{A}_\mathbf{n}\mathbf{x}_\mathbf{n} + \mathbf{B}_\mathbf{n}\mathbf{w} \\ \mathbf{u}_\mathbf{A} &= \mathbf{x}_\mathbf{n}, \end{aligned} \tag{4.15}$$

where $\mathbf{x}_\mathbf{n}$ are the filtered white noise states, $\mathbf{w}$ represents white noise, with $\mathbf{A}_\mathbf{n}$ and $\mathbf{B}_\mathbf{n}$ given as

$$\mathbf{A}_\mathbf{n} = \begin{bmatrix} -\gamma_1 & 0 \\ 0 & -\gamma_2 \end{bmatrix}, \quad \mathbf{B}_\mathbf{n} = \begin{bmatrix} \gamma_1 \\ \gamma_2 \end{bmatrix},$$

where γ_1 and γ_2 are the first-order filter break frequencies for each degree-of-freedom. The state equations given in Eqs. (4.13), (4.14), and (4.15) can be combined to form the desired system equation

$$\begin{aligned} \dot{\mathbf{x}} &= \mathbf{A}\mathbf{x} + \mathbf{B}\mathbf{u}_\mathbf{S} + \mathbf{H}\mathbf{w} \\ \mathbf{y} &= \begin{bmatrix} \mathbf{e} & \mathbf{x}_\mathbf{d} \end{bmatrix}^\mathrm{T} = \mathbf{C}\mathbf{x} + \mathbf{D}\mathbf{u}_\mathbf{S}, \end{aligned} \tag{4.16}$$

where **y** is the desired output, and $\mathbf{x} = \begin{bmatrix} \mathbf{x}_e & \mathbf{x}_d & \mathbf{x}_n \end{bmatrix}^T$ represents the combined states.

The combined system matrices **A**, **B**, **C**, **D**, and **H** are then given by

$$\mathbf{A} = \begin{bmatrix} \mathbf{A}_V & 0 & -\mathbf{B}_V \\ 0 & \mathbf{A}_d & 0 \\ 0 & 0 & \mathbf{A}_n \end{bmatrix}, \quad \mathbf{B} = \begin{bmatrix} \mathbf{B}_V \\ \mathbf{B}_d \\ 0 \end{bmatrix}, \quad \mathbf{H} = \begin{bmatrix} 0 \\ 0 \\ \mathbf{B}_n \end{bmatrix}, \quad \mathbf{C} = \begin{bmatrix} \mathbf{C}_V & 0 & -\mathbf{D}_V \\ 0 & \mathbf{I} & 0 \end{bmatrix}, \quad \mathbf{D} = \begin{bmatrix} \mathbf{D}_V \\ 0 \end{bmatrix}.$$

A cost function J is then defined as

$$J = E \left\{ \int_{t_0}^{t_1} \left(\mathbf{e}^T \mathbf{Q} \mathbf{e} + \mathbf{x}_d^T \mathbf{R}_d \mathbf{x}_d + \mathbf{u}_S^T \mathbf{R} \mathbf{u}_S \right) dt \right\}, \tag{4.17}$$

where $E\{\ \}$ is the mathematical mean of statistical variable, **Q** and $\mathbf{R}_d$ are positive semi-definite matrices, and **R** is a positive definite matrix. Eq. (4.17) implies that three variables are to be constrained in the cost function: the sensation error **e** along with the additional terms $\mathbf{x}_d$ and $\mathbf{u}_S$ which together define the linear and angular motion of the platform. The cost function constrains both the sensation error and the platform motion.

The system equation and cost function can be transformed to the standard optimal control form as shown in Kawkernaak and Sivan [39] and noted in Reid and Nahon [9] by the following equations:

$$\begin{aligned} \dot{\mathbf{x}} &= \mathbf{A}'\mathbf{x} + \mathbf{B}\mathbf{u}' + \mathbf{H}\mathbf{w} \\ J' &= E \left\{ \int_{t_0}^{t_1} \left(\mathbf{x}^T \mathbf{R}_1' \mathbf{x} + \mathbf{u}'^T \mathbf{R}_2 \mathbf{u}' \right) dt \right\}, \end{aligned} \tag{4.18}$$

where

$$\mathbf{A}' = \mathbf{A} - \mathbf{B}\mathbf{R}_2^{-1}\mathbf{R}_{12}^T, \quad \mathbf{u}' = \mathbf{u}_S + \mathbf{R}_2^{-1}\mathbf{R}_{12}^T \mathbf{x}, \quad \mathbf{R}_1' = \mathbf{R}_1 - \mathbf{R}_{12}\mathbf{R}_2^{-1}\mathbf{R}_{12}^T,$$
$$\mathbf{R}_1 = \mathbf{C}^T \mathbf{G} \mathbf{C}, \quad \mathbf{R}_{12} = \mathbf{C}^T \mathbf{G} \mathbf{D}, \quad \mathbf{R}_2 = \mathbf{R} + \mathbf{D}^T \mathbf{G} \mathbf{D}, \quad \mathbf{G} = diag[\mathbf{Q}, \mathbf{R}_d].$$

The cost function of Eq. (4.18) is minimized when

$$\mathbf{u}' = -\mathbf{R}_2^{-1}\mathbf{B}^T \mathbf{P}\mathbf{x}, \tag{4.19}$$

where **P** is the solution of the algebraic Riccati equation

$$\mathbf{R}_1' - \mathbf{PBR}_2^{-1}\mathbf{B}^T\mathbf{P} + \mathbf{A}'^T\mathbf{P} + \mathbf{PA}' = \mathbf{0}. \tag{4.20}$$

Substituting Eq. (4.19) into Eq. (4.18) and solving for $\mathbf{u}_S$,

$$\mathbf{u}_S = -\left[\mathbf{R}_2^{-1}\left(\mathbf{B}^T\mathbf{P} + \mathbf{R}_{12}^T\right)\right]\mathbf{x}, \tag{4.21}$$

and defining a matrix $\mathbf{K}$, where $\mathbf{u}_S = \mathbf{Kx}$, results in $\mathbf{K} = \mathbf{R}_2^{-1}\left(\mathbf{B}^T\mathbf{P} + \mathbf{R}_{12}^T\right)$.

$\mathbf{K}$ can be partitioned corresponding to the partition of $\mathbf{x}$ in Eq. (4.16):

$$\mathbf{u}_S = -\begin{bmatrix} \mathbf{K}_1 & \mathbf{K}_2 & \mathbf{K}_3 \end{bmatrix}\begin{bmatrix} \mathbf{x}_e \\ \mathbf{x}_d \\ \mathbf{x}_n \end{bmatrix}. \tag{4.22}$$

Noting that $\mathbf{x}_n = \mathbf{u}_A$, remove the states corresponding to the $\mathbf{x}_n$ partition from Eq. (4.22):

$$\begin{bmatrix} \dot{\mathbf{x}}_e \\ \dot{\mathbf{x}}_d \end{bmatrix} = \begin{bmatrix} \mathbf{A}_V & \mathbf{0} & \mathbf{-B}_V \\ \mathbf{0} & \mathbf{A}_d & \mathbf{0} \end{bmatrix}\begin{bmatrix} \mathbf{x}_e \\ \mathbf{x}_d \\ \mathbf{u}_A \end{bmatrix} + \begin{bmatrix} \mathbf{B}_V \\ \mathbf{B}_d \end{bmatrix}\mathbf{u}_S. \tag{4.23}$$

and substituting Eq. (4.22) into Eq. (4.23) results in

$$\begin{bmatrix} \dot{\mathbf{x}}_e \\ \dot{\mathbf{x}}_d \end{bmatrix} = \begin{bmatrix} \mathbf{A}_V - \mathbf{B}_V\mathbf{K}_1 & -\mathbf{B}_V\mathbf{K}_2 \\ -\mathbf{B}_d\mathbf{K}_1 & \mathbf{A}_d - \mathbf{B}_d\mathbf{K}_2 \end{bmatrix}\begin{bmatrix} \mathbf{x}_e \\ \mathbf{x}_d \end{bmatrix} + \begin{bmatrix} -\mathbf{B}_V\left(\mathbf{I} + \mathbf{K}_3\right) \\ -\mathbf{B}_d\mathbf{K}_3 \end{bmatrix}\mathbf{u}_A. \tag{4.24}$$

After observing the state space form of Eqs. (4.24) and (4.13), the following equations are obtained in the Laplace domain:

$$\mathbf{u}_S(s) = \mathbf{W}(s) \times \mathbf{u}_A(s), \tag{4.25}$$

where

$$\mathbf{W}(s) = \begin{bmatrix} \mathbf{K}_1 & \mathbf{K}_2 \end{bmatrix}\begin{bmatrix} s\mathbf{I} - \mathbf{A}_V + \mathbf{B}_V\mathbf{K}_1 & \mathbf{B}_V\mathbf{K}_2 \\ \mathbf{B}_d\mathbf{K}_1 & s\mathbf{I} - \mathbf{A}_d + \mathbf{B}_d\mathbf{K}_2 \end{bmatrix}^{-1}\begin{bmatrix} \mathbf{B}_V\left(\mathbf{I} + \mathbf{K}_3\right) \\ \mathbf{B}_d\mathbf{K}_3 \end{bmatrix} - \mathbf{K}_3.$$

$\mathbf{W(s)}$ is a matrix of the optimized open-loop transfer functions linking the simulator inputs $\mathbf{u}_S$ to the aircraft inputs $\mathbf{u}_A$. The block diagram for the on-line optimal

algorithm implementation is shown in Figure 4.2. Similar to the NASA adaptive algorithm [7], there are separate filtering channels for the translational and rotational degrees of freedom with the cross-feed path providing the tilt coordination cues.

The aircraft acceleration input vector is first transformed from the aircraft body frame Fr_A to the inertial frame Fr_I using Eq. (2.1). Nonlinear scaling in combination with limiting as described in Section 2.5 is then applied to scale the aircraft inputs. The scaled inertial acceleration $\mathbf{a_A^I}$ is then filtered through the translational filter W_{22} to produce a simulator translational acceleration command $\ddot{\mathbf{S}}_I$. This acceleration is integrated twice to produce the simulator translational position command $\mathbf{S_I}$.

The aircraft angular velocity input $\boldsymbol{\omega}_A^A$ is transformed to the Euler angular rate vector $\dot{\boldsymbol{\beta}}_A$ using Eq. (2.2), and is limited and scaled similar to the translational channel. This input is then passed through the rotational filter W_{11} to produce the vector $\dot{\boldsymbol{\beta}}_{SR}$. The tilt coordination rate $\dot{\boldsymbol{\beta}}_{ST}$ is formed from the acceleration $\mathbf{a_A^I}$ being passed through the tilt coordination filter W_{12}. The summation of $\dot{\boldsymbol{\beta}}_{ST}$ and $\dot{\boldsymbol{\beta}}_{SR}$ yields $\dot{\boldsymbol{\beta}}_S$, which is then integrated to generate $\boldsymbol{\beta}_S$, the simulator angular position command.

The simulator translational position $\mathbf{S^I}$ and the angular position $\boldsymbol{\beta}_S$ are then used to transform the simulator motion from degree-of-freedom space to actuator space as given in Eqs. (2.6) and (2.7), generating the actuator commands required to achieve the desired platform motion.
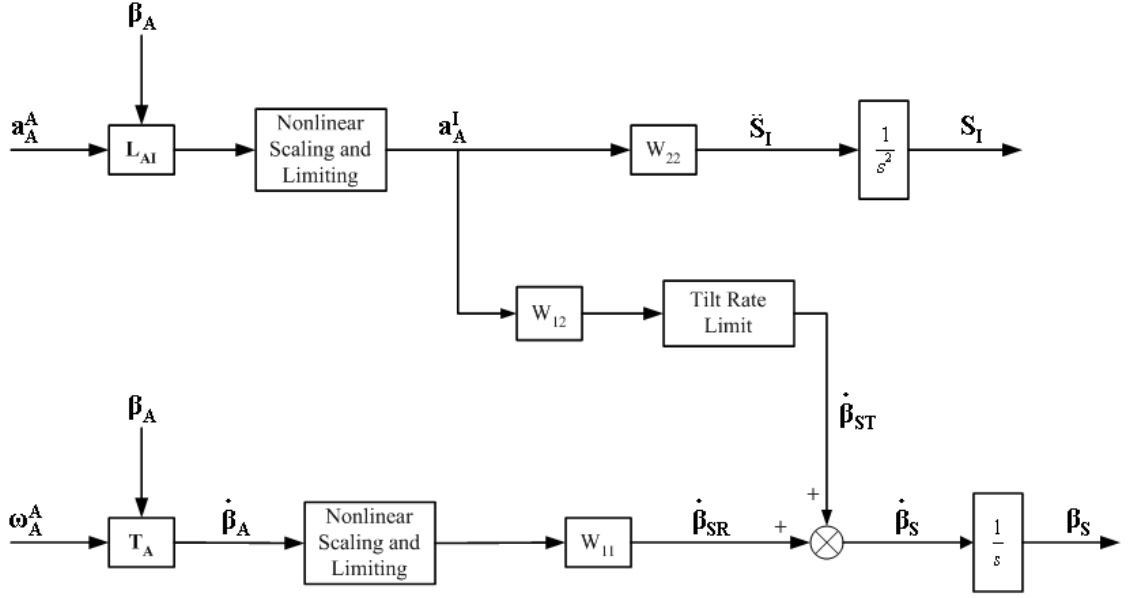
Figure 4.2. Optimal Algorithm Implementation for Longitudinal Mode.

The desired motion cueing filter matrix $\mathbf{W(s)}$ is computed using a set of MATLAB™ scripts. The weighting matrices $\mathbf{Q}$, $\mathbf{R}$, and $\mathbf{R_d}$ given in the cost function of Eq. (4.17) are selected and adjusted to produce the desired motion platform commands. From these weights and the vestibular models the standard optimal control matrices of Eq. (4.18) are computed. The algebraic Riccati equation of Eq. (4.20) is solved with a MATLAB™ function that uses a generalized eigenproblem formulation with a Newton-type refinement presented by Arnold and Laub [40]. The solution for $\mathbf{W(s)}$ is then computed. Common poles and zeros are cancelled in each transfer function, yielding a set of seventh-order filters for the longitudinal mode. These filters are then used in a SIMULINK™ model that generates the linear acceleration and angular velocity responses. If the solution to $\mathbf{W(s)}$ is unsatisfactory, this procedure is repeated by adjusting the elements of the weighting matrices $\mathbf{Q}$, $\mathbf{R}$, and $\mathbf{R_d}$ until the desired results are obtained. The procedure for computing the solution to $\mathbf{W(s)}$ is illustrated in Figure 4.3.
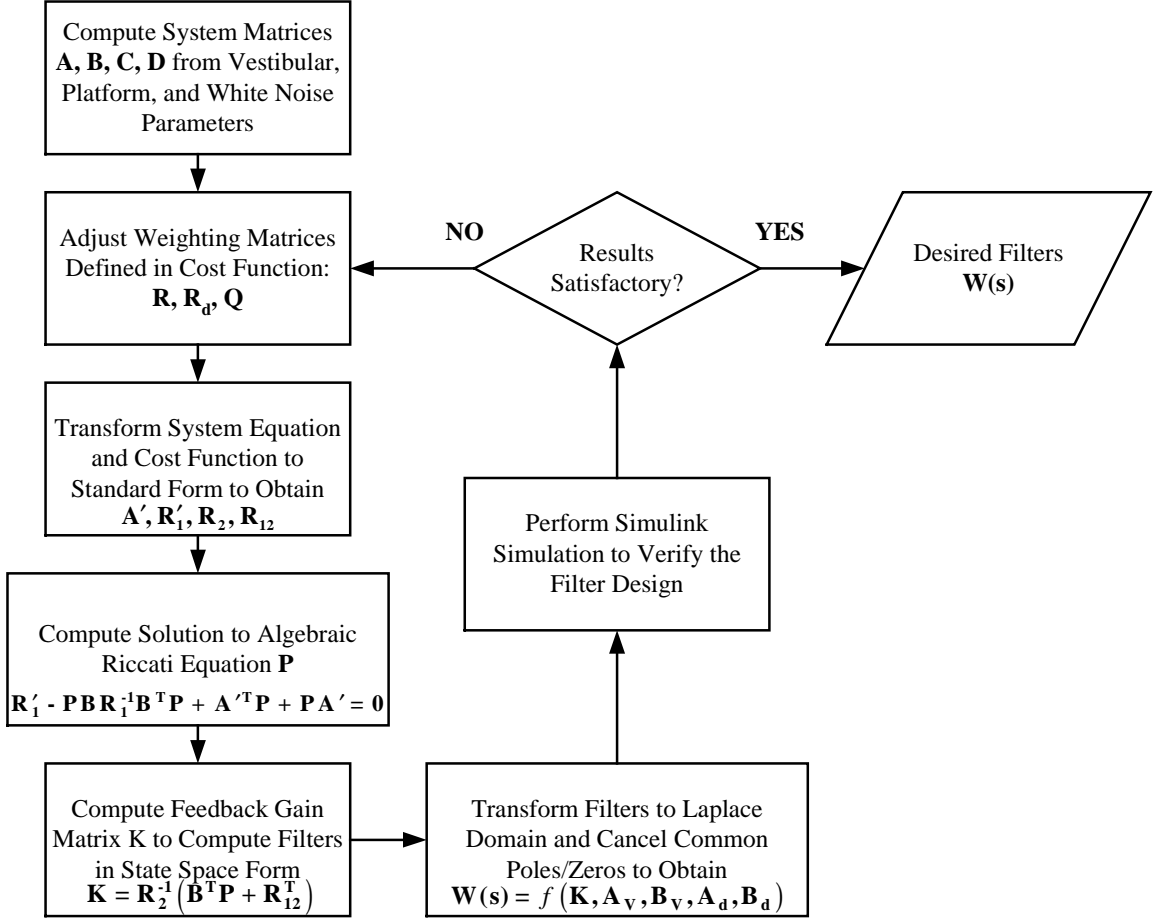
Figure 4.3. Linear Motion Cueing Filter Solution Procedure.

4.2.2. *Lateral Mode*

For the lateral (roll/sway) mode, the algorithm development is analogous to the longitudinal mode. In Eq. (4.1), the inputs $\dot{\theta}$ and a_x are replaced by $\dot{\phi}$ and a_y respectively. The sensed rotational motion $\hat{\dot{\theta}}$ in Eq. (4.2) is replaced by $\hat{\dot{\phi}}$. The specific force f_x and sensed specific force $\hat{f}_x$ become f_y and $\hat{f}_y$ respectively, with Eq. (4.6) now computed as

$$f_y = a_y - g\phi - R_{Sz}\ddot{\phi}. \tag{4.26}$$

These changes thus result in the differential equation given in Eq. (4.9) becoming

$$\ddot{\hat{f}}_y + (B_0 + B_1)\dot{\hat{f}}_y + B_0 B_1 \hat{f}_y =$$

$$G_{OTO} K'_{OTO} \left[R_{Sz}(A_0 - B_0 - B_1)\dot{u}_1 - (g + R_{Sz}B_0 B_1)u_1 - gA_0 \int u_1 dt + \dot{u}_2 + A_0 u_2 \right], \qquad (4.27)$$

which when rewritten as Eq. (4.10), will produce the state equation representation for the otolith model similar to Eq. (4.11), with the same system matrices except $\mathbf{D_{OTO}} = \begin{bmatrix} G_{OTO} K'_{OTO} r_{Sz} & 0 \end{bmatrix}$. The state equation representation for the vestibular model of the form of Eq. (4.13) ultimately results. For this mode the additional platform states given in Eq. (4.14) are now $\mathbf{x_d} = \begin{bmatrix} \iiint a_y dt^3 & \iint a_y dt^2 & \int a_y dt & \phi \end{bmatrix}^{\mathbf{T}}$.

The remaining development is identical in form to Eqs. (4.15) to (4.25), resulting in a matrix of seventh-order transfer functions $\mathbf{W(s)}$ for the lateral mode. The on-line implementation of this mode is identical to Figure 4.2.

4.2.3. Vertical Mode

For the vertical, or heave mode, the single degree-of-freedom input $u = a_z$, with the specific force $f_z = a_z - g$. The otolith model given in Eq. (4.5) then becomes

$$\hat{f}_z(s) = G_{OTO} K'_{OTO} \frac{(s + A_0)}{(s + B_0)(s + B_1)} f_z(s), \qquad (4.28)$$

and can then be defined in state space notation as

$$\begin{aligned} \dot{\mathbf{x}}_{OTO} &= \mathbf{A}_{OTO}\mathbf{x}_{OTO} + \mathbf{B}_{OTO}\mathbf{u} \\ \hat{f}_z &= \mathbf{C}_{OTO}\mathbf{x}_{OTO} + \mathbf{D}_{OTO}\mathbf{u}, \end{aligned} \qquad (4.29)$$

where $\dot{\mathbf{x}}_{OTO}$ are the otolith states for this mode, and

$$\mathbf{A}_{OTO} = \begin{bmatrix} 0 & 1 \\ -B_0 B_1 & -(B_0 + B_1) \end{bmatrix}, \quad \mathbf{B}_{OTO} = \begin{bmatrix} G_O \\ G_{OTO} K'_{OTO}(A_O - B_O - B_1) \end{bmatrix},$$

$$\mathbf{C}_{OTO} = \begin{bmatrix} 1 & 0 \end{bmatrix}, \qquad\qquad \mathbf{D}_{OTO} = \mathbf{0}.$$

Since this mode consists of a single translational degree-of-freedom, the formulation does not include the semicircular canals model, therefore $\mathbf{A_V} = \mathbf{A_{OTO}}$, $\mathbf{B_V} = \mathbf{B_{OTO}}$, and $\mathbf{C_V} = \mathbf{C_{OTO}}$. This results in a sensation model of the same form as Eq. (4.13):

$$\begin{aligned}
\dot{\mathbf{x}}_e &= \mathbf{A_V x_e} + \mathbf{B_V u_S} - \mathbf{B_V u_A} \\
\mathbf{e} &= \mathbf{C_V x_e}.
\end{aligned} \tag{4.30}$$

Similar to the longitudinal mode, additional motion platform states are included in the state equations:

$$\dot{\mathbf{x}}_d = \mathbf{A_d x_d} + \mathbf{B_d u_S}, \tag{4.31}$$

where $\mathbf{x_d}$ represents the additional motion platform states:

$$\mathbf{x_d} = \left[\iiint a_z dt^3 \quad \iint a_z dt^2 \quad \int a_z dt \right],$$

and $\mathbf{A_d}$ and $\mathbf{B_d}$ now become

$$\mathbf{A_d} = \begin{bmatrix} 0 & 1 & 0 \\ 0 & 0 & 1 \\ 0 & 0 & 0 \end{bmatrix}, \quad \mathbf{B_d} = \begin{bmatrix} 0 \\ 0 \\ 1 \end{bmatrix}.$$

The aircraft input $\mathbf{u_A}$ now consists of a single channel of filtered white noise with break frequency γ, and can be expressed as

$$\begin{aligned}
\dot{\mathbf{x}}_n &= -\gamma \mathbf{x_n} + \gamma \mathbf{w} \\
\mathbf{u_A} &= \mathbf{x_n}.
\end{aligned} \tag{4.32}$$

The state equations given in Eqs. (4.30), (4.31), and (4.32) can then be combined to form the desired system equation of the same form as Eq. (4.16), where $\mathbf{y}$ is the desired output, and $\mathbf{x} = \begin{bmatrix} \mathbf{x_e} & \mathbf{x_d} & \mathbf{x_n} \end{bmatrix}^T$ represents the combined states. The remaining development is identical in form to Eqs. (4.16) to (4.25), resulting in a single fourth-order

transfer function W_{22} for the vertical mode. The block diagram of the on-line implementation of this mode is shown in Figure 4.4.

Figure 4.4. Optimal Algorithm Implementation for Vertical Mode.

4.2.4. Yaw Mode

For the yaw mode, the single degree-of-freedom input is $u = \ddot{\psi}$. The state space representation is the same as Eq. (4.4) with output $\hat{\psi}$ replacing $\hat{\theta}$:

$$\dot{\mathbf{x}}_{scc} = \mathbf{A}_{scc}\mathbf{x}_{scc} + \mathbf{B}_{scc}\mathbf{u}$$
$$\hat{\psi} = \mathbf{C}_{scc}\mathbf{x}_{1\sim3} + \mathbf{D}_{scc}\mathbf{u}. \tag{4.33}$$

Since this mode consists of a single rotational input, the formulation does include the otolith model, therefore $\mathbf{A}_V = \mathbf{A}_{scc}$, $\mathbf{B}_V = \mathbf{B}_{scc}$, $\mathbf{C}_V = \mathbf{C}_{scc}$, and $\mathbf{D}_V = \mathbf{D}_{scc}$. This results in a sensation model of the same form as Eq. (4.13):

$$\dot{\mathbf{x}}_e = \mathbf{A}_V\mathbf{x}_e + \mathbf{B}_V\mathbf{u}_S - \mathbf{B}_V\mathbf{u}_A$$
$$e = \mathbf{C}_V\mathbf{x}_e + \mathbf{D}_V\mathbf{u}_S - \mathbf{D}_V\mathbf{u}_A. \tag{4.34}$$

Similar to the longitudinal mode, additional motion platform states are included in the state equations

$$\dot{\mathbf{x}}_d = \mathbf{A}_d\mathbf{x}_d + \mathbf{B}_d\mathbf{u}_S, \tag{4.35}$$

where $\mathbf{x}_d$ represents the additional motion platform states $\mathbf{x}_d = \begin{bmatrix} \int \psi dt & \psi \end{bmatrix}$, and $\mathbf{A}_d$ and $\mathbf{B}_d$ now become

$$\mathbf{A_d} = \begin{bmatrix} 0 & 1 \\ 0 & 0 \end{bmatrix}, \quad \mathbf{B_d} = \begin{bmatrix} 0 \\ 1 \end{bmatrix}.$$

The aircraft input $\mathbf{u_A}$ now consists of a single channel of filtered white noise with break frequency γ, and can be expressed as

$$\dot{\mathbf{x}}_\mathbf{n} = -\gamma \mathbf{x}_\mathbf{n} + \gamma \mathbf{w}$$
$$\mathbf{u_A} = \mathbf{x_n}.$$
(4.36)

The state equations given in Eqs. (4.34), (4.35), and (4.36) can then be combined to form the desired system equation of the same form as Eq. (4.16), where $\mathbf{y}$ is the desired output, and $\mathbf{x} = \begin{bmatrix} \mathbf{x_e} & \mathbf{x_d} & \mathbf{x_n} \end{bmatrix}^T$ represents the combined states. The remaining development is identical in form to Eqs. (4.16) to (4.25), resulting in a single fourth-order transfer function W_{11} for the yaw mode. The block diagram for the on-line implementation for this mode is shown in Figure 4.5.
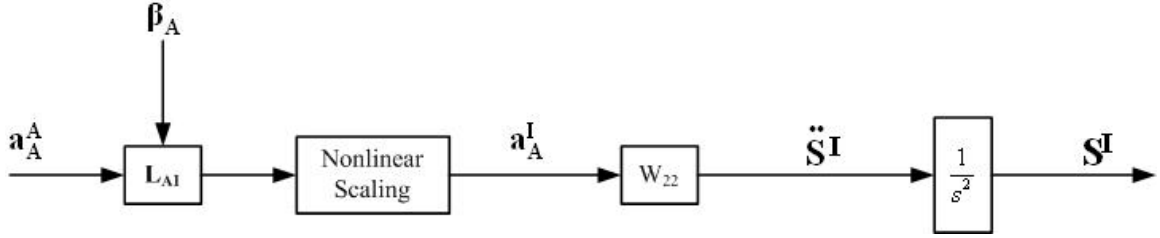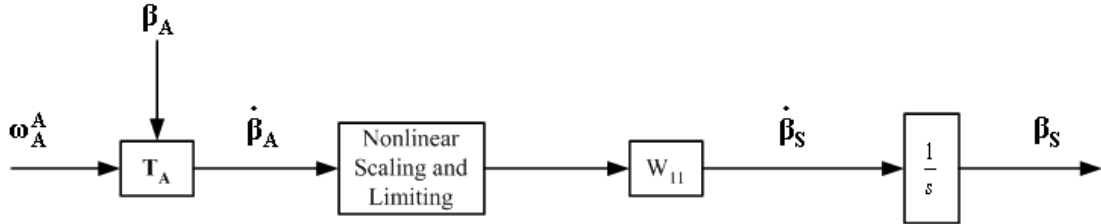

Figure 4.5. Optimal Algorithm Implementation for Yaw Mode.

4.3. Pilot Tuning of the Algorithm

A set of motion cueing filters for the longitudinal, lateral, vertical, and yaw modes was developed using the solution procedure given in Figure 4.3. The new semicircular canals model given in Eq. (3.8) was implemented, along with the Young-Meiry otolith model from Eq. (3.11) that was previously implemented [13], [9]. Filtered white noise break frequencies were initially set at 1 rad/sec for each degree-of-freedom. In some instances, the MATLAB™ error message "cannot order eigenvalues; spectrum too near

65

imaginary axis" resulted from the motion cueing filter development. This error occurs when the Hamiltonian matrix for the Riccati equation has eigenvalues on or very near the imaginary axis. To resolve this, a small change to any of the weights was needed to obtain a successful solution to the Riccati equation as suggested by Brogan [41]. Nonlinear scaling coefficients for each degree-of-freedom were based upon those chosen by Wu [13].

In order to determine the nonlinear gain coefficients for each degree-of-freedom that resulted in the most desired pilot performance, a trained simulator pilot executed a series of pilot controlled maneuvers with the optimal algorithm on the NASA Langley Visual Motion Simulator (VMS) described in Section 2.1. A series of maneuvers were first executed with the coefficients determined prior to testing. Coefficients for each degree-of-freedom were then adjusted until the simulator pilot subjectively felt the desired perception and performance were reached, while ensuring that the simulator motion platform limits were not exceeded. The following maneuvers were executed for the algorithm:

> Straight Approach and Landing (with varying wind from head to tail)
> Offset Approach and Landing (with and without turbulence)
> Pitch, Roll, and Yaw Doublets
> Throttle Increase and Decrease
> Coordinated Turn
> Ground Maneuvers (taxiing, effect of aircraft brakes)
> Takeoff from Full Stop.

The optimal algorithm resulted in motion cues with which the simulator pilot commented he had more control and confidence as compared to the NASA adaptive algorithm. For both pitch and roll doublets, a fast response was observed when changing directions. On takeoffs, the optimal algorithm was found to be easier to pitch up to the

66

desired attitude and control the aircraft. A noticeably large side force was observed with the coordinated turn maneuver. By reducing the gains for the roll degree-of-freedom, this side force was reduced to a minimal sensation. The pitch gains were decreased to reduce the likelihood of entering the braking region or exceeding the actuator limits. Reducing the gains for both roll and pitch degrees-of-freedom still yielded desirable motion cues.

The severe turbulence effects that were included with the offset approach and landing maneuver were hardly noticeable. An increase of the vertical gain coefficients resulted in increased cues, but still less than satisfactory. This increase in the vertical gains (coupled with an increase of the surge gains) resulted in forward surge cues that are more coordinated with the pitch cues, and a larger aft surge cue (initially, the aft cue was noticeably smaller than the forward cue).

The effect of the otolith model upon the vertical filter characteristics was investigated. Figure 4.6 compares the frequency response of the original heave filter using the Young-Meiry model with the response using the proposed otolith model given in Eq. (3.29). Note that the original filter results in a gain decrease starting at about 5 rad/sec, while the proposed model filter shows the gain unchanged for the same high frequencies. For the original filter, the filtered white noise break frequency γ was increased to 4π rad/sec (2 Hz) to remove a right-half plane zero that resulted in a large false cue at both the onset and end of the pulse. For the revised filter with the proposed otolith model, this break frequency was reduced to 1 rad/sec, resulting in the specific force cue shown in Figure 4.7. The proposed model filter results in a faster onset cue that approaches the aircraft step input, and a faster washout that reduces the maximum simulator displacement while sustaining the peak onset magnitude.
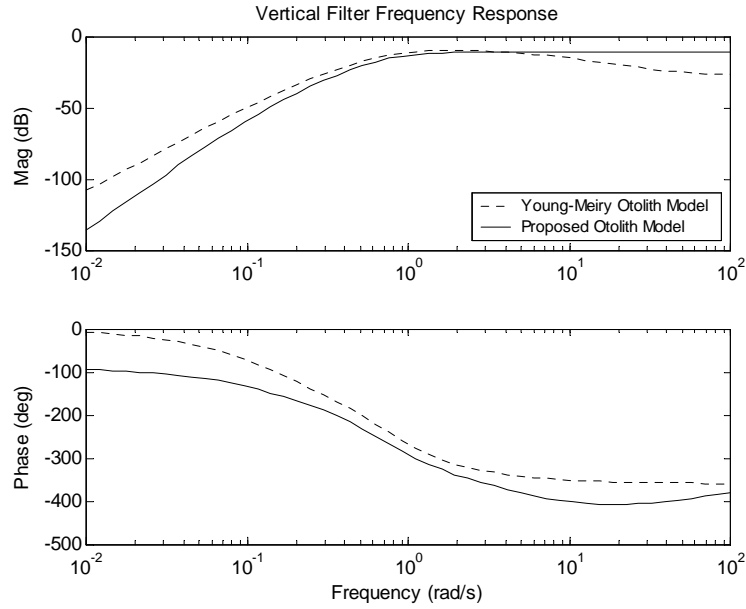
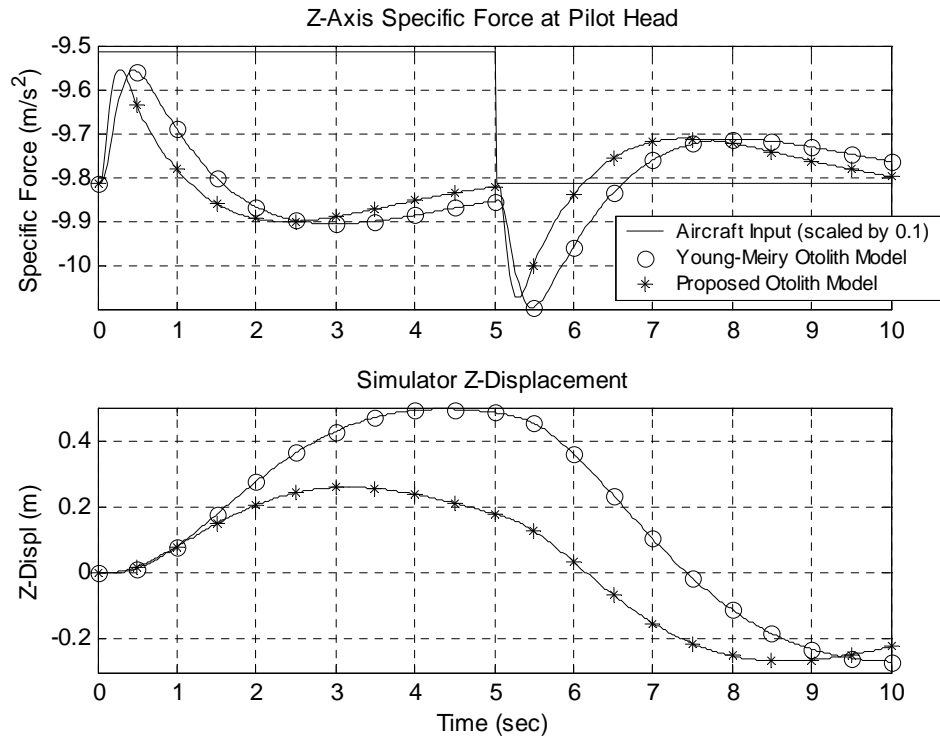**Figure 4.6. Vertical Filter Frequency Responses with Young-Meiry and Proposed Otolith Models.**

Figure 4.7. Specific Force Responses with Young-Meiry and Proposed Vertical Filters.

68

A filter matrix $\mathbf{W(s)}$ is then generated for the pitch/surge mode using the proposed otolith model. In order to eliminate a singular response, both the lead time constant τ_L and the short time constant τ_2 are removed from the semicircular canals model implemented in the motion cueing algorithm:

$$\hat{\theta} = \frac{G_{SCC}\tau_1\tau_a s^2}{(1+\tau_a s)(1+\tau_1 s)}u_1.$$

(4.37)

Eq. (4.37) can be rewritten as

$$\hat{\theta} = \frac{G_{SCC}s^2}{s^2 + T_1 s + T_0}u_1,$$

(4.38)

where T_0 and T_1 become

$$T_0 = \frac{1}{\tau_a\tau_1}, \quad T_1 = \frac{\tau_a + \tau_1}{\tau_a\tau_1},$$

and can be defined in state space notation as

$$\dot{\mathbf{x}}_{\mathbf{scc}} = \mathbf{A}_{\mathbf{scc}}\mathbf{x}_{\mathbf{scc}} + \mathbf{B}_{\mathbf{scc}}\mathbf{u}$$
$$\hat{\theta} = \mathbf{C}_{\mathbf{scc}}\mathbf{x}_{\mathbf{scc}} + \mathbf{D}_{\mathbf{scc}}\mathbf{u},$$

(4.39)

where in observer canonical form,

$$\mathbf{A}_{\mathbf{scc}} = \begin{bmatrix} -T_1 & 1 \\ -T_0 & 0 \end{bmatrix}, \quad \mathbf{B}_{\mathbf{scc}} = \begin{bmatrix} -G_{SCC}\tau_1 & 0 \\ -G_{SCC}\tau_0 & 0 \end{bmatrix}, \quad \mathbf{C}_{\mathbf{scc}} = \begin{bmatrix} 1 & 0 \end{bmatrix}, \text{ and } \mathbf{D}_{\mathbf{scc}} = \begin{bmatrix} G_{SCC} & 0 \end{bmatrix}.$$

There is one less state as compared to Eq. (4.4), which in turn results in a matrix of sixth-order filters for $\mathbf{W(s)}$. The translational break frequency γ_2 was increased from 1 to 4π rad/sec for the original filters, eliminating a false specific force cue at onset. For the proposed model filters, γ_2 is reduced to π rad/sec to produce a faster onset cue. The semicircular canals threshold G_{SCC} was reduced to 2.0 deg/sec, the value obtained by Benson, et al. [37], to reduce the magnitude of the tilt coordination rate. Figure 4.8

compares the responses to a ramp to step input for both filters. Using the proposed

otolith model in the filter development results in a faster onset ramp for the specific force

response, with a faster onset and reduced magnitude for the tilt coordination rate. For

both the original and revised filters, the weight component $\mathbf{Q}$(2,2) needed to be increased

from 1 to 10 to produce the magnitude of the specific force cues shown in Figure 4.8.
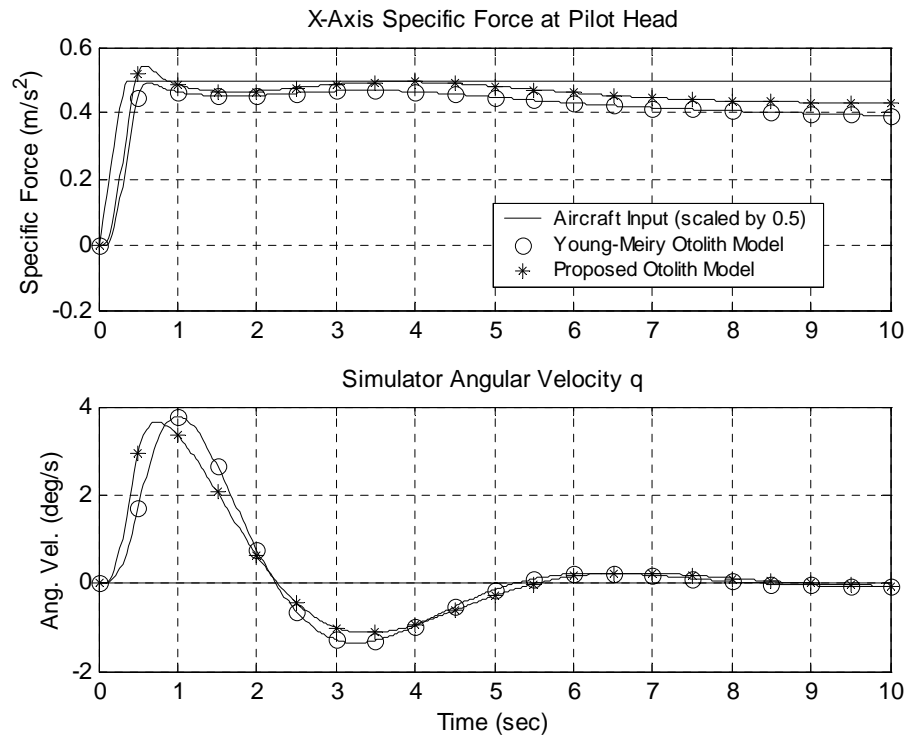
Figure 4.8. Responses to a Surge Ramp to Step Input with Original and Revised Longitudinal Filters.

Figure 4.9 compares responses to a lateral (sway) half sine input for both the original and revised filters. Since the algorithm development is similar to the longitudinal mode, the effect of the change of otolith models upon the motion cues is expected to be the same as the longitudinal mode. Note that the revised filter has a faster onset ramp with a larger specific force cue.
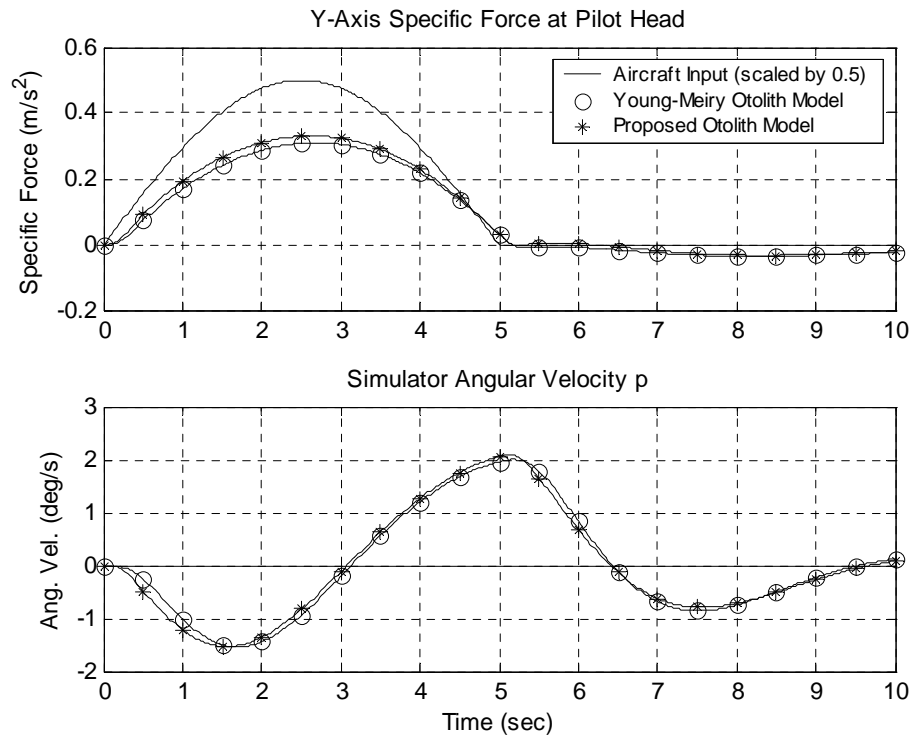
Figure 4.9. Responses to a Sway Half Sine Input with Original and Revised Lateral Filters.

A summary of the optimal algorithm parameters for each of the four modes (longitudinal, lateral, vertical, and yaw) is given in Appendix B, Table B.1. The filter characteristics for both the original and revised linear motion cueing filters $\mathbf{W(s)}$ are also given in Appendix B, in Tables B.2 and B.3 respectively.

This page intentionally left blank.

5. Integrated Human Perception Model

The purpose of this study is to develop a model of human motion perception that can be readily implemented into the nonlinear motion cueing algorithm discussed in the next chapter. This integrated human perception model includes both vestibular and visual motion stimuli and incorporates the interaction between the vestibular and visual stimuli. This study is based on the literature presented by several researchers who investigated both the characteristics of visually induced motion sensation and the visual-vestibular interaction.

5.1. Visually Induced Self-motion

The visually induced effect on self-motion perception is commonly known as vection. Circularvection refers to visually induced rotational motion, in particular yaw, but also visually induced pitch and roll. Linearvection refers to visually induced translational motion. One common experience of linearvection is the illusion of moving backwards when seated in a stationary train car as the adjacent train in the station begins to slowly move forward. The self-motion response to a full visual field surround rotating about a vertical axis has been described by Young [42]:

> The response to a full field surround which suddenly begins to move at constant velocity is rather startling, although quite repeatable. At first, the veridical motion is sensed – the surround appears to be moving and the subject feels himself stationary. After a period of typically two to five seconds, the visual field appears to slow down, often to a stop, and the subject perceives himself as rotating in the opposite direction. The sensation of rotation builds to a maximum over a period of three to ten seconds, rising approximately as an exponential.

Young [42] then noted that in order to achieve a complete "saturation" of this effect, in which the visual field is perceived to be entirely stationary, it is useful to have a wide, compelling field of view in the periphery, moving uniformly at speeds less than 60

degrees per second. Young then noted that if the visual surround is allowed to accelerate smoothly to its final velocity, at accelerations comparable to the acceleration thresholds of the semicircular canals, then the self-motion is more likely to be perceived as a smooth, continuous development of circularvection.

Visually induced self-motion has been explored for rotations about both the earth-horizontal and earth-vertical axes, and along all three linear axes. The general characteristics of visually induced self-motion in the absence of confirming vestibular stimuli have been reported by Young [43] and supported by other researchers. Young noted two distinct classes of visual cues for flight simulation: the foveal cues, the high acuity, high information-dense central field cues that must be "read" to be interpreted, and the peripheral cues, the wide-field, lower acuity, rapidly moving cues that generate non-cognitive motion perception. These cues correspond respectively to the high static acuity, cone-filled fovea, and the high dynamic sensitivity, rod-filled periphery of the retina.

Brandt, et al. [44] demonstrated that the peripheral visual field was of primary importance in stimulating self-motion over the central visual field. They observed that when the central visual field is masked up to 120 degrees in diameter, circularvection diminished very little. Conversely, if peripheral vision was precluded, stimulation of the central field of up to 60 degrees in diameter produced an almost exclusive exocentric perception of the moving visual surround and a very weak self-motion perception. They also found that when equal stimulus areas are presented either foveally or peripherally, that stimulation of the peripheral visual field is more favorable to stimulate self-motion perception.

Brandt, et al. [45] demonstrated that for circularvection, background stimulation is dominant over foreground stimulation. They showed that movement in the background induced the apparent self-motion, while if the foreground moved the stationary background inhibited circularvection. They showed that if a stationary pattern is attached to the background, the circularvection latencies are increased significantly, thus indicating an inhibitory effect of circularvection due to the presence of stationary contrasts in the background. Howard and Howard [46] later demonstrated that the presence of stationary objects in the foreground significantly increases circularvection and reduces the latency of onset to circularvection.

The spatial frequency of the scene determines its effectiveness in generating self-motion. Held, et al. [47] demonstrated this by quantifying the visual border placement and velocity necessary to achieve a visually induced roll. In their experiment the observer viewed a circular disc through a monocular color-corrected lens, effectively producing an extended visual field. The disc was covered with a random pattern of spots with areas that were masked off, producing a set of ring-shaped displays. They found that, in general, the magnitude of visually induced tilt increased with field size, with the use of a large number of rings subtending small solid angles in the peripheral areas being more effective than the same for central areas. Young [43] commented that the peripheral field display should also have a sufficient number of borders such as stars, clouds, or ground features to induce the perceived self-motion.

The visual field velocity determines the magnitude of the self-motion up to a saturation velocity that most likely corresponds to the blurring of the visual field associated with increased dynamic acuity [43]. Saturation of vection occurs when the

field appears stationary in space and all motion is perceived self-motion or egocentric. Brandt, et al. [45] observed that the velocity of apparent yaw self-motion matches the stimulus speeds up to 90 to 120 degrees per second. Young and Oman [48] observed for a pitch stimulus, the visually induced pitch increases with field speed up to a stimulus of about 40 to 60 degrees per second. They also observed a limit of about 40 to 60 degrees per second for visually induced roll that was confirmed by Held, et al. [47]. Young [43] noted that saturation occurs for linearvection up to 1 meter per second, which was the maximum stimulus velocity tested Berthoz, et al., [49].

Young [43] found that the approximate frequency response for both circularvection and linearvection is flat from static inputs up to a frequency of 0.1 Hz, beyond which it decreases at least as rapidly as a first-order filter. Berthoz, et al. [49] confirmed these results for forward linearvection, with similar results obtained for visually induced pitch [50] and for yaw circularvection [51].

5.2. Latency of Onset to Vection

Young [43] noted that the onset delay, or the latency, of visually induced motion is highly variable among individuals. Repeated exposures will reduce this latency, as does the development of the appropriate mental set, thus allowing for the development of vection. The latency of onset to either circularvection or linearvection has an impact on the perception of motion in flight simulation. Several experimenters have quantified this phenomenon.

Brandt, et al. [44] conducted experiments using a rotating chair located in the center of a closed cylindrical drum 1.5 meters in diameter, whose inner walls were painted with alternating vertical black and white stripes subtending 7 degrees of visual

angle. To stabilize the direction of the chair, the subjects were asked to fixate on a one-degree luminous spot mounted on the chair and presented in a position straight ahead of the subject. The yaw stimuli consisted of drum rotations moving at either constant velocity (10 to 180 deg/sec) or at constant acceleration (1 deg/sec^2).   The latency of onset was measured using a stopwatch from the sudden onset of optokinetic stimulation (lights on) to the beginning of circularvection. Following the stimulus onset, circularvection began after a latency of about 3 to 4 seconds. The latencies were found to be independent of the stimulus velocities tested.

Young and Oman [48] carried out experiments in one of the differential maneuvering simulators (DMS) at the NASA Langley Research Center. Each simulator consisted of a jet cockpit mounted on a fixed-base platform inside of a forty-foot diameter projection sphere. Visual scenes were projected on the interior of the sphere wall by a computer controlled projection system that consisted of two servo-driven transparent plastic hemispheres on which the scenes to be projected were painted. A high intensity point light source mounted near the center of each hemisphere projected the scene onto the interior walls of the simulator sphere. The hemispheres projected a pattern of randomly spaced and oriented black rectangles of 2 to 3 degrees in subtended angle against a white background, with a black-white ratio of approximately 25%. A series of constant velocity yaw stimuli were presented randomly left and right at speeds of 5 to 120 deg/sec. The latency of onset was recorded using a stopwatch. A rapid decrease in time to onset of circularvection with increasing pattern speed (from 11 seconds at 5 deg/sec to 6 to 2 seconds from 10 to 120 deg/sec) was observed.

Howard and Howard [46] performed tests using an apparatus consisting of a vertical cylinder of translucent plastic, with an inner surface covered with adhesive black vinyl and perforated with round holes randomly distributed over the surface. The cylinder was illuminated from outside by diffuse tungsten light. The visual field of the subject inside the cylinder was filled with a random array of white spots subtending approximately 0.5 and 1 degree respectively. The cylinder rotated from left to right, from the subject's point of view, about its mid-vertical axis. Six stimulus field conditions were tested at angular velocities of 5, 10, and 25 deg/sec. The field conditions consisted of a full field condition where subjects saw only a moving display without stationary objects, a set of conditions with two vertical rods placed symmetrically at central, intermediate, and peripheral locations in front of the moving display (each presented separately and all presented together), and a condition with a frame placed in front of the moving display similar to the "window bars" that frame the video monitors in a simulator cockpit. Each field condition at each velocity was tested once with the subject looking straight ahead with relaxed gaze, and once with the gaze fixated on a stationary white spot projected from a laser and positioned at eye level straight ahead of the subject. The latency of vection was measured by having the subject press a switch at the first sign of vection.

The results obtained by Howard and Howard [46] showed that latency is longer when there are no stationary objects in view. They note that this effect is most evident at the lowest stimulus velocity, where subjects were usually unaware that the display was moving. They reasoned that at this velocity the eyes reflexively pursue a moving display without the presence of stationary objects. Fixation upon a small laser point was also sufficient to increase the vection magnitude significantly. At 5 deg/sec, the presence of

the visual frame reduced latency for the full field condition from 48.4 seconds to 8 seconds with no fixation. With fixation, the presence of the visual frame reduced latency from 14.3 seconds to 5.4 seconds, with the latency relatively unchanged for this condition (5.2 sec) for 10 and 25 deg/sec. The condition of central vertical rods without fixation also yielded results within the ranges reported by Young and Oman [48]; a latency of 9.4 seconds was found for a stimulus of 5 deg/sec that decreased to 5.6 seconds for 25 deg/sec.

Berthoz, et al. [49] tested the latency to onset of forward linearvection. The experimental apparatus they used allowed the projection of a moving 35-mm film loop of randomly distributed images on a screen that was fixed on a mobile cart. The screen image was projected via two mirrors to produce two peripheral images parallel to the sagittal plane of the head. The subject, whose head position was fixed by a chin rest, could view the moving images through a black box with side windows that limited the visual field between 20 and 70 degrees away from the sagittal plane on each side. The sensation of self-motion experienced by the subject was measured by the method of magnitude estimation by adjusting a lever fixed to the cart that could rotate forward or backward starting from a zero position. Both the lever rotation and the image velocity were recorded with a potentiometer.

In the experiment, latencies of about 1 to 1.5 seconds were observed for velocities measured between 0.2 and 1 m/sec. This significant difference in latency between linearvection and circularvection may be related to the differences in response dynamics associated with the otolith and semicircular canals respectively.

5.3. Visual-Vestibular Interaction Models

Zacharias [52] reported that both psychophysical and neurophysiological studies support the theory that visual and vestibular cues are jointly processed to provide for a perceived sense of self-motion. The vestibular nucleus complex was identified as a possible interaction for the convergence of sensory inputs. Zacharias [52] then noted that experiments reported by Dichgans, et al. on the single unit recordings from the vestibular nuclei of goldfish indicated that the majority of cells respond to both vestibular and moving visual field inputs. When both visual and vestibular stimuli were presented in opposing directions consistent with rotation in the presence of a physically stationary visual surround, the afferent firing rate was characterized by the faster response and greater sensitivity of vestibular stimulation combined with the non-adapting behavior of visual stimulation. The result was a signal that accurately indicated the perceived angular velocity.

A study by Young, et al. was also reported by Zacharias [52] in which subjective velocity and acceleration were measured in response to combined yaw-axis rotational cues. The study showed that the subjective velocity response was biased in the direction of the induced circularvection, but not to the extent of a simple summation of circularvection and expected vestibular response. These studies indicated that a simple linear summation of the visual and vestibular cues failed to predict the response when both cues are simultaneously presented.

Visual motion cues dominate the perception of velocity and orientation in the steady state and at frequencies below 0.1 Hz [43]. At higher frequencies, the vestibular cues will tend to dominate. Confirming vestibular cues, in the direction opposite to the

visual field, can produce a rapid onset of the visual self-motion that is sustained by vision after the vestibular cues have been washed out. When visual and vestibular motion cues are in conflict, either due to the direction of motion or to a difference in magnitude, the vestibular cues will initially dominate. Young [43] suggested that when both inputs are presented to a subject simultaneously, he or she would combine or "mix" the two cues in a nonlinear manner, favoring the visual input for confirming cues and the vestibular input for conflicting cues.

Young [53] first proposed that visual and vestibular cues are independently processed to produce two estimates of motion that are compared with one another to provide some means of cue conflict. For low conflict, such as when the cues confirm one another, the perceived motion is calculated from the weighted sum of the two estimates. This weighting is dependent on the sensory cue characteristics in the given situation and would be chosen to minimize the error in the combined cue estimate. For high conflict, that is when the cues fail to confirm one another, the weighting is then shifted based upon the reliability of each cue.

Zacharias [52] developed a cue conflict model for yaw perception that was based on the switching concept first proposed by Young [53]. This model is illustrated in Figure 5.1. For low conflict, that is when the visual and vestibular cues are confirming, the perceived motion is calculated from a weighted sum of the two estimates. For high conflict, that is when the cues fail to confirm one another, the weighting on the visual input is reduced and that on the vestibular input is increased until the conflict is reduced.
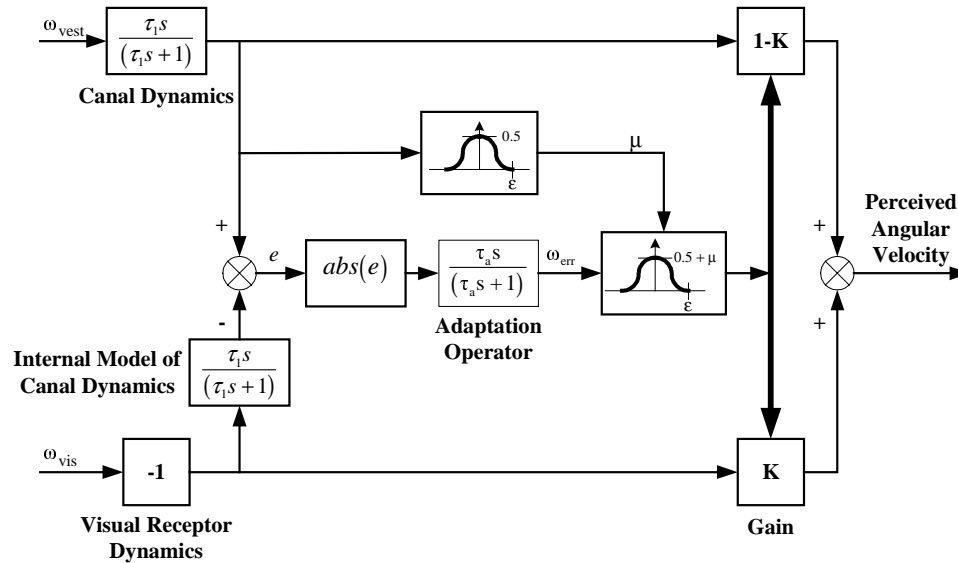
Figure 5.1. Visual-Vestibular Conflict Estimator Model. (Zacharias, [52])

The visual cue is passed through an internal model of the vestibular dynamics (a reduced model with only the long time constant was used) to produce an "expected" vestibular signal that is then subtracted from the actual vestibular signal. To allow for long-term resolution of steady-state conflict, the absolute value of this error is passed through an adaptation operator to generate the conflict signal. The adaptation operator determines how long a steady state conflict is allowed to continue by washing out the conflict signal, ultimately allowing for an averaging of the two cues. Zacharias [52] chose a value of 10 seconds for the adaptation time constant based on typical trainer acceleration latencies observed for a conflicting visual field.

The weighting of each cue is governed by a gain K that is derived directly from the two cues, and varies between zero and one. The gain K is computed from symmetric weighting functions that are applied to the vestibular and the washed out conflict signal ω_{err}. Zacharias [52] noted that "for simplicity" a cosine bell operator was chosen for the weighting function. A large conflict signal will drive the gain K to zero, gating out the

82

visual path, while a small conflict signal will drive K to a peak weighting value between 0.5 and 1, depending on the amplitude of the vestibular signal. In a low conflict situation the cues are either averaged or the visual cue is passed straight through and the vestibular cue is gated, depending on the magnitude of the vestibular cue. Zacharias [52] then noted that the value of the conflict threshold ε was determined by appealing to past work in defining threshold behavior. He presumed that the same type of behavior associated with the vestibular motion thresholds characterized cue conflict detection.

A second approach to modeling the visual-vestibular interaction was developed by Borah, et al. [54]. This approach involves the implementation of an optimal estimator as a "central processor" representation for the central nervous system processing of sensory inputs. Individual sensory dynamic models represent the visual and vestibular systems, and this concept can be extended to include proprioceptive and tactile models. The sensors respond to input stimuli and send signals to a central processor represented by a steady-state Kalman filter, which combines the sensory information to generate an estimate of the perceived motion. In this model, a modified version of the cue conflict estimator proposed by Zacharias [52] was also implemented.

Van der Steen [51] proposed a self-motion perception model in which vestibular and visual stimuli are combined to describe perceived self-motion. This model is shown in Figure 5.2. The model can describe perceived self-motion induced by either vestibular or visual stimuli alone, or a combination of both. However, unlike the model proposed by Zacharias [52], cue conflict estimation is not considered in this model.
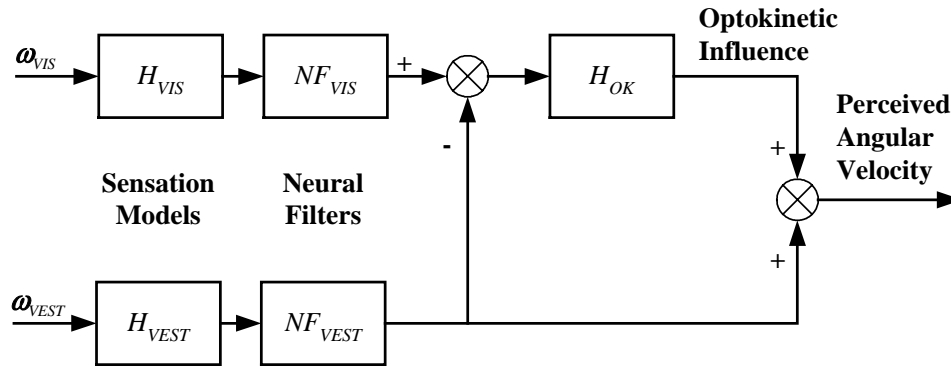
ω_{VIS} H_{VIS} NF_{VIS} +

Sensation Models **Neural Filters**

-

H_{OK}

Optokinetic Influence

Perceived Angular Velocity

+

+

ω_{VEST} H_{VEST} NF_{VEST}

Figure 5.2. Model for Self-Motion Perception with Visual Attractor. (Van der Steen, [51])

Van der Steen [51] introduced the concept of a neural filter in the model. The neural filter transfers the afferent response of either the visual or vestibular sensor to a perceptual physical variable. In other words, the neural filter models the process of assigning a perceptual meaning to a sensory output signal. Van der Steen then noted that, in general, neural filters are not explicitly described in the literature but are either represented as a constant that relates the afferent response to the perceived response, or are implicitly imbedded in the sensory dynamics. For example, the vestibular transfer function H_{VEST} cascaded with the vestibular neural filter NF_{VEST} represents the perceived self-motion estimate from vestibular stimuli.

Van der Steen [51] then noted that psychophysical experiments concerning vection showed that, depending on self-motion that the visual scene suggests, the visual estimate of self-motion "attracts" the vestibular estimate of self-motion. He suggested that the self-motion perception model needs a component that handles this "attraction" towards the visual system's estimate of self-motion. This component was referred to as the "visual attractor".

The visual attractor uses the visual and vestibular system's estimates of perceived self-motion. The difference between these cues is then filtered as shown in Figure 5.2, forming an optokinetic influence that is an estimate of perceived self-motion from visual stimuli. Van der Steen [51] noted that the filter H_{OK} represents the gradual build-up of perceived self-velocity when exposed to a constant visual scene velocity as observed in psychophysical experiments, and can be represented by a first-order low-pass filter of the form

$$H_{OK} = \frac{1}{1 + \tau_{OK} s}. \tag{5.1}$$

The perceived self-motion yielded by the model is then the sum of the optokinetic influence and the vestibular system's estimates of perceived self-motion.

Van der Steen [51] determined values for the optokinetic time constant τ_{OK} from experiments conducted using an optokinetic drum. The apparatus consisted of a rotating chair surrounded by a closed cylindrical drum, the inside of which contained alternating black and white stripes. Each test subject was asked to fixate on a stripe edge near the middle of the drum to indicate left or right drum motion. Two experiments were performed using this apparatus. In experiment 1, six visual acceleration amplitudes were tested with the chair stationary, and fourteen inertial acceleration amplitudes were provided with three constant magnitude drum accelerations. In experiment 2, the drum was accelerated for one second to a constant velocity of either 10 or 20 deg/sec, with the chair remaining stationary. After 17 seconds, the drum decelerated for three seconds. Four acceleration amplitudes were tested. In both experiments, the subject indicated perceived drum motion by pushing a button, with the elapsed time recorded electronically.

Van der Steen [51] then performed a series of simulations of the self-motion perception model with the data from both experiments. It was found that the model could be more accurately described with different optokinetic time constants for each experiment; the value for τ_{OK} was chosen smaller for experiment 1 (2 seconds) and larger for experiment 2 (10 seconds). A smaller time constant for smaller drum accelerations also resulted. Van der Steen concluded that the model dynamics using fixed parameters might not completely describe results for each combination of stimuli.

5.4. Visual Sensory Dynamics Models

Each visual-vestibular interaction model examined incorporates a model of the visual receptor dynamics that in turn produces a perceptual estimate of the visual scene motion. Zacharias [52] did not model visual sensory dynamics due to the lack of experimental data for single channel visual response, and assumed that the visual system has a relatively wide-band response. The negative sign in Figure 5.1 reflects the fact that the visual field motion is opposite in direction to the perceived self-motion, i.e., a visual field moving to the left induces self-motion of the subject to the right.

Borah, et al. [54] modeled the dynamics of the visual sensor as unity, noting that the eye detects the visual field motion almost immediately after a short neural transmission delay. Van der Steen [51] modeled the perceptual dynamics as a cascade of the visual receptor transfer function and neural filter with a unity gain and a delay τ_d:

$$NF_{VIS}H_{VIS} = -e^{s\tau_d}. \qquad (5.2)$$

Hosman and Van der Vaart [55] noted that τ_d is due to the delay of the visual receptors along with the delays due to both neural transmissions from the retina to the visual cortex and information processing during motion perception. From experiments in

roll rate perception with visual displays only, Hosman and Van der Vaart found values for τ_d to be about 90 msec for peripheral visual field stimulation and about 150 msec for central visual field stimulation.

5.5. Proposed Rotational Model

A revised visual-vestibular interaction model will now be constructed for rotational motion. This model can be used to estimate perceived motion for yaw, roll, and pitch stimuli. As suggested by Borah, et al. [54], the visual motion cues considered will be limited to peripheral visual scenes provided by a flight simulator with a wide visual scene field. These peripheral cues would be equivalent to the passage of stars or clouds in a wide field simulation. The cues do not include any elements in the structure of the scene such as landmarks, orientation cues, or a visual horizon.

A visual-vestibular interaction model for rotational motion is proposed and is shown in Figure 5.3. The proposed semicircular canals model given in Eq. (3.9) is used. The vestibular model combines the afferent dynamics model with the neural filter gain proposed by Van der Steen [51], resulting in a model with a perceived response to vestibular stimuli. Since the visual motion cues are assumed to be peripheral, the visual delay $\tau_d = 90$ msec obtained by Hosman and Van der Vaart [55] is chosen. The optokinetic influence proposed by Van der Steen [51] is also implemented.
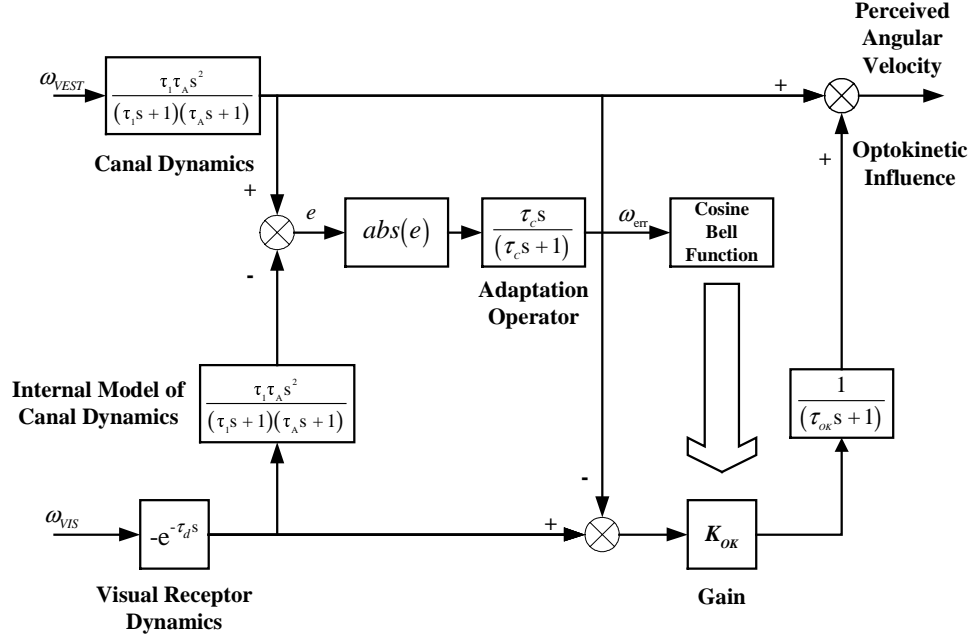
Figure 5.3. Proposed Visual-Vestibular Interaction Model for Rotational Motion.

As first proposed by Zacharias [52], the model produces a washed out conflict signal ω_{err}. The weighting of the optokinetic gain K_{OK} is then computed by a modified cosine bell function suggested by Borah, et al. [54] as shown in Figure 5.4. The gain K_{OK} varies between zero and one. A conflict signal greater than the threshold value ε ($\omega_{err} > \varepsilon$), will drive the optokinetic gain to zero, whereas a signal below the threshold value ($\omega_{err} < \varepsilon$) will drive the gain to a value between zero and one, approaching one as ω_{err} approaches zero. For $\omega_{err} < 0$, the gain remains at one. As previously suggested by Borah, et al. [54], the vestibular path gain remains fixed at unity.

The conflict threshold ε is chosen to equal the vestibular indifference motion threshold [52]. The angular velocity thresholds obtained by Benson, et al. [37], 1.6 deg/sec for yaw stimuli, and 2.0 deg/sec for roll and pitch stimuli, will be used in the model.
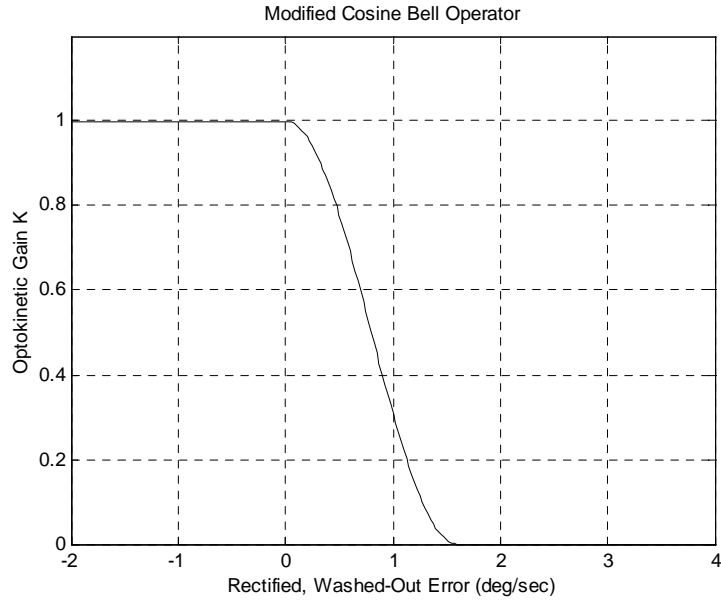
Figure 5.4. Modified Cosine Bell Operator for Optokinetic Gain.

In order to examine model responses to various stimuli, a MATLAB/SIMULINK representation of the proposed rotational model shown in Figure 5.3 was developed. Time constants $\tau_{OK} = 2$ seconds and $\tau_C = 5$ seconds were chosen to produce the latencies noted in the literature. In the model, the latency is defined as the amount of time to perceive motion above a visual indifference threshold of 3 deg/sec. Model responses to yaw inputs with either visual cues alone or confirming visual and vestibular cues were examined.

Figure 5.5 shows the responses to a visual field step input of 10 deg/sec. Since there is no vestibular input, the rectified error is the magnitude of the visual input filtered through the internal model of the semicircular canals. The adaptation operator then generates the washout error ω_{err}. Due to the large value of ω_{err}, the cosine bell function will produce a gain of zero for nearly five seconds. This results in a corresponding latency in the perceived angular velocity response.
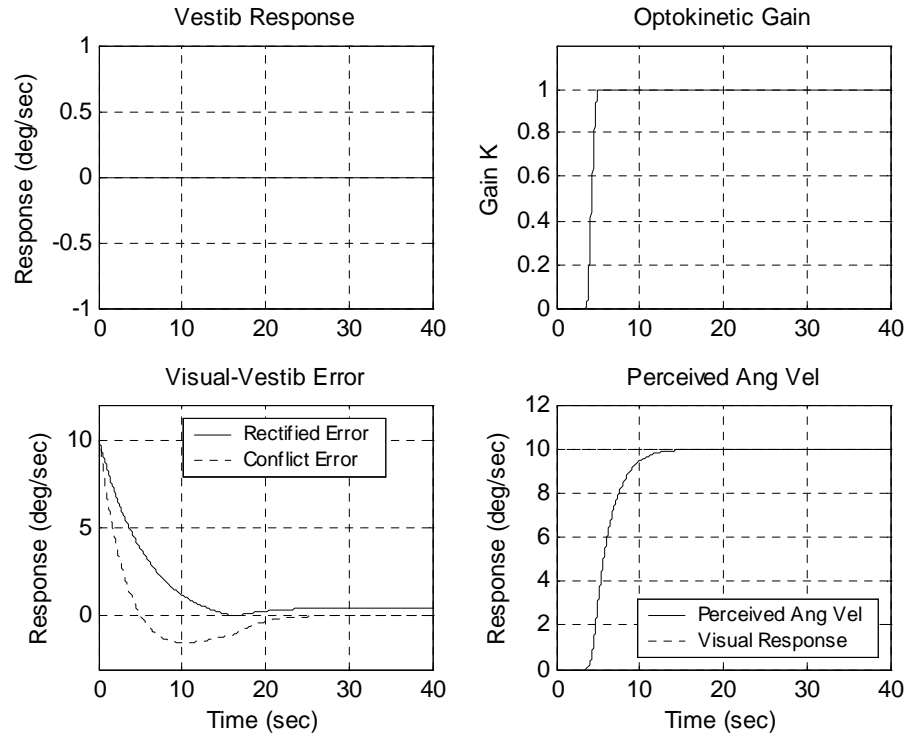
Figure 5.5. Rotational Perception Model Responses to Visual Step Input of 10 deg/sec.

Once ω_{err} decreases below the conflict threshold ε, the optokinetic gain will vary between zero and one, resulting in the onset of perceived motion or circularvection. This gain will rapidly rise to a value of one once ω_{err} reaches zero. As ω_{err} becomes negative, the gain K_{OK} remains at one. If a cosine bell operator were applied to this negative response, the gain would decrease back to zero, resulting in a large sag in the perceived response. The perceived motion reaches its maximum value with a rise time of about ten seconds, as governed by the time constant τ_{OK}.

Various magnitudes of angular velocity inputs were examined in order to compare latency responses with those obtained from psychophysical experiments in the literature. Figure 5.6 compares the model responses to visual step inputs of 5, 10, and 25 deg/sec.
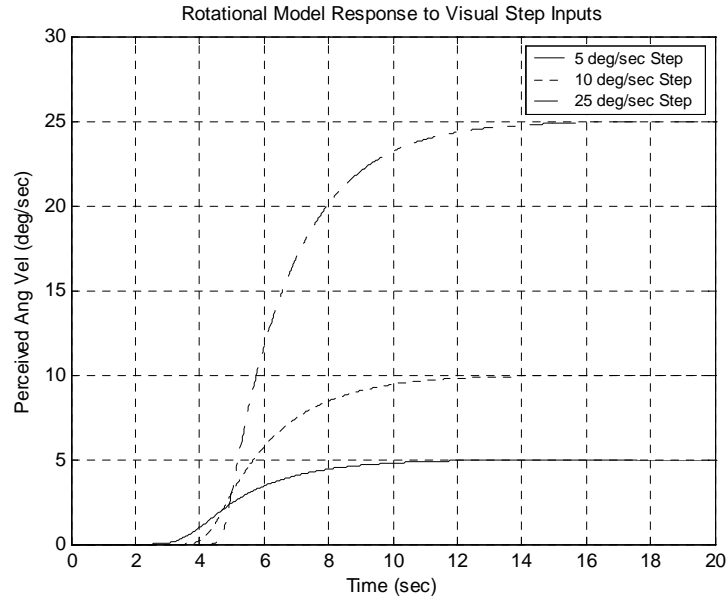
Rotational Model Response to Visual Step Inputs

Figure 5.6. Rotational Model Responses to Visual Step Inputs of 5, 10, and 25 deg/sec.

Due to the conflict estimator, the responses in Figure 5.6 produce a "dead zone", of which the duration increases with increasing step input. Assuming this phenomenon as latency alone contradicts the experimental results obtained by Howard and Howard [48] and Young and Oman [46] that showed the latency decreases with increasing stimuli magnitudes. However, assuming latency to onset occurs until an indifference threshold is reached reveals the latency decreasing with increasing step inputs.

The latencies resulting for the proposed rotational model are shown in Table 5.1. The latencies obtained with a threshold of 3 deg/sec result in values that are near those obtained by Howard and Howard [46] (5.2 to 5.4 seconds) for the stationary visual frame condition with fixation. As seen in Figure 5.6, increasing the visual threshold to 4 deg/sec for a 5 deg/sec step input would result in a latency of 7 seconds, which approaches the value of 8 seconds obtained by Howard and Howard [46] for the same condition with no fixation.

Table 5.1. Model Results for Latency to Onset of Circularvection.

ω_{vis} (deg/sec)	Latency (sec)	
	Model	Howard and Howard
5	5.525	5.4
10	5.0	5.2
25	5.0	5.2

Figure 5.7 shows the model responses to a confirming visual and vestibular step inputs of 10 deg/sec. Due to the visual delay τ_d, a large value of ω_{err} results at the onset that is rapidly washed out in a fraction of a second, resulting in the optokinetic gain K_{OK} increasing from zero to one during this instant and remaining at one for the duration of the response. Due to the rapid onset of the semicircular canals, the visual delay will have a negligible effect on the perceived response. After the vestibular cue decays, the optokinetic influence will gradually increase until the maximum response is achieved.
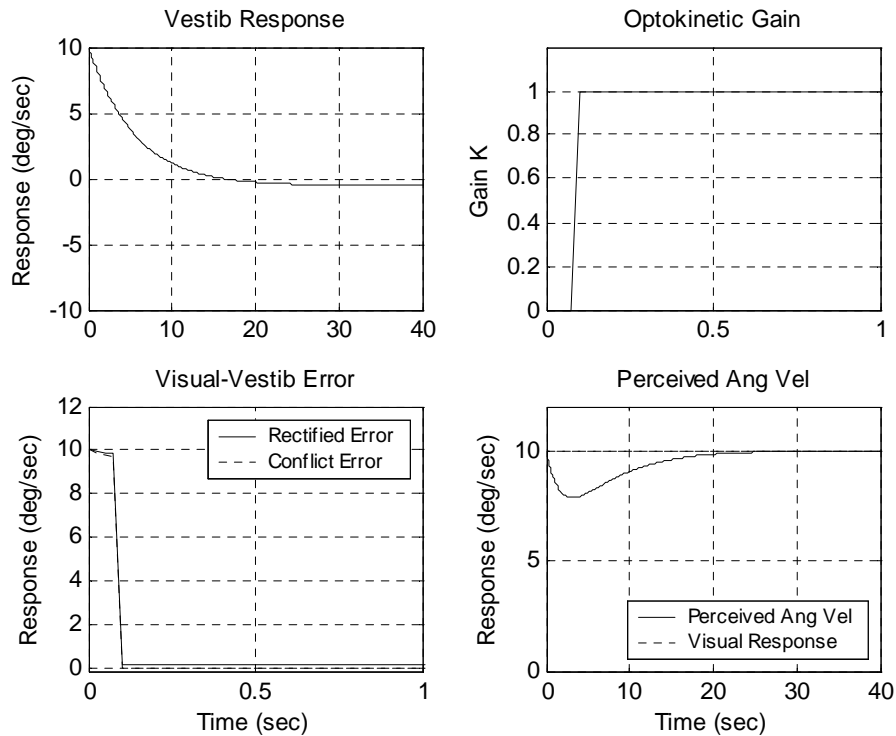

Figure 5.7. Rotational Perception Model Responses to Confirming Step Inputs of 10 deg/sec.

5.6. Proposed Translational Model

A visual-vestibular interaction model was developed to estimate motion in all three translational axes. The same assumptions applied to the rotational cues were considered. The proposed visual-vestibular motion model for translational motion is shown in Figure 5.8. The model structure is similar to the rotational model. The same values for visual delay τ_d and optokinetic time constant τ_{OK} as proposed for the rotational model will be used. In this model the washout error v_{err} is used to estimate the optokinetic gain K_{OK}. Vestibular and optokinetic responses are combined to produce perceived linear velocity.
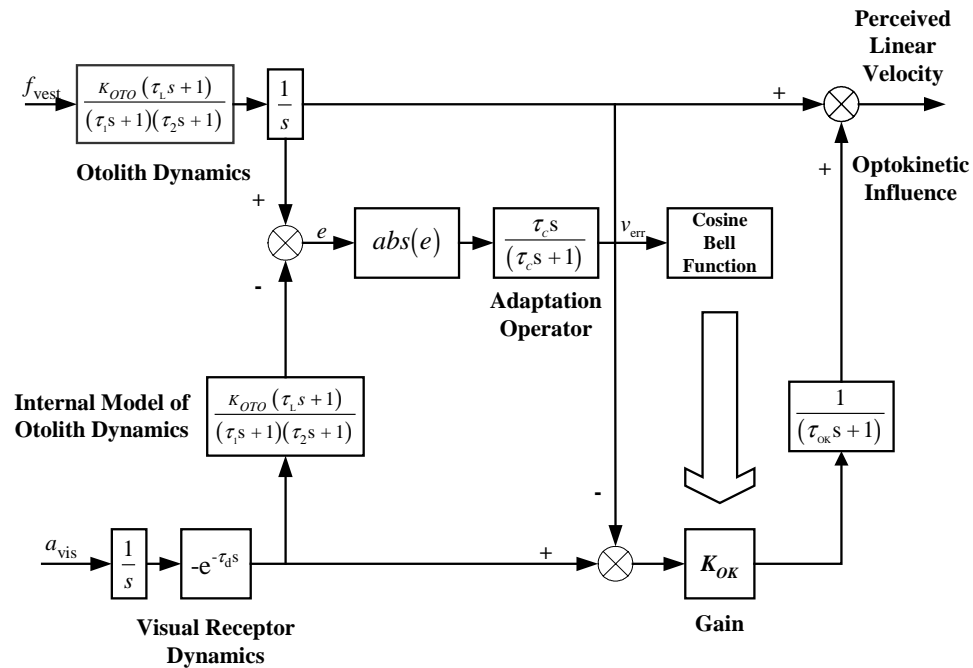

Figure 5.8. Proposed Visual-Vestibular Interaction Model for Translational Motion.

A MATLAB™/SIMULINK™ representation of the model shown in Figure 5.8 was developed. Figure 5.9 shows responses to a visual field step input of 1 m/sec. An adaptation time constant $\tau_C = 0.2$ seconds was chosen to generate latencies close to those

obtained by Berthoz, et al. [49]. The rectified error is the magnitude of the visual velocity response filtered through the internal model of the otoliths. As a result of this fast time constant, the washout error decays very quickly, resulting in a small latency of about 1.5 seconds. The perceived linear velocity then reaches its maximum value in about ten seconds, as governed by the time constant τ_{OK}.
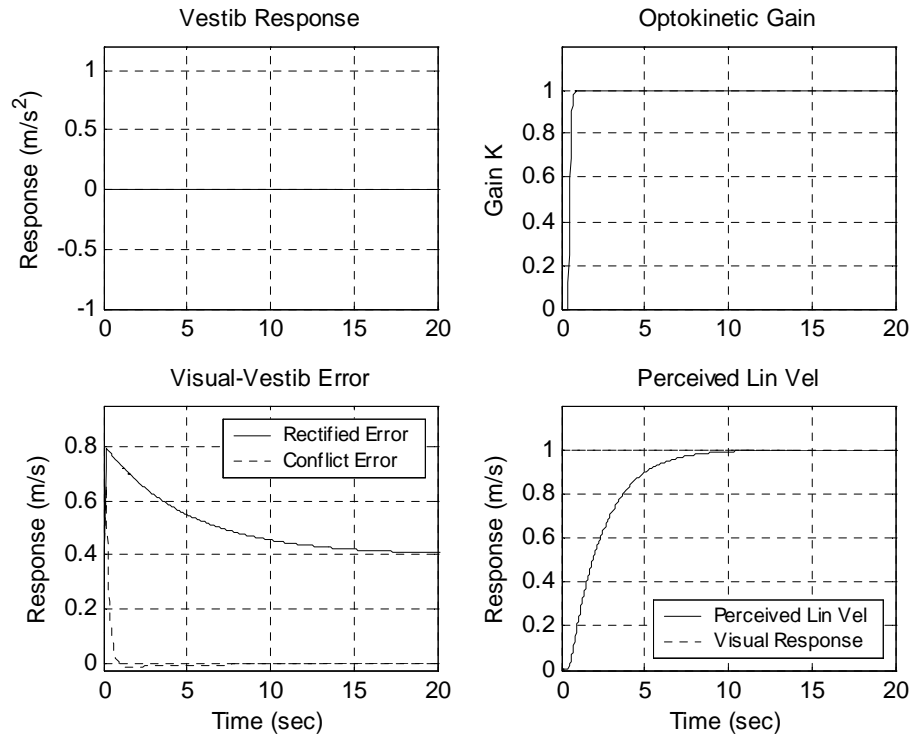
Figure 5.9. Translational Perception Model Responses to Visual Field Step Input of 1 m/sec.

Various magnitudes of linear velocity inputs were examined in order to compare latency responses with those obtained from psychophysical experiments in the literature. The latencies for $\tau_C = 0.2$ seconds and $\varepsilon = 0.2$ m/sec result in values that fall within the range (1 to 2 m/sec) reported by Berthoz, et al. [49] for velocity inputs from 0.4 m/sec to 1 m/sec. As the input is reduced towards the 0.2 m/sec threshold, the latency increases

beyond the reported experimental range. Table 5.2 lists the latencies the model generates

for inputs from 0.2 to 1 m/sec.

Table 5.2. Model Results for Latency to Onset of Linearvection.

v_{vis} (m/sec)	Latency (sec)
0.4	1.75
0.6	1.25
0.8	1.05
1.0	0.975

Figure 5.10 shows the model responses to confirming visual and vestibular step

pulse inputs of 1 m/s² magnitude and 1-second duration, which produces a ramp to step

velocity input of 1 m/s. Due to the visual delay τ_d, a sub-threshold value of ω_{err} is

generated at the onset that will result in the optokinetic gain K_{OK} being slightly less than

one for about one second.

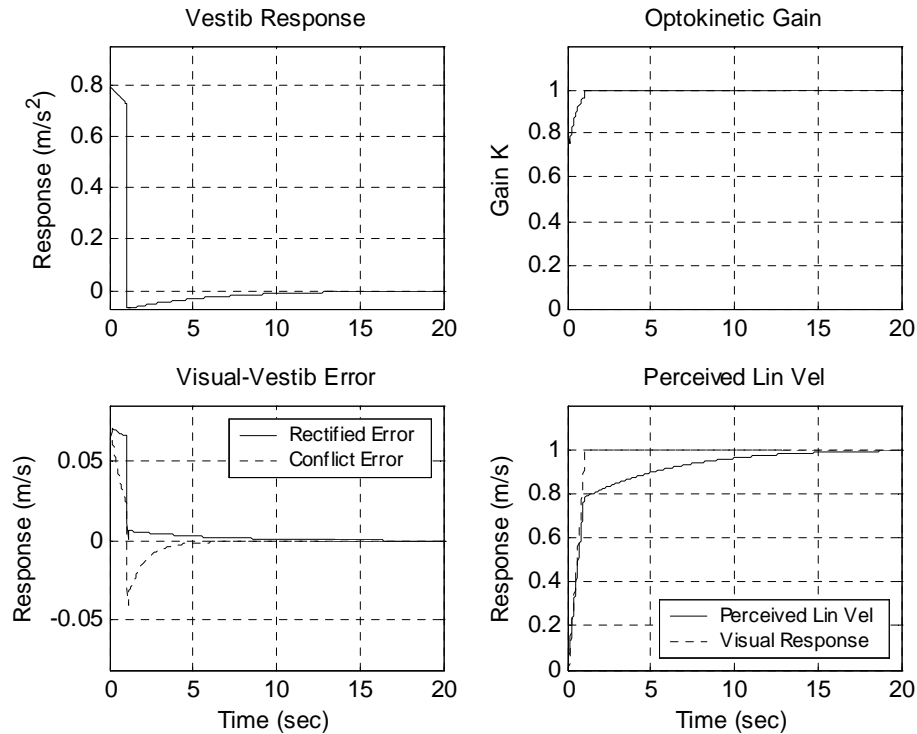**Figure 5.10. Translational Perception Model Responses to 100% Confirming Pulse Inputs of 1 m/sec Magnitude and 1 second Duration.**

Due to the rapid onset of the otoliths, the visual delay will have a negligible effect on the perceived response. After the initial otolith onset decays to its steady state value, the optokinetic influence then gradually increases until the maximum response is achieved.

6. Nonlinear Motion Cueing Algorithm

6.1. Problem Description

The motion perception process depends on the interaction between visual and vestibular sensation. Based on this, the problem is to develop a set of motion cueing filters that minimize the pilot perceptual error. A nonlinear approach is desired to further maximize the available motion cues within the hardware limitations of the motion system. This algorithm must be efficient enough to update filter characteristics in real time. Cardullo and Kosut [56] suggested this approach, and Ish-Shalom [57] also proposed a similar algorithm structure. The structure of the proposed solution is illustrated in Figure 6.1.

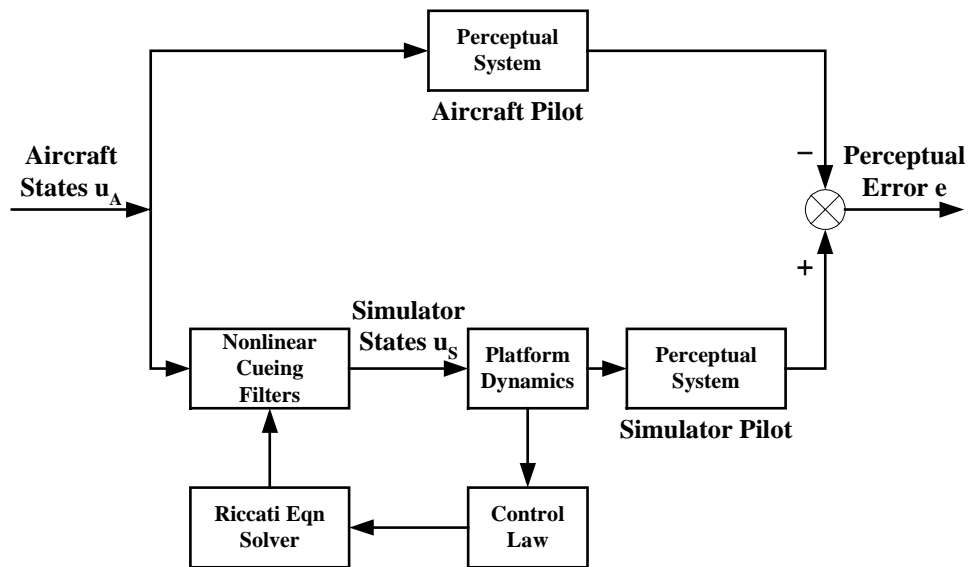**Figure 6.1. Proposed Solution for Nonlinear Motion Cueing Algorithm.**

The nonlinear algorithm incorporates models of the human vestibular sensation system, the new semicircular canals and otolith models, along with the new integrated visual-vestibular perception model. A nonlinear control law is implemented to generate a scalar coefficient α that is a function of the motion platform states. The matrix Riccati

97

equation is then solved in real time as a function of α, resulting in the feedback matrix needed to compute the desired motion cues. This results in nonlinear filter characteristics that sustain small motion cues for longer durations, and generates faster washout of large platform motions.

6.2. Algorithm Development

6.2.1. Longitudinal Mode

The algorithm development for the longitudinal (pitch/surge) mode is given below. The input **u** is the same as given in Eq. (4.1) for the linear algorithm development:

$$\mathbf{u} = \begin{bmatrix} \dot{\theta} \\ a_x \end{bmatrix} = \begin{bmatrix} u_1 \\ u_2 \end{bmatrix}, \tag{6.1}$$

where $\dot{\theta}$ is angular velocity, and a_x is the translational acceleration, with each term respectively set equal to u_1 and u_2. The reduced-order semicircular canals model given in Eq. (4.38) is used:

$$\hat{\dot{\theta}} = \frac{G_{SCC}s^2}{s^2 + T_1 s + T_0} u_1, \tag{6.2}$$

where T_0 and T_1 become

$$T_0 = \frac{1}{\tau_a \tau_1}, \ T_1 = \frac{\tau_a + \tau_1}{\tau_a \tau_1},$$

where τ_a and τ_1 are the same as those used in the optimal algorithm and given in the semicircular canals model of Eq. (3.8). G_{SCC} is the angular velocity threshold that scales the response to threshold units, using the threshold of 2.0 deg/sec obtained by Benson, et al. [37]. Eq. (6.2) is defined in state space notation as

$$\dot{\mathbf{x}}_{\text{scc}} = \mathbf{A}_{\text{scc}}\mathbf{x}_{\text{scc}} + \mathbf{B}_{\text{scc}}\mathbf{u}$$
$$\hat{\theta} = \mathbf{C}_{\text{scc}}\mathbf{x}_{\text{scc}} + \mathbf{D}_{\text{scc}}\mathbf{u},$$

(6.3)

where in observer canonical form,

$$\mathbf{A}_{\text{scc}} = \begin{bmatrix} -T_1 & 1 \\ -T_0 & 0 \end{bmatrix}, \ \mathbf{B}_{\text{scc}} = \begin{bmatrix} -G_{SCC}\tau_1 & 0 \\ -G_{SCC}\tau_0 & 0 \end{bmatrix}, \ \mathbf{C}_{\text{scc}} = \begin{bmatrix} 1 & 0 \end{bmatrix}, \ \text{and } \mathbf{D}_{\text{scc}} = \begin{bmatrix} G_{SCC} & 0 \end{bmatrix}.$$

In an attempt to produce the desired motion cues that most closely represent the perceptual behavior of the aircraft pilot, the confirming case of the integrated perceptual model (neglecting conflict estimation) will be incorporated into the perceptual channel. The visual delay was also neglected since it has only a small effect on the perceptual response.

For a simulator pilot, the perceptual input $\mathbf{u} = \mathbf{u}_S$ and for the aircraft pilot is $\mathbf{u} = \mathbf{u}_A$. Therefore, $\mathbf{u} = \mathbf{u}_S - \mathbf{u}_A$ can be considered as input to the cueing algorithm. For the perceptual error states $\mathbf{x}_e = \mathbf{x}_S - \mathbf{x}_A$, the input to the optokinetic influence of the integrated perception model given in Eq. (5.1) becomes

$$\hat{\theta}_e = \left(\dot{\theta}_A - \hat{\dot{\theta}}_S\right) - \left(\dot{\theta}_A - \hat{\dot{\theta}}_A\right) = \hat{\dot{\theta}}_A - \hat{\dot{\theta}}_S$$
$$= \left(x_{1A} + G_{SCC}u_{1A}\right) - \left(x_{1S} + G_{SCC}u_{1S}\right)$$
$$= G_{SCC}u_{1A} - x_1 - G_{SCC}u_{1S}.$$

(6.4)

The output of the optokinetic influence given in Eq. (5.1) (for gain $K_{OK} = 1$) becomes

$$\dot{\theta}_{OK} = \frac{1}{\tau_{OK}s + 1}\hat{\theta}_e = \frac{T_2\hat{\theta}_e}{s + T_2},$$

(6.5)

where $T_2 = 1/\tau_{OK}$. This can be defined as an additional state space term x_3:

$$\dot{x}_3 = -T_2 x_3 + T_2\dot{\theta}_{OK}$$
$$= -T_2 x_3 + T_2\left(G_{SCC}u_{A1} - x_1 - G_{SCC}u_{S1}\right)$$
$$= -T_2 x_1 - T_2 x_3 - G_{SCC}T_2 u_1.$$

(6.6)

99

Eq. (6.3) now becomes

$$\dot{\mathbf{x}}_{SCC} = \mathbf{A}_{SCC}\mathbf{x}_{SCC} + \mathbf{B}_{SCC}\mathbf{u}$$
$$\dot{\theta}_{PE} = \mathbf{C}_{SCC}\mathbf{x}_{SCC} + \mathbf{D}_{SCC}\mathbf{u}, \tag{6.7}$$

with

$$\mathbf{A}_{SCC} = \begin{bmatrix} -T_1 & 1 & 0 \\ -T_0 & 0 & 0 \\ -T_2 & 0 & -T_2 \end{bmatrix}, \quad \mathbf{B}_{SCC} = \begin{bmatrix} -G_{SCC}T_1 & 0 \\ -G_{SCC}T_0 & 0 \\ -G_{SCC}T_2 & 0 \end{bmatrix}, \quad \mathbf{C}_{SCC} = \begin{bmatrix} 1 & 0 & 1 \end{bmatrix}, \quad \mathbf{D}_{SCC} = \begin{bmatrix} G_{SCC} & 0 \end{bmatrix}.$$

The sensed velocity $\hat{v}_x$ is related to the stimulus specific force f_x by the otolith

model of Eq. (3.29):

$$\hat{v}_x(s) = G_{OTO}K'_{OTO}\frac{(s + A_0)}{s(s + B_0)}f_x(s), \tag{6.8}$$

where the break frequency B_1 is neglected, and G_{OTO} is the linear velocity threshold that

scales the response to threshold units. As with the linear algorithm, the specific force is

$$f_x = a_x + g\theta + R_{Sz}\ddot{\theta}. \tag{6.9}$$

In terms of u_1 and u_2, Eq. (6.9) is transformed into the Laplace domain, where

$$f_x(s) = u_2(s) + \left(g\frac{1}{s} - R_{Sz}s \right)u_1(s). \tag{6.10}$$

Note that the form of the transfer function of Eq. (6.8) is similar to the form of the otolith

model given in Eq. (4.5), with $\hat{v}$ replacing $\hat{f}$ as output, and the integrator replacing the

short time constant term $(s + B_1)$. Thus, Eq. (4.10) from the linear algorithm becomes

$$\ddot{\hat{v}}_x + B_0\dot{\hat{v}}_x =$$
$$G_{OTO}K'_{OTO}\left[R_{Sz}(B_0 - A_0)\dot{u}_1 + gu_1 + gA_0\int u_1 dt + \dot{u}_2 + A_0 u_2 \right], \tag{6.11}$$

and can be rewritten as $\ddot{\hat{v}}_x + a\dot{\hat{v}} = cu_1 + du_1 + e\int u_1 dt + fu_2 + gu_2$, and is then defined in

state space notation as

$$\dot{\mathbf{x}}_{\mathbf{OTO}} = \mathbf{A}_{\mathbf{OTO}}\mathbf{x}_{\mathbf{OTO}} + \mathbf{B}_{\mathbf{OTO}}\mathbf{u}$$
$$\hat{v}_x = \mathbf{C}_{\mathbf{OTO}}\mathbf{x}_{\mathbf{OTO}} + \mathbf{D}_{\mathbf{OTO}}\mathbf{u},$$

(6.12)

with

$$\mathbf{A}_{\mathbf{OTO}} = \begin{bmatrix} 0 & 1 & 0 & 0 & 0 \\ 0 & -a & 1 & 0 & 0 \\ 0 & 0 & 0 & 0 & 0 \\ 0 & 0 & 0 & 0 & 1 \\ 0 & 0 & 0 & 0 & -a \end{bmatrix}, \quad \mathbf{B}_{\mathbf{OTO}} = \begin{bmatrix} c & 0 \\ d-ac & 0 \\ e & 0 \\ 0 & f \\ 0 & h-af \end{bmatrix},$$

$$\mathbf{C}_{\mathbf{OTO}} = \begin{bmatrix} 1 & 0 & 0 & 1 & 0 \end{bmatrix}, \qquad \mathbf{D}_{\mathbf{OTO}} = \begin{bmatrix} -G_{OTO}r_{Sz} & 0 \end{bmatrix}.$$

The output of the optokinetic influence (for gain K_{OK} equal to 1) becomes

$$v_{xOK} = \frac{1}{\tau_{OK}s+1}\hat{v}_e = \frac{T_2\hat{v}_e}{s+T_2},$$

(6.13)

where $T_2 = 1/\tau_{OK}$. This can be defined as an additional state space term x_9:

$$\dot{x}_9 = -T_2 x_9 + T_2\left(-x_4 - x_7 + G_{OTO}K'_{OTO}r_z u_1\right)$$
$$= -T_2 x_4 - T_2 x_7 - T_2 x_9 + T_2 G_{OTO}K'_{OTO}r_z u_1.$$

(6.14)

Eq. (6.12) now becomes

$$\dot{\mathbf{x}}_{\mathbf{OTO}} = \mathbf{A}_{\mathbf{OTO}}\mathbf{x}_{\mathbf{OTO}} + \mathbf{B}_{\mathbf{OTO}}\mathbf{u}$$
$$v_{xPE} = \mathbf{C}_{\mathbf{OTO}}\mathbf{x}_{\mathbf{OTO}} + \mathbf{D}_{\mathbf{OTO}}\mathbf{u},$$

(6.15)

with

$$\mathbf{A}_{\mathbf{OTO}} = \begin{bmatrix} 0 & 1 & 0 & 0 & 0 & 0 \\ 0 & -a & 1 & 0 & 0 & 0 \\ 0 & 0 & 0 & 0 & 0 & 0 \\ 0 & 0 & 0 & 0 & 1 & 0 \\ 0 & 0 & 0 & 0 & -a & 0 \\ -T_2 & 0 & 0 & -T_2 & 0 & -T_2 \end{bmatrix}, \quad \mathbf{B}_{\mathbf{OTO}} = \begin{bmatrix} c & 0 \\ d-ac & 0 \\ e & 0 \\ 0 & f \\ 0 & h-af \\ T_2 G_{OTO}r_{Sz} & 0 \end{bmatrix},$$

$$\mathbf{C}_{\mathbf{OTO}} = \begin{bmatrix} 1 & 0 & 0 & 1 & 0 & 1 \end{bmatrix}, \qquad \mathbf{D}_{\mathbf{OTO}} = \begin{bmatrix} -G_{OTO}K'_{OTO}r_{Sz} & 0 \end{bmatrix}.$$

The representations in Eqs. (6.7) and (6.15) can be combined to form a single representation for the human perceptual model:

$$\dot{\mathbf{x}}_V = \mathbf{A}_V \mathbf{x}_V + \mathbf{B}_V \mathbf{u}$$
$$\mathbf{y}_{PE} = \mathbf{C}_V \mathbf{x}_V + \mathbf{D}_V \mathbf{u},$$

(6.16)

where $\mathbf{x}_V$ and $\mathbf{y}_{PE}$ are, respectively, the combined states and perceived responses, and $\mathbf{A}_V, \mathbf{B}_V, \mathbf{C}_V,$ and $\mathbf{D}_V$ represent the perceptual models as one set of state equations:

$$\mathbf{A}_V = \begin{bmatrix} \mathbf{A}_{SCC} & \mathbf{0} \\ \mathbf{0} & \mathbf{A}_{OTO} \end{bmatrix}, \quad \mathbf{B}_V = \begin{bmatrix} \mathbf{B}_{SCC} \\ \mathbf{B}_{OTO} \end{bmatrix}, \quad \mathbf{C}_V = \begin{bmatrix} \mathbf{C}_{SCC} & \mathbf{0} \\ \mathbf{0} & \mathbf{C}_{OTO} \end{bmatrix}, \quad \mathbf{D}_V = \begin{bmatrix} \mathbf{D}_{SCC} \\ \mathbf{D}_{OTO} \end{bmatrix}.$$

It is assumed that the same perceptual model can be applied to both the pilot in the aircraft and the pilot in the simulator as shown in Figure 6.1. We define the pilot perceptual error $\mathbf{e}$, resulting in

$$\dot{\mathbf{x}}_e = \mathbf{A}_V \mathbf{x}_e + \mathbf{B}_V \mathbf{u}_S - \mathbf{B}_V \mathbf{u}_A$$
$$\mathbf{e} = \mathbf{C}_V \mathbf{x}_e + \mathbf{D}_V \mathbf{u}_S - \mathbf{D}_V \mathbf{u}_A.$$

(6.17)

Additional motion platform states and filtered white noise states defined in the linear algorithm development in Eqs. (4.14) and (4.15) are again used. The desired system equation given in Eq. (4.16) is then formed, with the cost function J given in Eq. (4.17). The system equation and cost function are then transformed to the standard optimal control form given in Eq. (4.18). The cost function is augmented with an additional term $e^{2\alpha t}$ proposed by Anderson and Moore [58]:

$$J' = E\left\{ \int_{t_0}^{t_1} e^{2\alpha t} \left(\mathbf{x}^T \mathbf{R}_1' \mathbf{x} + \mathbf{u}'^T \mathbf{R}_2 \mathbf{u}' \right) dt \right\},$$

(6.18)

where $\mathbf{R}_1'$ is positive definite, $\mathbf{R}_2$ is positive semi-definite, and the scalar coefficient α represents a minimum degree of stability in the closed-loop system where $\alpha > 0$.

Anderson and Moore [58] showed that the system equation and cost function can be transformed to the standard optimal control form [39]:

$$\dot{\tilde{\mathbf{x}}} = \left(\mathbf{A}' + \alpha \mathbf{I} \right) \tilde{\mathbf{x}} + \mathbf{B}\tilde{\mathbf{u}} + \mathbf{H}'\mathbf{w}$$

$$\tilde{J}' = E\left\{ \int_{t_0}^{t_1} \left(\tilde{\mathbf{x}}^{\mathrm{T}} \mathbf{R}_1' \tilde{\mathbf{x}} + \tilde{\mathbf{u}}^{\mathrm{T}} \mathbf{R}_2 \tilde{\mathbf{u}} \right) dt \right\},$$

(6.19)

where $\tilde{\mathbf{x}} = e^{\alpha t}\mathbf{x}$ and $\tilde{\mathbf{u}} = e^{\alpha t}\mathbf{u}'$. We now wish to compute the simulator control input $\mathbf{u}_{\mathrm{S}}$ that minimizes the cost function given in Eq. (6.19). Anderson and Moore note that for this problem, $\mathbf{A}' + \alpha \mathbf{I}$ is positive definite, $\left(\mathbf{A}' + \alpha \mathbf{I}, \mathbf{B} \right)$ is controllable and $\left(\mathbf{A}' + \alpha \mathbf{I}, \mathbf{R}_1' \right)$ is observable. Under these conditions, the cost function is minimized when

$$\mathbf{u}_{\mathrm{S}} = -\mathbf{K}(\alpha)\mathbf{x},$$

(6.20)

where $\mathbf{K}(\alpha) = \mathbf{R}_2^{-1} \left(\mathbf{B}^{\mathrm{T}} \mathbf{P}(\alpha) + \mathbf{R}_{12} \right)$, and $\mathbf{P}(\alpha)$ is the solution of the algebraic Riccati equation

$$\left(\mathbf{A}' + \alpha \mathbf{I} \right)^{\mathrm{T}} \mathbf{P}(\alpha) + \mathbf{P}(\alpha)\left(\mathbf{A}' + \alpha \mathbf{I} \right) - \mathbf{P}(\alpha)\mathbf{B}\mathbf{R}_2^{-1}\mathbf{B}^{\mathrm{T}}\mathbf{P}(\alpha) + \mathbf{R}_1' = \mathbf{0}.$$

(6.21)

The feedback matrix $\mathbf{K}(\alpha)$ is partitioned corresponding to the partition of $\mathbf{x}$ in Eq. (4.16) of the linear algorithm development:

$$\mathbf{u}_{\mathrm{S}} = -\left[\mathbf{K}_1(\alpha) \quad \mathbf{K}_2(\alpha) \right] \begin{bmatrix} \mathbf{x}_{\mathrm{e}} \\ \mathbf{x}_{\mathrm{d}} \end{bmatrix} - \mathbf{K}_3(\alpha)\mathbf{u}_{\mathrm{A}},$$

(6.22)

and the Riccati equation solution $\mathbf{P}(\alpha)$ can be partitioned as

$$\mathbf{P}(\alpha) = \begin{bmatrix} \mathbf{P}_{11}(\alpha) & \mathbf{P}_{12}(\alpha) & \mathbf{P}_{13}(\alpha) \\ \mathbf{P}_{21}(\alpha) & \mathbf{P}_{22}(\alpha) & \mathbf{P}_{23}(\alpha) \\ \mathbf{P}_{31}(\alpha) & \mathbf{P}_{23}(\alpha) & \mathbf{P}_{33}(\alpha) \end{bmatrix},$$

(6.23)

where the partitions correspond to the partitions of the system matrix $\mathbf{A}$. Reid and Nahon [9] noted that when computing $\mathbf{K}$, only a subset of the elements of $\mathbf{P}$ is needed.

Substituting Eq. (6.23) and the expression for $\mathbf{R}_{12}$ from Eq. (4.18) into the expression for $\mathbf{K}$ given in Eq. (6.20) results in

$$
\begin{aligned}
\mathbf{K}_1(\alpha) &= \mathbf{R}_2^{-1}\left[\mathbf{B}_V^T\mathbf{P}_{11} + \mathbf{B}_d^T\mathbf{P}_{21} + \mathbf{D}_V^T\mathbf{Q}\mathbf{C}_V\right] \\
\mathbf{K}_2(\alpha) &= \mathbf{R}_2^{-1}\left[\mathbf{B}_V^T\mathbf{P}_{12} + \mathbf{B}_d^T\mathbf{P}_{22}\right] \\
\mathbf{K}_3(\alpha) &= \mathbf{R}_2^{-1}\left[\mathbf{B}_V^T\mathbf{P}_{13} + \mathbf{B}_d^T\mathbf{P}_{23} - \mathbf{D}_V^T\mathbf{Q}\mathbf{C}_V\right],
\end{aligned}
\tag{6.24}
$$

where, by symmetry, $\mathbf{P}_{12} = \mathbf{P}_{21}^T$.

Noting that $\mathbf{x_n} = \mathbf{u_A}$, remove the states corresponding to the $\mathbf{x_n}$ partition:

$$
\begin{bmatrix}\dot{\mathbf{x}}_e \\ \dot{\mathbf{x}}_d\end{bmatrix} = \begin{bmatrix} \mathbf{A}_V & \mathbf{0} & -\mathbf{B}_V \\ \mathbf{0} & \mathbf{A}_d & \mathbf{0}\end{bmatrix}\begin{bmatrix}\mathbf{x}_e \\ \mathbf{x}_d \\ \mathbf{u}_A\end{bmatrix} + \begin{bmatrix}\mathbf{B}_V \\ \mathbf{B}_d\end{bmatrix}\mathbf{u}_S,
\tag{6.25}
$$

and substituting Eq. (6.22) into Eq. (6.25) results in

$$
\begin{bmatrix}\dot{\mathbf{x}}_e \\ \dot{\mathbf{x}}_d\end{bmatrix} = \begin{bmatrix} \mathbf{A}_V - \mathbf{B}_V\mathbf{K}_1(\alpha) & -\mathbf{B}_V\mathbf{K}_2(\alpha) \\ -\mathbf{B}_d\mathbf{K}_1(\alpha) & \mathbf{A}_d - \mathbf{B}_d\mathbf{K}_2(\alpha)\end{bmatrix}\begin{bmatrix}\mathbf{x}_e \\ \mathbf{x}_d\end{bmatrix} + \begin{bmatrix}-\mathbf{B}_V\left(\mathbf{I}+\mathbf{K}_3(\alpha)\right) \\ -\mathbf{B}_d\mathbf{K}_3(\alpha)\end{bmatrix}\mathbf{u}_A.
\tag{6.26}
$$

A nonlinear control law is chosen to make α dependent upon the system states:

$$
\alpha = \mathbf{x}_d^T\mathbf{Q}_2\mathbf{x}_d,
\tag{6.27}
$$

where $\mathbf{Q}_2$ is a weighting matrix that is at least positive semi-definite. As the system states increase in magnitude, i.e. with large commanded platform displacements and velocities, then α increases, resulting in faster control action to quickly wash out the platform to its neutral state. For small commands there will be limited control action, resulting in motion cues being sustained for longer durations. The feedback matrix $\mathbf{K}(\alpha)$ is then determined by solving the Riccati equation of Eq. (6.19) in real time as a function of α.

The block diagram for the on-line nonlinear algorithm implementation is shown in   Figure 6.2. Due to the tilt coordination limit of 5 deg/sec that is needed for responses to surge inputs, a separate set of state equations as given in Eq. (6.26) and Riccati solver for Eq. (6.21) are needed for the pitch cues.
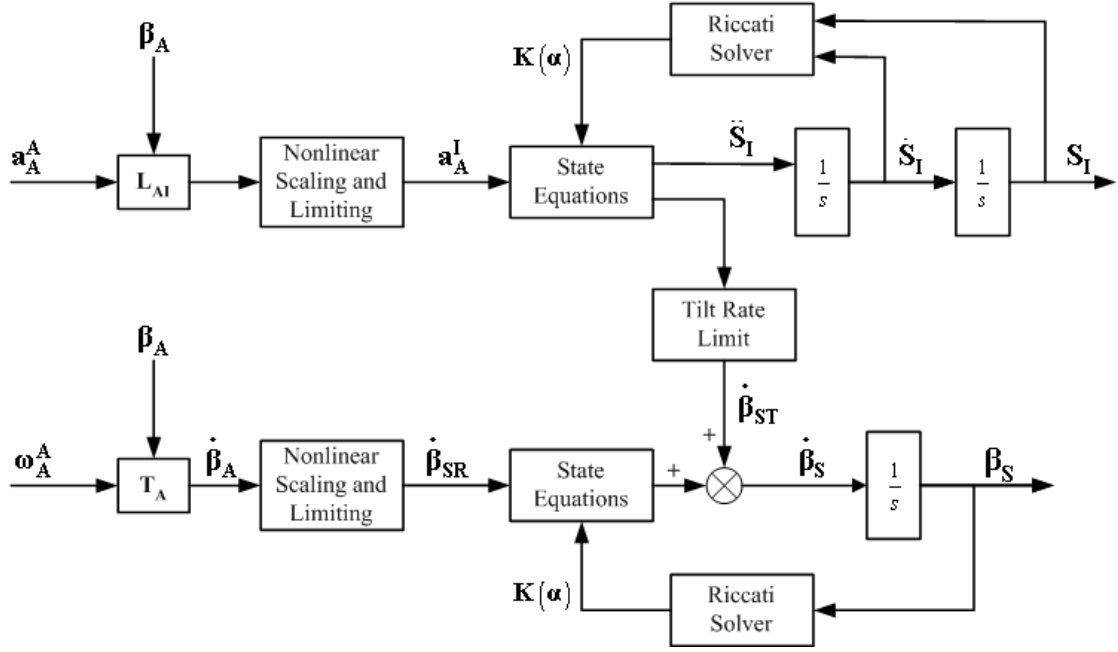

Figure 6.2. Nonlinear Algorithm Implementation for Longitudinal Mode.

6.2.2. Lateral Mode

For the lateral (roll/sway) mode, the algorithm development is analogous to the longitudinal mode. The inputs are the same as given in Section 4.2.2 for the linear algorithm. The specific force f_y is given in Eq. (4.26). With $\hat{v}_y$ replacing $\hat{v}_x$, the differential equation given in Eq. (6.8) becomes

$$\ddot{\hat{v}}_y + B_0 \dot{\hat{v}}_y =$$
$$G_O \left[R_{Sz} \left(A_0 - B_0 \right) \dot{u}_1 - g u_1 - g A_0 \int u_1 dt + \dot{u}_2 + A_0 u_2 \right], \tag{6.28}$$

which when rewritten as Eq. (6.11), will produce the state equation representation for the otolith   model   similar   to   Eq. (6.12),   with   the   same   system   matrices   except

$\mathbf{D_{OTO}} = \begin{bmatrix} G_{OTO}r_{Sz} & 0 \end{bmatrix}$. The state space representation for the vestibular model of the form

of Eq. (6.13) ultimately results. Similar to Eq. (6.14), the additional state resulting from

the optokinetic influence becomes

$$
\begin{aligned}
\dot{x}_9 &= -T_2 x_9 + T_2 \left(-x_4 - x_7 - G_{OTO}r_z u_1 \right) \\
&= -T_2 x_4 - T_2 x_7 - T_2 x_9 - T_2 G_{OTO}r_z u_1.
\end{aligned}
\tag{6.29}
$$

The perceptual model representation of the same form as Eqs. (6.16) and (6.17)

will then result. Additional motion platform states and filtered white noise states defined

in Section 4.2.2 are again used. The remaining development is identical in form to

Eqs.(6.18) to (6.27), resulting in state equations with a nonlinear control law and a time-

varying feedback matrix dependent upon solution of the Riccati equation. The on-line

implementation for this mode is identical to Figure 6.2.

6.2.3. Vertical Mode

For the vertical (heave) mode, the single degree-of-freedom input $u = a_z$, with the

specific force $f_z = a_z - g$. The otolith model given in Eq. (6.8) then becomes

$$
\hat{v}_z(s) = G_{OTO} K'_{OTO} \frac{(s + A_0)}{s(s + B_1)} f_z(s),
\tag{6.30}
$$

which can then be defined in state space notation as $\dot{\mathbf{x}}_{OTO} = \mathbf{A}_{OTO}\mathbf{x}_{OTO} + \mathbf{B}_{OTO}\mathbf{u}$, where

$\dot{\mathbf{x}}_{OTO}$ are the otolith states for this mode with $\dot{x}_2 = \hat{v}_z$, and

$$
\mathbf{A_{OTO}} = \begin{bmatrix} -B_0 & 0 \\ 1 & 0 \end{bmatrix}, \quad \mathbf{B_{OTO}} = \begin{bmatrix} G_{OTO}(A_O - B_O) \\ G_{OTO} \end{bmatrix}.
$$

Similar to Eq. (6.14), the additional state resulting from the optokinetic influence

becomes $\dot{x}_3 = -T_2 x_3 + T_2 u$. The state space perceptual model now becomes:

$$\dot{\mathbf{x}}_{\text{OTO}} = \mathbf{A}_{\text{OTO}}\mathbf{x}_{\text{OTO}} + \mathbf{B}_{\text{OTO}}\mathbf{u}$$
$$v_{zPE} = \mathbf{C}_{\text{OTO}}\mathbf{x}_{\text{OTO}},$$

(6.31)

with

$$\mathbf{A}_{\text{OTO}} = \begin{bmatrix} -B_0 & 0 & 0 \\ 1 & 0 & 0 \\ 0 & -T_2 & -T_2 \end{bmatrix}, \quad \mathbf{B}_{\text{OTO}} = \begin{bmatrix} G_{OTO}(A_O - B_O) \\ G_{OTO} \\ 0 \end{bmatrix}, \quad \mathbf{C}_{\text{OTO}} = \begin{bmatrix} 0 & 1 & 1 \end{bmatrix}.$$

Since this mode consists of a single translational degree-of-freedom, $\mathbf{A}_V = \mathbf{A}_{\text{OTO}}$, $\mathbf{B}_V = \mathbf{B}_{\text{OTO}}$, and $\mathbf{C}_V = \mathbf{C}_{\text{OTO}}$. This results in a perceptual model of the same form as Eq. (6.17). Additional motion platform states and filtered white noise states defined in the linear algorithm development in Eqs. (4.31) and (4.32) are again used. The remaining development is identical in form to Eqs. (6.18) to (6.27), resulting in state equations with a nonlinear control law and a time-varying feedback matrix dependent upon solution of the Riccati equation. The block diagram for the on-line implementation for this mode is shown in Figure 6.3.
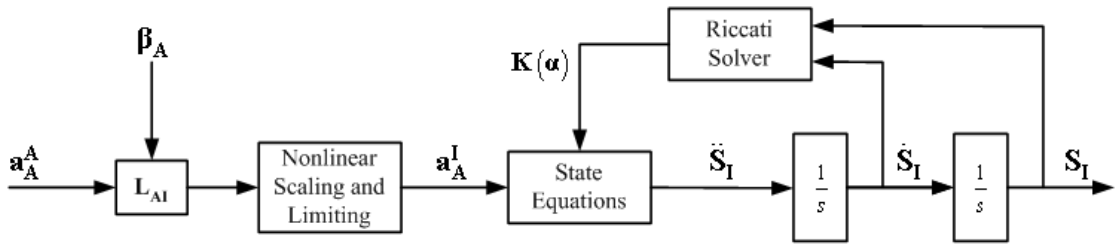

Figure 6.3. Nonlinear Algorithm Implementation for Vertical Mode.

6.2.4. Yaw Mode

For the yaw mode, the single degree-of-freedom input is $\mathbf{u} = \dot{\psi}$. The state equations given in Eq. (6.3) apply, with output $\hat{\psi}$ replacing $\hat{\theta}$. The additional state resulting from the optokinetic influence follows a development similar to Eqs. (6.4) to

(6.7), with $\dot{\psi}_{PE}$ replacing $\dot{\theta}_{PE}$ as output. Since this mode consists of a single rotational input, $\mathbf{A_V} = \mathbf{A_{SCC}}$, $\mathbf{B_V} = \mathbf{B_{SCC}}$, $\mathbf{C_V} = \mathbf{C_{SCC}}$, and $\mathbf{D_V} = \mathbf{D_{SCC}}$. This results in a perceptual model of the same form as Eq. (6.17). Additional motion platform states and filtered white noise states defined in the linear algorithm development in Eqs. (4.35) and (4.36) are again used. The remaining development is identical in form to Eqs. (6.18) to (6.27), resulting in state equations with a nonlinear control law and a time-varying feedback matrix dependent upon solution of the Riccati equation. The block diagram for the on-line implementation for this mode is shown in Figure 6.4.
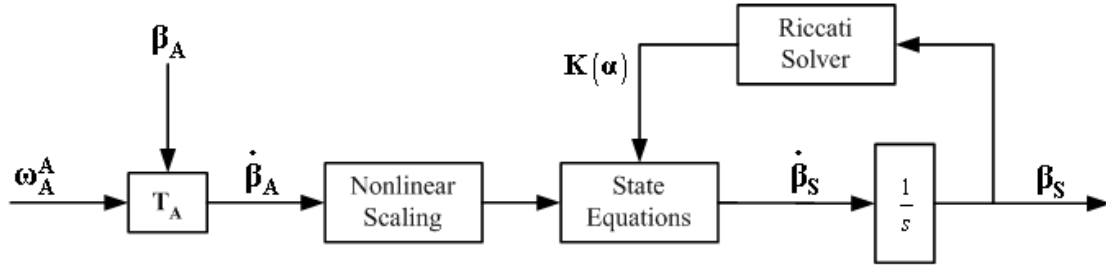

Figure 6.4. Nonlinear Algorithm Implementation for Yaw Mode.

6.3. Real Time Solution of the Riccati Equation

Solving the nonlinear Riccati equation in Eq. (6.21) is a computational challenge in real time as a new solution is required at each time step. Since the solution to the preceding time step is available, it is advantageous to use this as an initial solution when computing the solution for the current time step. This would result in a more refined computational solution that can be produced within the real time requirement, i.e., within a time step. The initial Riccati equation solution to the linear optimal algorithm that is computed off-line in MATLAB is available and can be used as the initial solution for the first time step. To this end we desire a technique that assumes the initial solution is "close" to the computational solution at a given time step. Two techniques were

investigated: a Newton-Raphson method and a neurocomputing approach using a structured neural network.

Blackburn [59] developed a method of solution using a Newton-Raphson iteration. The Riccati equation given in Eq. (6.21) is first generalized as

$$\mathbf{G}(\mathbf{P}) = \mathbf{PSP} - \mathbf{PA}'_\alpha - \mathbf{A}'^\mathbf{T}_\alpha \mathbf{P} - \mathbf{R}'_1, \tag{6.32}$$

where $\mathbf{A}'_\alpha = \mathbf{A}' + \boldsymbol{\alpha}\mathbf{I}$ and $\mathbf{S} = \mathbf{B}^\mathbf{T}\mathbf{R}_2^{-1}\mathbf{B}$. If we map the square matrices $\mathbf{G}$ and $\mathbf{P}$ into column vectors

$$\begin{aligned}\mathbf{g}(\mathbf{P}) &= vec(\mathbf{G}) = \begin{bmatrix} G_{11} & G_{21} & \cdots & G_{nn} \end{bmatrix} \\ \mathbf{p} &= vec(\mathbf{P}) = \begin{bmatrix} P_{11} & P_{21} & \cdots & P_{nn} \end{bmatrix},\end{aligned} \tag{6.33}$$

then it is shown that given an initial Riccati solution $\mathbf{p}(k)$, the Newton-Raphson method can then be used to obtain a refined solution

$$\mathbf{p}(k+1) = \mathbf{p}(k) - \left\{ \partial\mathbf{G}\big/\partial\mathbf{P}\big[\mathbf{p}(k)\big] \right\}^{-1} \mathbf{g}\big[\mathbf{p}(k)\big], \tag{6.34}$$

where $\partial\mathbf{G}\big/\partial\mathbf{P}$ is the Jacobian matrix, which is shown to be

$$\partial\mathbf{G}\big/\partial\mathbf{P} = -\left[\mathbf{I} \otimes \left(\mathbf{A}'_\alpha - \mathbf{SP}\right)^\mathbf{T} + \left(\mathbf{A}'_\alpha - \mathbf{SP}\right)^\mathbf{T} \otimes \mathbf{I} \right], \tag{6.35}$$

and $\otimes$ is the Kronecker product, where $\mathbf{A} \otimes \mathbf{B} = a_{ij}\mathbf{B}$.

Structured neural networks, first introduced by Wang and Mendel [60], are a special neural architecture that is customized to fit the specific matrix algebra application. An efficient method is employed that can take advantage of the matrix structure associated with the algorithm. Ham and Kostanic [61] have demonstrated this approach in solving a wide variety of matrix algebra problems such as matrix inversion, LU decomposition, and solving the algebraic matrix Lyapunov equation.

Ham and Collins [62] developed an approach for solving the algebraic matrix Riccati equation. A structured neural network is used for obtaining the computational solution $\mathbf{P}(t)$ and is shown in Figure 6.5.
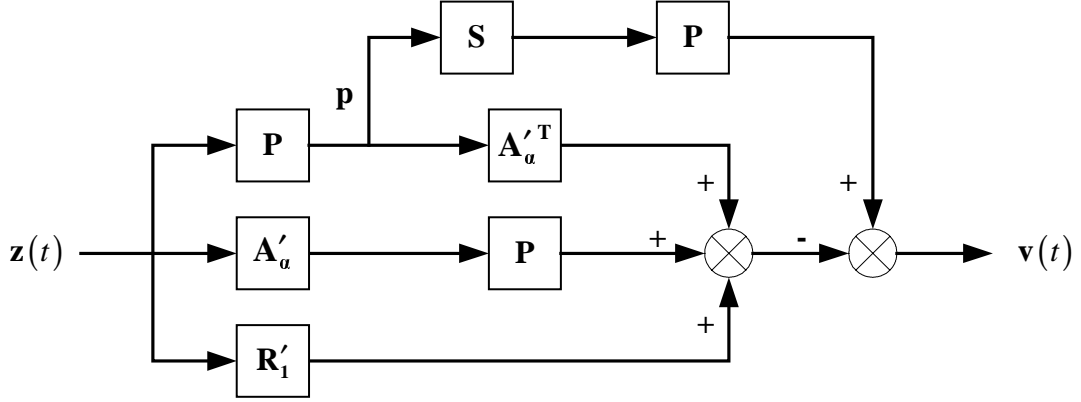

Figure 6.5. Structured Neural Network for Solving the Riccati Equation.

The error signal $\mathbf{v}(t)$ in Figure 6.5 is given as

$$\mathbf{v}(t) = \left[\mathbf{P}(t)\mathbf{S}\mathbf{P}(t) - \mathbf{A}_\alpha'^{\mathrm{T}}\mathbf{P}(t) - \mathbf{P}(t)\mathbf{A}_\alpha' - \mathbf{R}_1' \right]\mathbf{z}(t), \tag{6.36}$$

where $\mathbf{z}(t)$ is an excitatory input signal. An energy function is then formulated as $\mathbf{E}(\mathbf{P}) = \frac{1}{2}\|\mathbf{v}\|_2^2$ (where $\|\mathbf{v}\|_2$ is the Euclidean norm of $\mathbf{v}$), which is minimized using the method of steepest descent, resulting in a system of first-order matrix differential equations

$$\dot{\mathbf{P}}(t) = \mu\left[\mathbf{A}_\alpha'(t)\mathbf{v}(t)\mathbf{z}(t) + \mathbf{v}(t)\mathbf{z}^{\mathrm{T}}(t)\mathbf{A}_\alpha'(t) - \mathbf{v}(t)\mathbf{p}^{\mathrm{T}}(t)\mathbf{S} \right], \tag{6.37}$$

where $\mu > 0$ is the learning rate parameter, and $\mathbf{p}(t) = \mathbf{P}(t)\mathbf{z}(t)$ as shown in Figure 6.5. In discrete-time form (the time step Δt is absorbed into the learning rate μ), the learning rule for each training step k becomes

$$\mathbf{P}(k+1) = \mathbf{P}(k) + \mu\Delta\mathbf{P}(k), \tag{6.38}$$

110

with the update term $\Delta\mathbf{P}(k)$ given as

$$\Delta\mathbf{P}(k) = \left[\mathbf{A}'_{\alpha}(k)\mathbf{v}(k)\mathbf{z}(k) + \mathbf{v}(k)\mathbf{z}^{\mathbf{T}}(k)\mathbf{A}'_{\alpha}(k) - \mathbf{v}(k)\mathbf{p}^{\mathbf{T}}(k)\mathbf{S} \right]. \qquad (6.39)$$

Ham and Collins [62] noted that even though the update term is not symmetric, the learning rule would still converge to the positive definite, symmetric solution. They noted, however, that performing an additional computation resulting in a symmetric update term would improve convergence:

$$\mathbf{P}(k+1) = \mathbf{P}(k) + \frac{\mu}{2}\left[\Delta\mathbf{P}(k) + \Delta\mathbf{P}^{\mathbf{T}}(k) \right]. \qquad (6.40)$$

Ham and Collins [62] noted that the external excitatory vector input signals $\mathbf{z}(t)$ are a set of linearly independent bi-polar vectors given as

$$z^{(1)} = \begin{bmatrix} 1 & -1 & \cdots & -1 \end{bmatrix}, z^{(2)} = \begin{bmatrix} -1 & 1 & \cdots & -1 \end{bmatrix}, z^{(n)} = \begin{bmatrix} -1 & -1 & \cdots & 1 \end{bmatrix}, \qquad (6.41)$$

where each vector $z^{(k)}$ is presented once to the neural network in an iteration, i.e. for one iteration there is a total of n presentations of the training step given in Eq. (6.40), with the solution $\mathbf{P}(k)$ updated with each training step.

The structured neural network offers some advantages over the Newton-Raphson method for solutions to higher-order systems. The Newton-Raphson method requires matrix inversion, which resulted in singular solutions for ill-conditioned systems. Matrix inversion is not required for the structured neural network. Eliminating both matrix inversion and computation of the Jacobian matrix as a Kronecker product in turn reduces the computational burden. For these reasons the structured network approach is selected for implementation into the nonlinear algorithm.

6.4. Algorithm Evaluation

The nonlinear algorithm is developed to achieve the desired motion cues at an update rate of 60 Hz. Since the computer image generator, which provides the out-the-window visual imagery to the simulator pilot, also runs at 60 Hz, the motion cues would be synchronous with the visual cues. However, because of the computer operating system, the real time operating system and the I/O system on the Langley real time computing system, the minimum interval must be an integer multiple of 125 μsec and a power of 2. Therefore, a time step of 16 msec or an update rate of 62.5 Hz was selected for the real time implementation and the pilot tests.

For the vertical mode based upon the integrated perception model, the off-line solution of the Riccati equation initially produced one closed-loop eigenvalue of zero, which resulted in the linear optimal control weights being very difficult to tune, resulting in undesirable motion cues. This eigenvalue was a result of the inclusion of the optokinetic channel in the heave mode algorithm formulation given in Section 6.2.3; the formulation based on the vestibular model alone did not produce a zero eigenvalue. Kalman decomposition [41] was performed on the perceptual state space model of Eq. (6.31), resulting in a model with one less state, with no change to the perceptual response. Implementation of this reduced-order model removed the uncontrollable state and in turn eliminated the closed-loop eigenvalue of zero. The linear optimal control weights could then be tuned to produce the desired specific force cue; matrices $\mathbf{Q}$ and $\mathbf{R_d}$ were increased to produce the desired onset ramp and magnitude while the filtered white noise break frequency γ was increased to 20π rad/s to eliminate false cues.

In Figure 6.6, the vertical mode responses for a square pulse input from the nonlinear algorithm are compared to the linear algorithm based upon the integrated perception model. A learning rate parameter $\mu = 2 \times 10^{-7}$ is used in computing the Riccati equation solution. The nonlinear weight parameters $\mathbf{Q}_2 = diag(1.0, 2.0)$ result in the desired washout characteristics. The first diagonal term $\mathbf{Q}_2(1,1)$ acts upon the simulator displacement, reducing the z-axis displacement. The second term $\mathbf{Q}_2(2,2)$ acts upon the simulator velocity, reducing the offset response that follows the onset cue to an imperceptible magnitude.
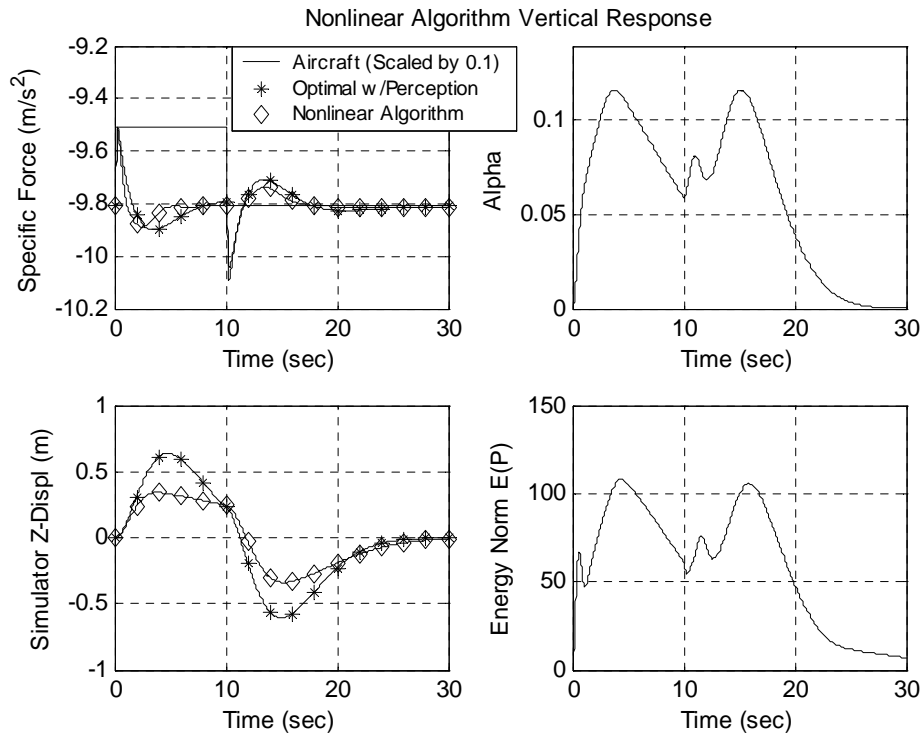

Figure 6.6. Nonlinear Algorithm Vertical Mode Responses.

A further increase of $\mathbf{Q}_2(1,1)$ does not reduce the displacement, but reduces the negative cue at the end of the pulse. An additional increase of $\mathbf{Q}_2(2,2)$ decreases the offset, but the magnitude of the negative cue remains unchanged. Figure 6.6 also shows

the nonlinearity α and the energy norm $\mathbf{E(P)}$ for the heave response. The variations resulting for α will in turn affect the vertical response. The energy norm reaches peak values at the start and end of the pulse, and approaches zero as the response is washed out and the platform returns to a neutral position.

The yaw mode responses for an angular acceleration pulse doublet are shown in Figure 6.7. Since all closed-loop eigenvalues were nonzero, Kalman decomposition of the perceptual model was not required. The weight $\mathbf{R_d}$ that acts upon the simulator yaw displacement was reduced to 200 to produce a faster onset cue. The nonlinear weight parameter $\mathbf{Q_2} = 120$ reduces the false cue at the end of the pulse.
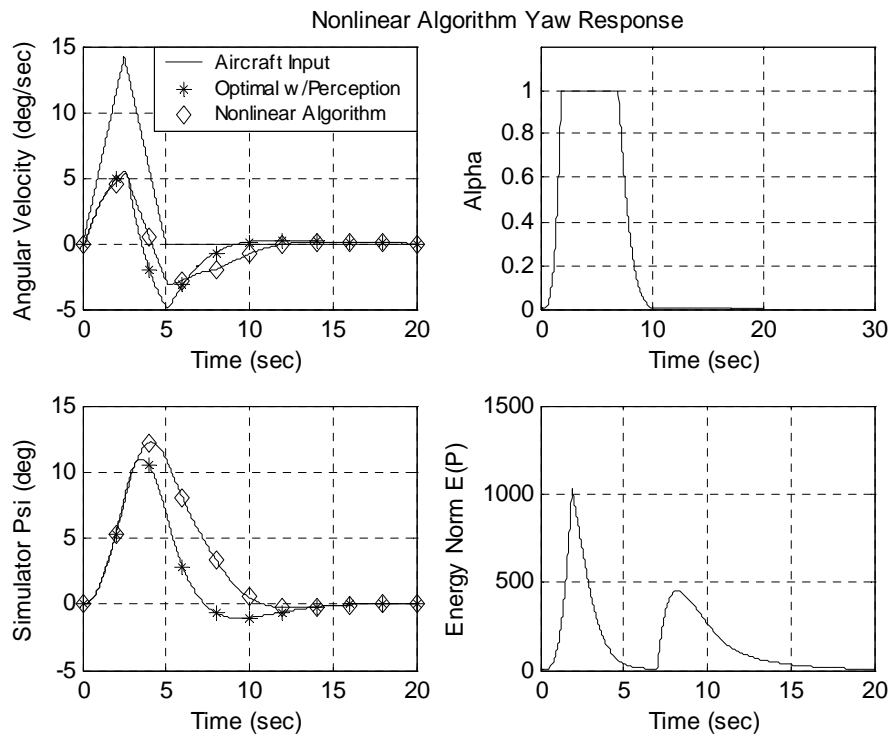

Figure 6.7. Nonlinear Algorithm Yaw Mode Responses.

In this mode an upper limit α_{max} equal to 1 is placed on α that restricts the yaw displacement. Increasing α_{max} will result in a longer sustained cue, but with an increase

in the yaw displacement beyond 12 degrees. Note that after α_{max} is reached, the energy norm **E(P)** rapidly decreases, increasing again when α starts to decrease below its upper limit. A learning rate parameter $\mu = 2 \times 10^{-6}$ is used in computing the Riccati equation solution; increasing μ by one order-of-magnitude results in a discontinuity in the angular velocity cue when α_{max} is reached.

For the two-degree-of-freedom longitudinal mode, the initial formulation with the integrated perception model resulted in a higher-order system (15th-order) that is much larger than either heave (6th-order) or yaw (5th-order). Two closed-loop eigenvalues of zero resulted from the off-line solution of the Riccati equation. The first originated from the additional simulator state θ. The second resulted from the optokinetic channel for the translational degree-of-freedom. Removal of the additional platform state combined with Kalman decomposition of the perceptual model given in Eq. (6.7) eliminates the two closed-loop eigenvalues of zero, reducing the system to 11th-order.

The longitudinal mode responses for a surge ramp to step input of 1 m/s^2 magnitude and 3 m/s^2/s slope are shown in Figure 6.8. Note that the nonlinear algorithm produces a specific force cue very close to the linear case, but with a reduction in the x-axis displacement. The percent reduction in displacement compared to the linear case increases as a function of the aircraft surge input magnitude. The peak angular velocity is slightly larger than the linear case, resulting in a slight increase of the pitch angle. The responses for both α and the energy norm (not shown) are similar to the heave and yaw modes in that the nonlinearity primarily affects the cue onset, with the energy norm washing out to zero over time.
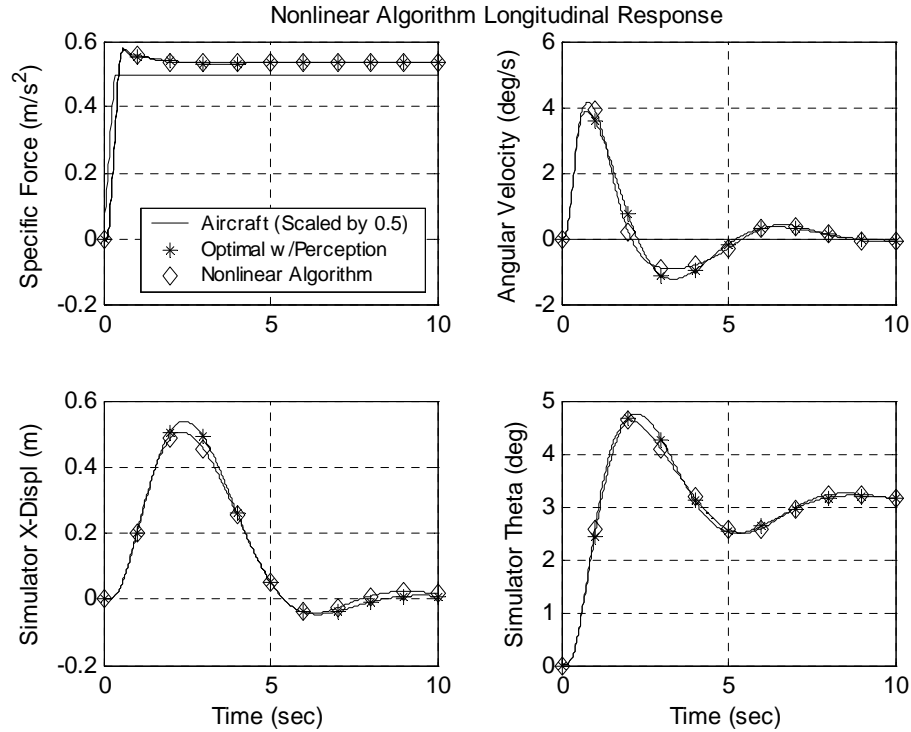
Figure 6.8. Nonlinear Algorithm Longitudinal Mode Responses to Surge Input.

The nonlinear weight parameters $\mathbf{Q_2} = diag(0,0.6)$ result in the desired washout characteristics. Increasing the first diagonal term $\mathbf{Q_2}(1,1)$ that acts upon the x-axis simulator displacement from 0 to 0.1 will result in increasing magnitudes of x-axis displacement and tilt with additional oscillatory responses. A further increase of the second diagonal term $\mathbf{Q_2}(2,2)$ results in an increase of the peak angular velocity. A learning rate parameter $\mu = 2 \times 10^{-6}$ is used in computing the solution of the Riccati equation; the responses are unchanged with an increase of μ by one order-of-magnitude.

Figure 6.9 shows the algorithm lateral mode responses to an aircraft half-sine input of 3 m/s^2 peak and 5-second duration. As with the longitudinal mode, Kalman decomposition was performed on the integrated perception model to eliminate one zero eigenvalue, and the additional simulator state ϕ was removed from the algorithm

formulation. As with the surge response, the nonlinear algorithm produces a specific force cue very close to the linear case, but with a 0.1-m reduction in the y-axis displacement. Similar to the longitudinal mode, the peak angular velocity is slightly larger than the linear case, but in this case the peak roll angle is slightly smaller.
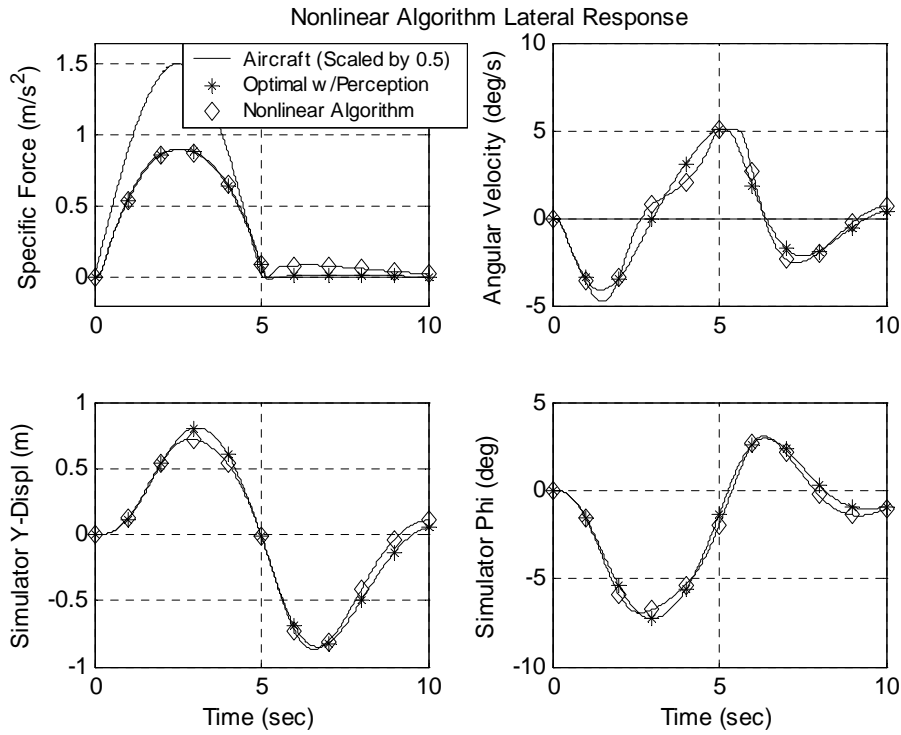

Figure 6.9. Nonlinear Algorithm Lateral Mode Responses to Sway Input.

A learning rate parameter $\mu = 2 \times 10^{-6}$ was again used; again the responses are unchanged with an increase of μ by one order-of-magnitude. The nonlinear weight parameters $\mathbf{Q}_2 = \text{diag}(0, 0.8)$ produce the desired washout characteristics. The effects of increasing the weights are the same as with the longitudinal mode.

The responses for a pitch doublet input of 0.1 rad/sec^2 are shown in Figure 6.10. A learning rate parameter $\mu = 2 \times 10^{-6}$ is used in computing the solution of the Riccati equation. The nonlinear weight parameter $\mathbf{Q}_2 = 1$ results in a large value for α, but does

not produce any noticeable change in the angular velocity response. Note that the response is scaled (by the pitch degree-of-freedom nonlinear gain), but closely follows the shape of the aircraft input.
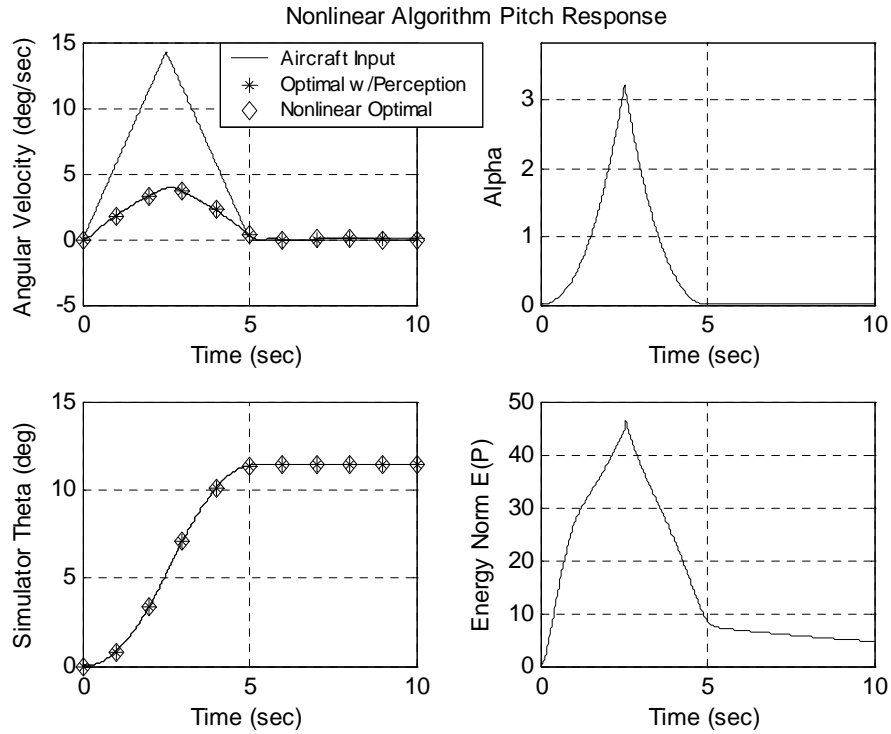

Figure 6.10. Nonlinear Algorithm Pitch Degree-of-Freedom Responses.

The frequency characteristics of the linear state space filter are very close to a unity-gain filter. Since there is no benefit from solving the Riccati equation in real time, the formulations shown in Eqs. (6.1) to (6.23) are replaced by unity-gain filters for both the pitch and roll degree-of-freedom. Figure 6.11 shows the revised implementation for the longitudinal and lateral modes.
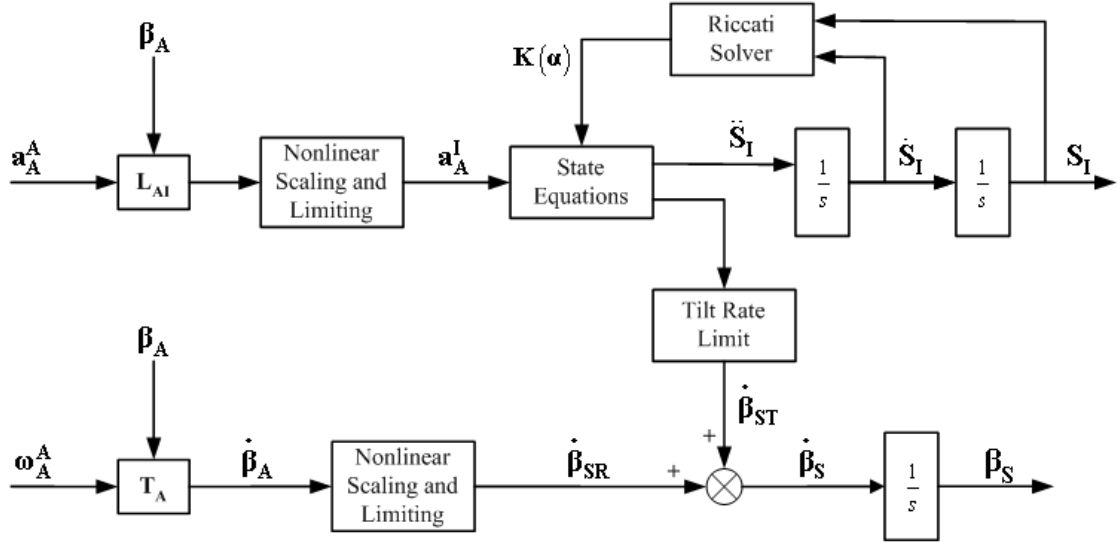
Figure 6.11. Revised Algorithm Implementation with Unity-Gain Pitch Filter.

The systems of first-order differential equations given for the neurocomputing solver in Eq. (6.40) require a numerical integration algorithm. A series of algorithms (Euler, 2nd-order Adams-Bashforth, 2nd- and 4th-order Runge-Kutta) were evaluated. No improvement was noticed with the higher-order methods as compared to the Euler method. However, for the system state equations in Eq. (6.26), the Euler method was found unstable for low sampling frequencies; the 2nd-order Runge-Kutta method resulted in stable results for sample rates as low as 32 Hz.

The responses using a second neurocomputing solver developed by Wang and Wu [63] are sensitive to the magnitude and stiffness of the closed-loop eigenvalues, with the responses dependent upon the choice and structure of the activation functions. The approach proposed by Ham and Collins [62] utilizes a structured network without activation functions; the responses are more robust with respect to the closed-loop eigenvalues.   This solver yields improved responses and convergence with less computational burden; only one solver iteration is required per time step.

119

During implementation on the NASA Langley real time computing system, it was discovered that for a time step of 16 msec, the real time requirement for the nonlinear algorithm was not being met. The baseline software for the nonlinear algorithm, with all presentations of the excitatory vector $\mathbf{z}(t)$ given in Eq. (6.41) for each mode, i.e. n presentations for an nth-order system, resulted in an average CPU time of 34 msec. This CPU time also includes the contributions of the aircraft model and control loader. Optimizing matrix operations by taking advantage of symmetry and sparse matrices in the state equations and solution of the Riccati equation resulted in an average CPU time of 24 msec. Reducing the number of presentations of the vector $\mathbf{z}(t)$ for each mode to the first three vectors produced a CPU time of 12 msec, which met the real time requirement.

This change is reflected in the nonlinear algorithm results shown in this Section. The results for the yaw mode were about the same as the case of 5 presentations of $\mathbf{z}(t)$. For the heave mode, the learning rate μ was reduced from 2×10^{-6} to 2×10^{-7} to remove a false cue at the end of the square pulse; the results were then very close to the case of 6 presentations of $\mathbf{z}(t)$. For the longitudinal and lateral modes the results were about the same as the case of 11 presentations of $\mathbf{z}(t)$ for each mode; the only noticeable change was an increase in a secondary artifact in the specific force cue after the half-sine pulse as shown in Figure 6.9 that remains imperceptible.

A summary of the nonlinear algorithm parameters for each of the four modes (longitudinal, lateral, vertical, and yaw) is given in Appendix C.

6.5. Pilot Tuning of the Algorithm

A computer program was developed by Telban, et al. [64] for the purpose of driving the NASA Langley Visual Motion Simulator (VMS) that is described in Section 2.1. This program includes both the optimal algorithm and the nonlinear algorithm. A general description of the program is given along with a description and flow charts of each cueing algorithm. Common block variable listings and a program listing are also provided. Procedures for tuning the nonlinear gain coefficients are also given.

In order to determine the nonlinear gain coefficients for each degree-of-freedom that resulted in the most desired pilot performance, an experienced simulator pilot executed a series of controlled maneuvers with the optimal and nonlinear algorithms on the VMS. This series of maneuvers was first executed with the polynomial gain coefficients determined prior to testing. Coefficients for each degree-of-freedom were then adjusted until the simulator pilot subjectively felt the desired perception and performance were reached, while ensuring that the simulator motion platform limits were not exceeded.

The following maneuvers were executed for both algorithms using the nonlinear B757 model:

> Straight Approach and Landing (with varying wind from head to tail)
> Offset Approach and Landing (with and without turbulence)
> Takeoff from Full Stop (with and without engine failure)
> Ground Maneuvers (taxiing, effect of aircraft brakes).

No additional tuning was needed for either the straight-in or offset approach maneuvers. However, both algorithms showed a tendency to exceed the actuator limits of the motion system with the takeoff maneuver. Reducing the surge gains for the optimal algorithm and both the surge and pitch gains for the nonlinear algorithm resulted

in platform motion within the actuator limits during the takeoff maneuvers. Table 6.1 lists the nonlinear gains by degree-of-freedom for each algorithm. From Eq. (2.8), the coefficients c_1, c_2, and c_3 are given for each degree-of-freedom.

Table 6.1. Nonlinear Gain Coefficients for the Cueing Algorithms.

Degree-of-Freedom	Optimal Algorithm			Nonlinear Algorithm		
	c_1	c_2	c_3	c_1	c_2	c_3
Surge (X)	0.6	-0.055	0.002	0.5	-0.05	0.002
Sway (Y)	0.5	-0.055	0.002	0.4	-0.035	0.001
Heave (Z)	0.6	-0.082	0.0038	0.6	-0.082	0.0038
Roll (p)	0.3	-0.3	0.1	0.3	-0.3	0.1
Pitch (q)	0.4	-0.54	0.26	0.3	-0.3	0.1
Yaw (r)	1.1	-1.46	0.64	1.1	-1.46	0.64

6.6. Comparison of Motion Cueing Algorithms

Algorithm responses using test runs for each degree-of-freedom are given in Appendix D. Comparisons are made (with the linear optimal algorithm) of both specific force cues (denoted by SF in the graphs) at the pilot's head and angular velocity cues, as well as the linear and angular displacement of the simulator. Actuator extension lengths are also compared. The number of each actuator referenced in Appendix D is shown on the motion platform in Figure 2.4.

The vertical mode responses for the nonlinear algorithm for a pulse input of 1 m/s^2 magnitude and 10-second duration are shown in Figure 6.12. The onset ramp is very close to that of the adaptive and optimal algorithms, with a slightly larger peak magnitude. The cue is sustained for a longer duration, resulting in 33 percent more z-axis displacement compared to the linear optimal algorithm. The negative specific force cue at the end of the pulse is twice the magnitude as the adaptive algorithm response. This results in increased sensation that indicates the end of the pulse input.
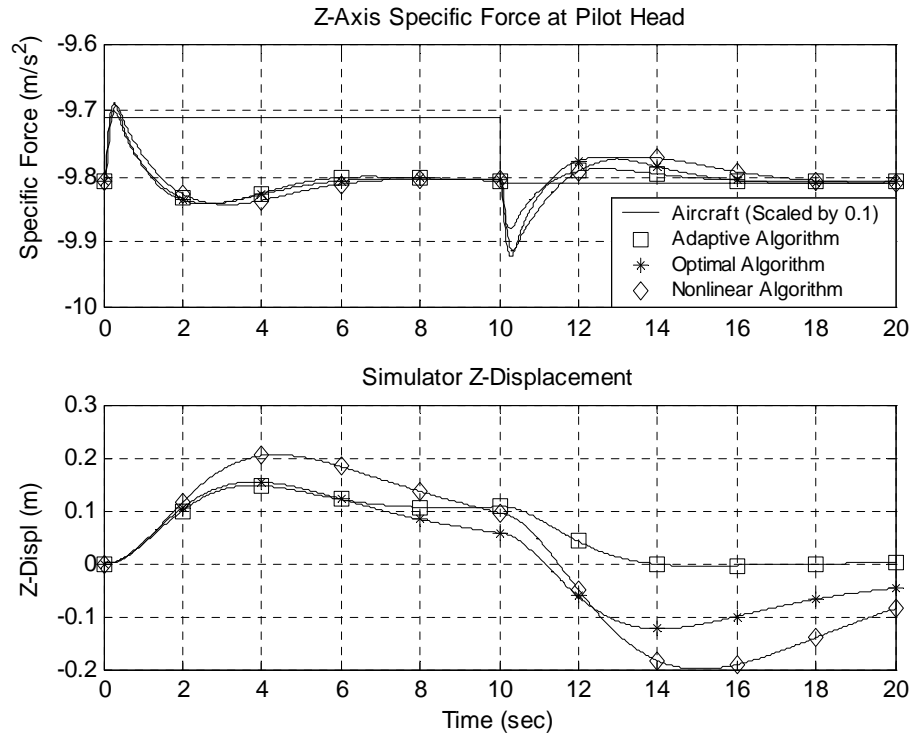
Figure 6.12. Algorithm Responses to Vertical Pulse of 1 m/s² Magnitude, 10-Second Duration.

Figure 6.13 compares responses with the vertical pulse magnitude increased to 3 m/s². The cue from the nonlinear algorithm is sustained for a longer duration, resulting in slightly less (5 percent less) z-axis displacement as compared to the linear optimal algorithm. The nonlinear algorithm response washes out faster due to the nonlinear effects generated from the Riccati equation solution. The negative cue at the end of the pulse is slightly smaller than the optimal algorithm response, but is much larger than the negative cue that results from the adaptive algorithm.
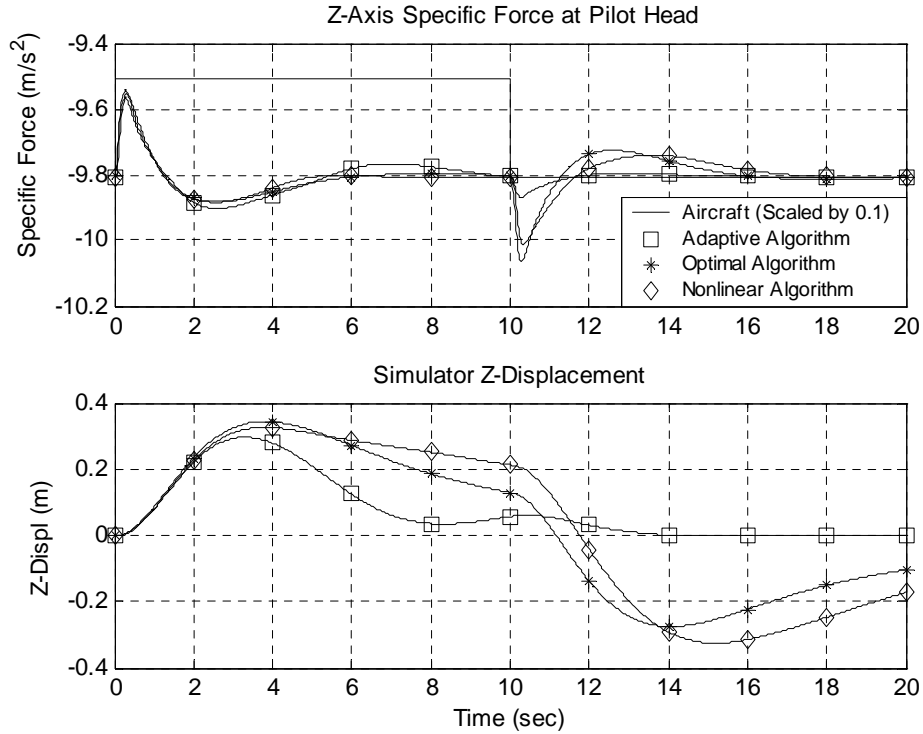
Figure 6.13. Algorithm Responses to Vertical Pulse of 3 m/s^2 Magnitude, 10-Second Duration.

Figure 6.14 compares the algorithm responses to an aircraft longitudinal input. A surge ramp to step input of 1 m/s^2 peak magnitude and 3 m/s^2/s slope is applied to each algorithm. The specific force response for the nonlinear algorithm does not wash out as a function of time, resulting from the steady-state tilt angle sustaining a constant magnitude. A small increase in the angular velocity (tilt) rate compared to the optimal algorithm is also observed. Note that the adaptive algorithm has a larger steady-state specific force magnitude, as well as a larger angular velocity.
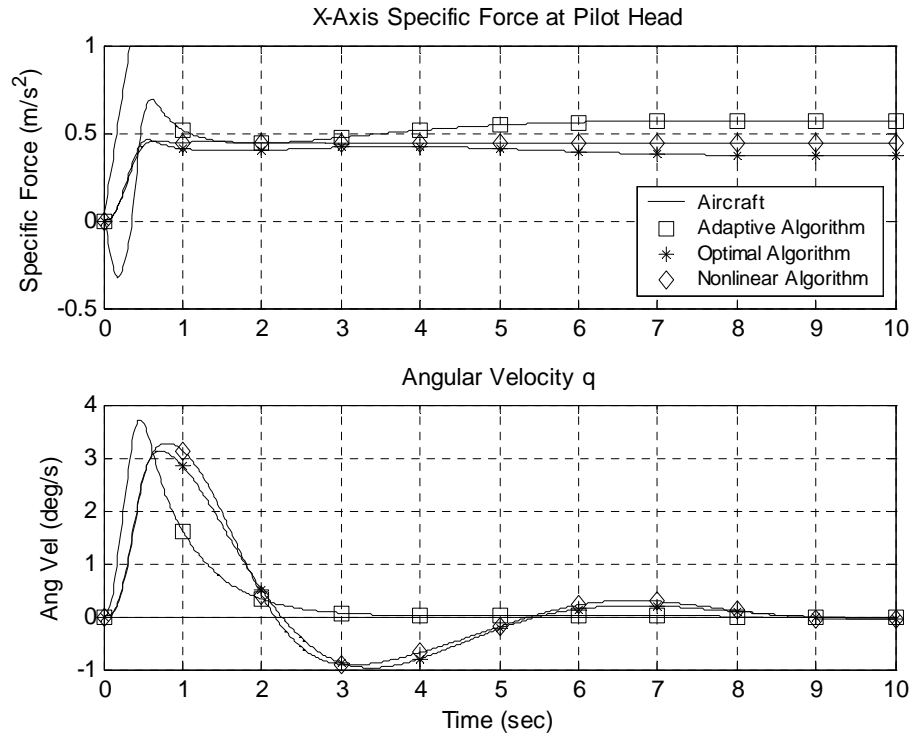
Figure 6.14. Algorithm Responses to Surge Ramp to Step of 1 m/s² Magnitude, 3 m/s²/s Slope.

Figure 6.15 compares the responses from the integrated perception model for these surge cues. The sensed specific force, or otolith responses show the nonlinear algorithm closely tracks the shape of the sensed response from the aircraft. The optimal algorithm produces about the same onset as the nonlinear algorithm, but results in noticeably less sensed response, especially for the first few seconds after the peak magnitude is reached. The perceived velocity responses show a slightly larger magnitude for the nonlinear algorithm, increasing to 2 percent greater magnitude after 10 seconds. The adaptive algorithm shows a negative, or false specific force cue sensed at the onset that results in a subsequent lag and a reduction in the perceived velocity for one second.
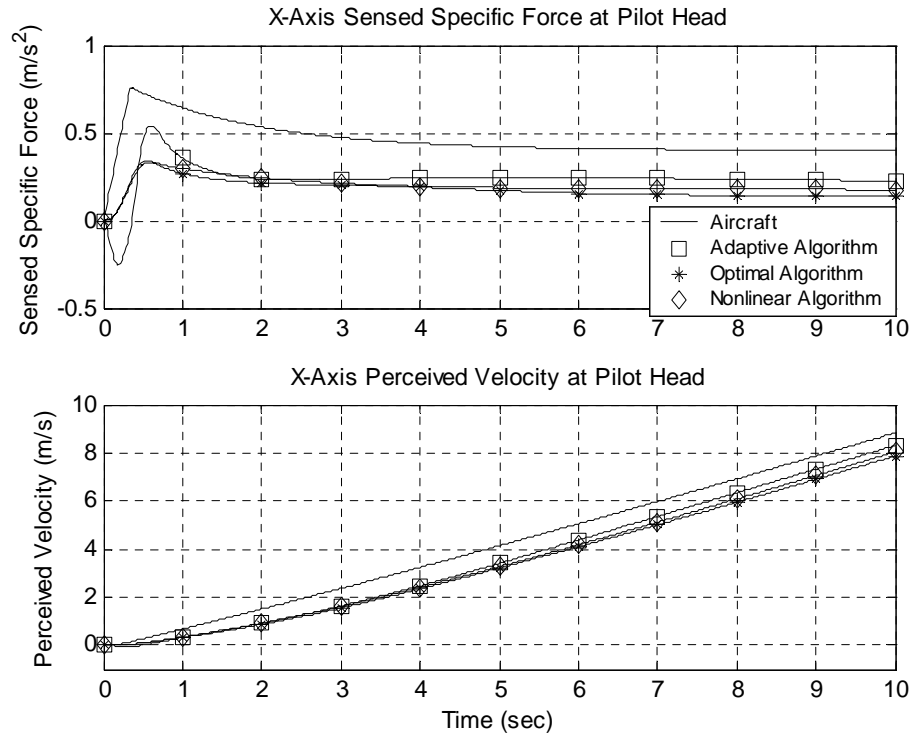
Figure 6.15. Integrated Perception Model Responses to Surge Cues of Figure 6.14.

Figure 6.16 compares the algorithm responses to an aircraft lateral input. A sway half sine of 3 m/s^2 peak magnitude and 5-second duration was applied to each algorithm. Note that the specific force cue generated by the adaptive algorithm has some significant distortion. A false cue is generated at onset, resulting in a noticeable lag in the motion cue response. A large peak magnitude is reached, but nearly one second after the aircraft input reached its peak. A large residual specific force cue remains for about three seconds after the aircraft input ends. The response generated by the linear optimal algorithm shows no negative cue at the onset, a well-shaped half sine response with a less noticeable lag, and much less residual specific force cue. The nonlinear algorithm results in a peak specific force cue that is 15 percent larger than the linear optimal algorithm, with even less lag and almost no residual specific force cue after the half sine input ends.
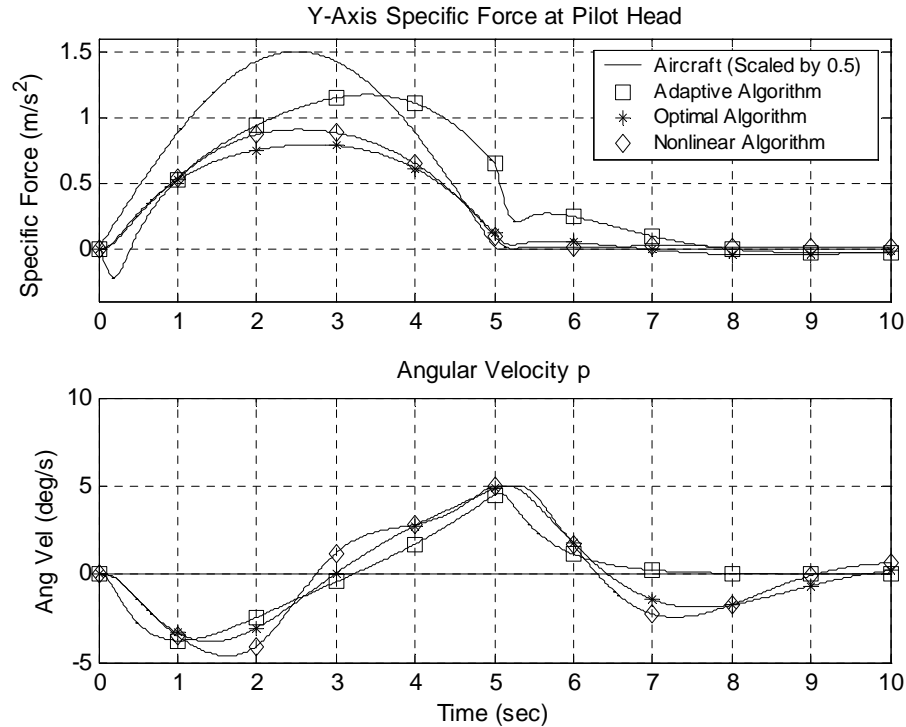
126

Figure 6.16. Algorithm Responses to Sway Half Sine of 3 m/s^2 Magnitude, 5-Second Duration.

Figure 6.17 compares the responses for these sway cues from the integrated perception model. As expected, the nonlinear algorithm peaks to a larger sensed specific force as compared to the optimal algorithm, resulting in a larger perceived velocity. After five seconds, the conflict between the vestibular and visual stimuli is reduced, resulting in a gradual acceptance of the visual cues governed by the optokinetic influence in the model. The problems noted with the adaptive algorithm are evident; the false cue and delayed peak are noticeable along with excessive sensed and perceived responses observed in the last two seconds of the pulse input. In all three algorithms, the magnitude of the vestibular cues eliminates the latency to onset of linearvection that would occur with visual stimuli alone.
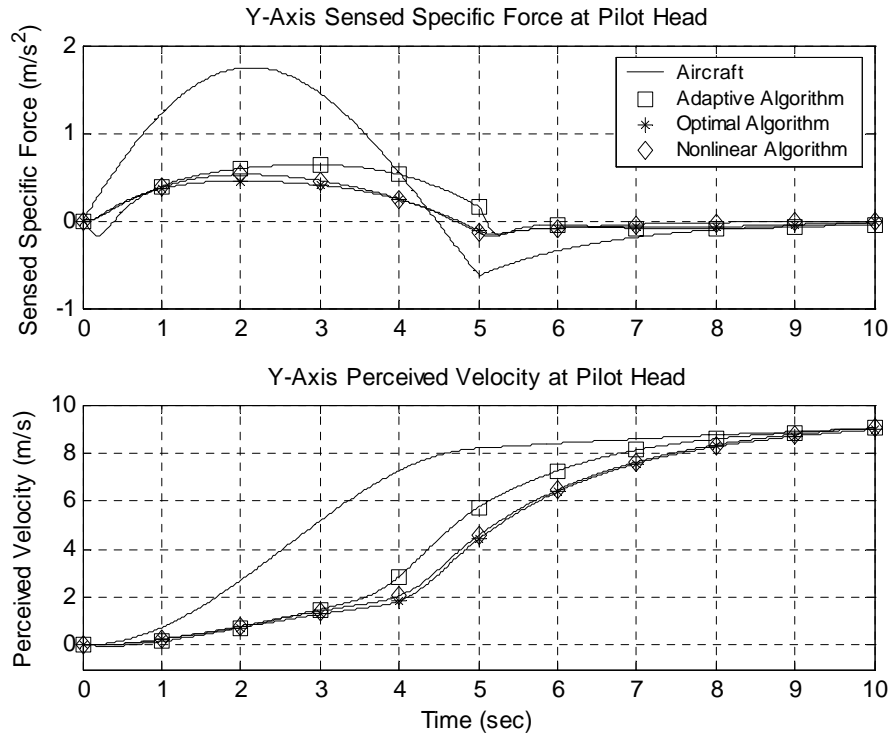
Figure 6.17. Integrated Perception Model Responses to Sway Cues of Figure 6.16.

The yaw mode responses for an angular acceleration doublet of 0.1 rad/s² magnitude and 5-second duration are shown in Figure 6.18. Both the optimal and nonlinear algorithms extend the duration of the positive angular velocity cue about one second longer than the adaptive algorithm, with the nonlinear algorithm duration being slightly longer. Note that the false angular velocity cue near the end of the aircraft input is reduced for the nonlinear algorithm. The yaw angle displacement command returns to the neutral state (zero displacement) in less than twenty seconds, while the linear optimal algorithm requires more time to return to the neutral state.
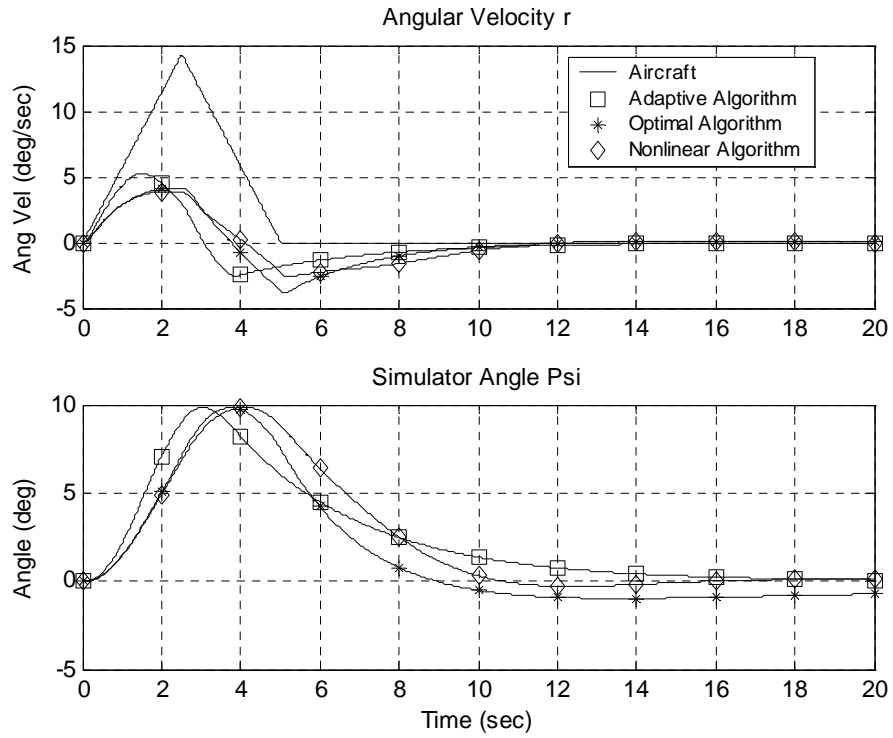
Figure 6.18. Algorithm Responses to Yaw Doublet of 0.1 rad/s^2 and 5-Second Duration.

Figure 6.19 shows the roll responses for an angular acceleration doublet of 0.1 rad/s^2 magnitude and 5-second duration. The aircraft acceleration doublet is integrated to produce the triangular angular velocity shown in Figure 6.19, and generates a specific force discontinuity at the doublet transition. Note that the specific force response for the nonlinear algorithm is about the same magnitude in comparison to the optimal and adaptive algorithm responses.
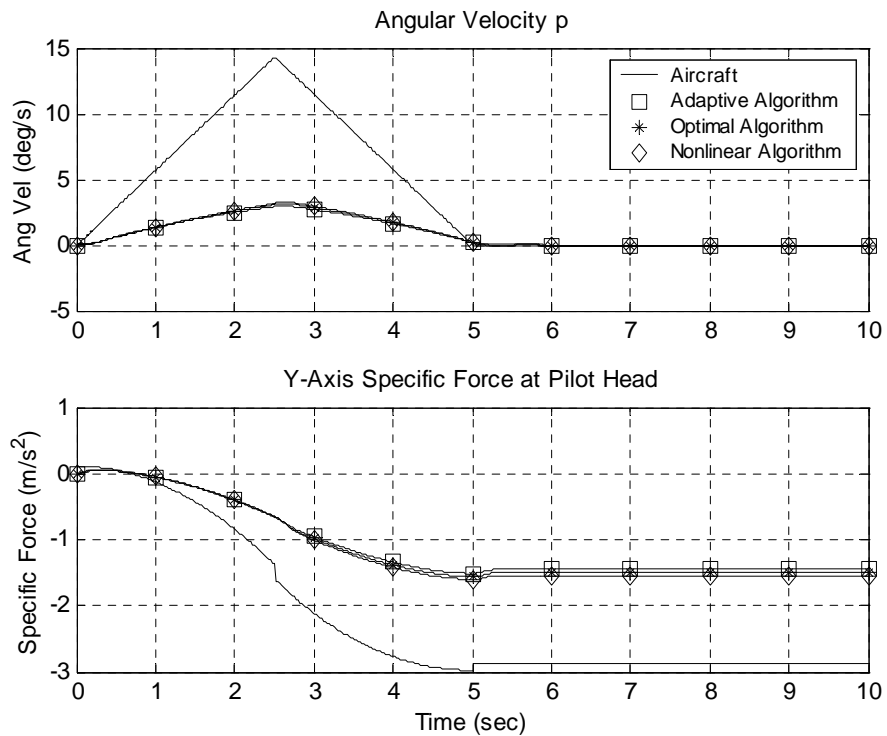

Figure 6.19. Algorithm Responses to Roll Doublet of 0.1 rad/s^2 and 5-Second Duration.

Figure 6.20 shows the pitch responses of the same magnitude and duration for all three algorithms. Similar aircraft inputs to the roll degree-of-freedom are observed. Note that for a single degree-of-freedom pitch input (e.g., pitch during straight and level flight), the adaptive algorithm will produce the largest angular velocity and specific force cues, with the nonlinear algorithm cues being less than the optimal algorithm. However, with the addition of longitudinal cues generated during a takeoff maneuver, the aircraft inertial acceleration will penalize or decrease the angular velocity gain as governed by the cost function of Eq. (2.11).
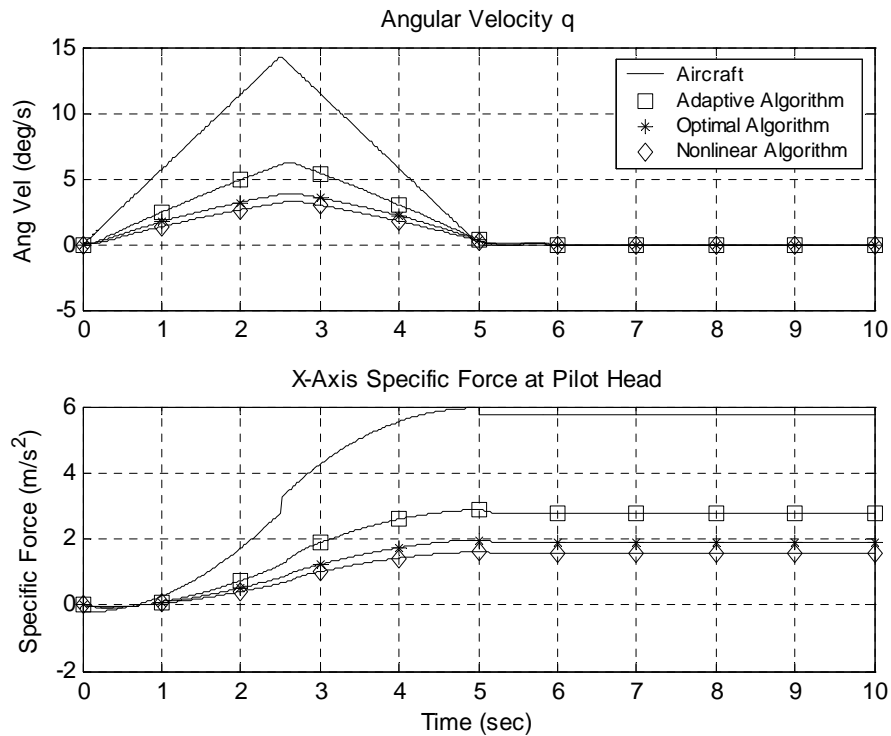

Figure 6.20. Algorithm Responses to Pitch Doublet of 0.1 rad/s^2 and 5-Second Duration.

6.7. Turbulence

Reid and Robinson [65] first addressed the problem of producing acceptable motion cues to turbulent gust inputs. They noted that heave is the most critical cue in representing turbulence, but is also the most restricted cue when constraining motion within the platform geometry. To overcome this limitation, they developed an approach in which a second set of aircraft flight equations driven only by the turbulence inputs is employed. The output from this augmented channel is then added to the output from the primary flight equations, being driven by both turbulence and the pilot control inputs, before serving as input to the motion system. A similar approach to that developed by Reid and Robinson [65] has been implemented and is shown in Figure 6.21.
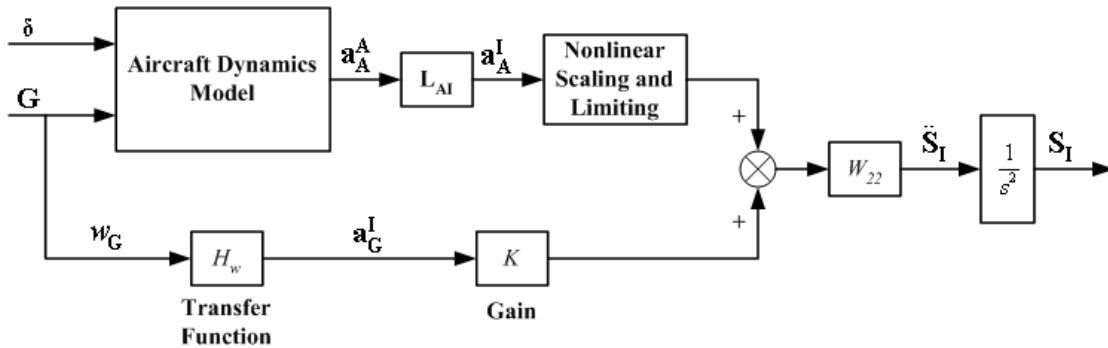

Figure 6.21. Optimal Algorithm Vertical Mode with Augmented Turbulence Channel.

The input to the augmented channel is the z-axis component w_G of the turbulence vector **G**. Reid and Robinson showed that w_G is the dominant turbulence component needed in producing vertical acceleration due to turbulence. The secondary flight equations can then be represented by a transfer function $H_G(s)$. The secondary acceleration $\mathbf{a}_G^I$ is then scaled with a constant gain K_G. Both the primary and secondary signals are then combined before input to the vertical motion cueing filter W_{22}.

From a simulated aircraft test run, a system identification of aircraft vertical accelerations in response to turbulence was performed. The transfer function $H_G(s)$ was then created to not only represent the acceleration, but also incorporate some desired motion cueing characteristics, i.e., attenuated low-frequency content and increased high-frequency content. The following second-order transfer function was obtained for $H_G(s)$:

$$H_G(s) = 0.1 \frac{(2.4s+1)(2.4s+1)}{(0.4s+1)(0.1s+1)}.$$ (6.42)

For the optimal algorithm, a gain of K_G equal to 0.8 was chosen to maximize the desired sensation of turbulence while keeping the actuator extensions within the motion limits. Figure 6.22 shows the optimal algorithm vertical responses due to turbulence both with and without the augmented channel. Note that the addition of the channel results in larger specific force peaks along with greater z-axis displacement. Figure 6.23 shows the power spectral density (PSD) of the heave acceleration cues. Note that the addition of the augmented turbulence channel greatly increases the PSD for low and mid-range frequencies up to 3 Hz.

A similar implementation to that shown in Figure 6.21 was applied to the nonlinear algorithm. In this approach, the linear cueing filter W_{22} was replaced with the nonlinear heave filter, with the gain K_G set equal to 1.2. Figure 6.24 shows the nonlinear algorithm vertical responses due to turbulence. Note that the augmented channel results in larger specific forces and displacements than the optimal algorithm, with a similar increase in the power spectral densities as shown in Figure 6.25.
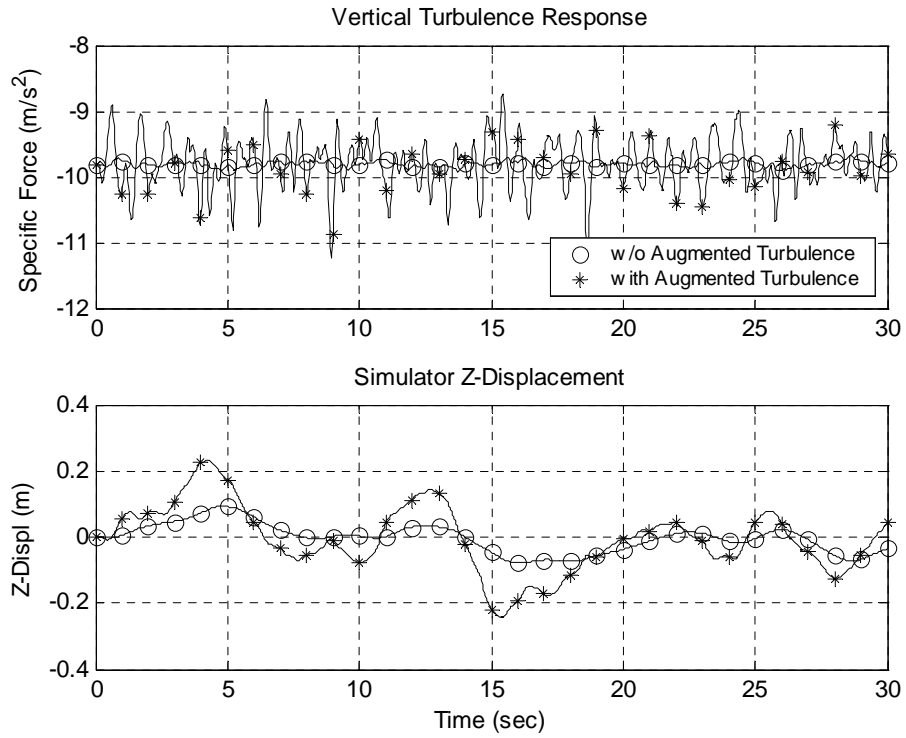
Figure 6.22. Optimal Algorithm Motion Cues Due to Turbulence.
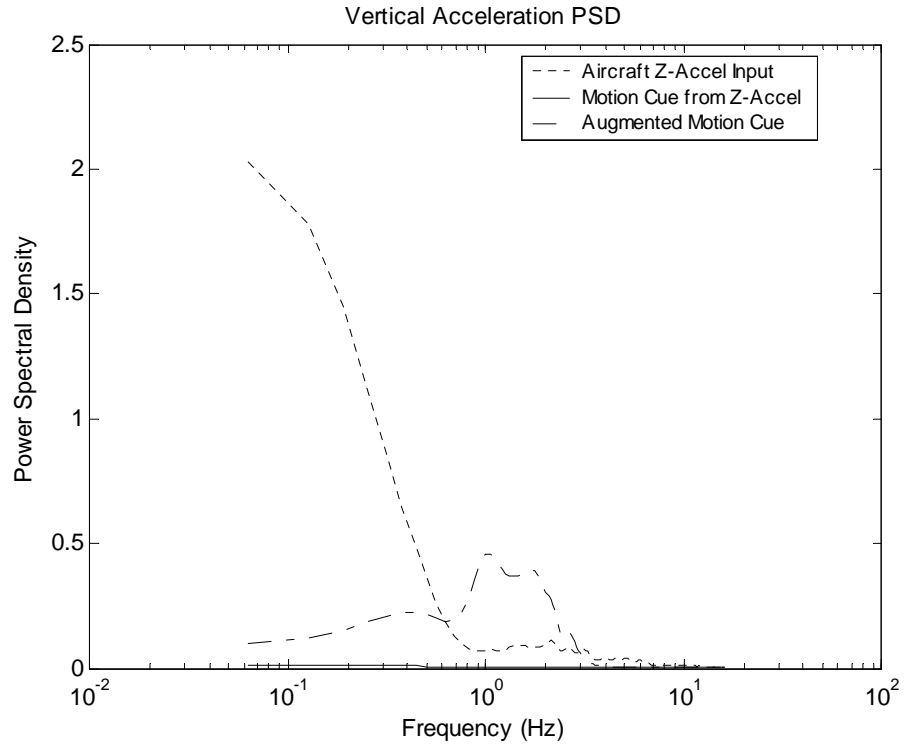

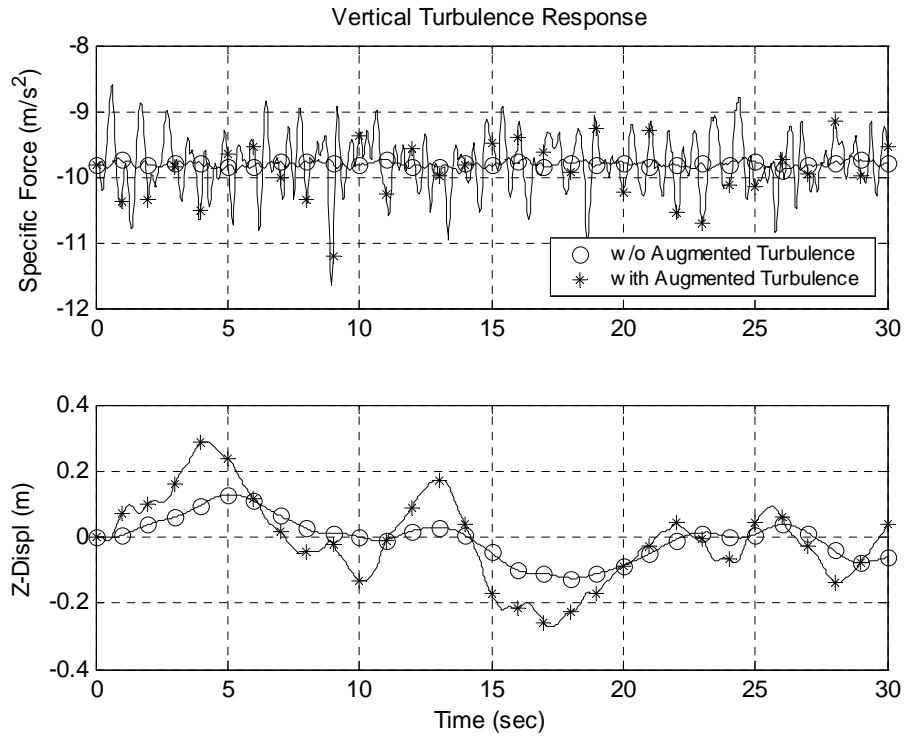**Figure 6.23. Power Spectral Density of Optimal Algorithm Motion Cues.**

134

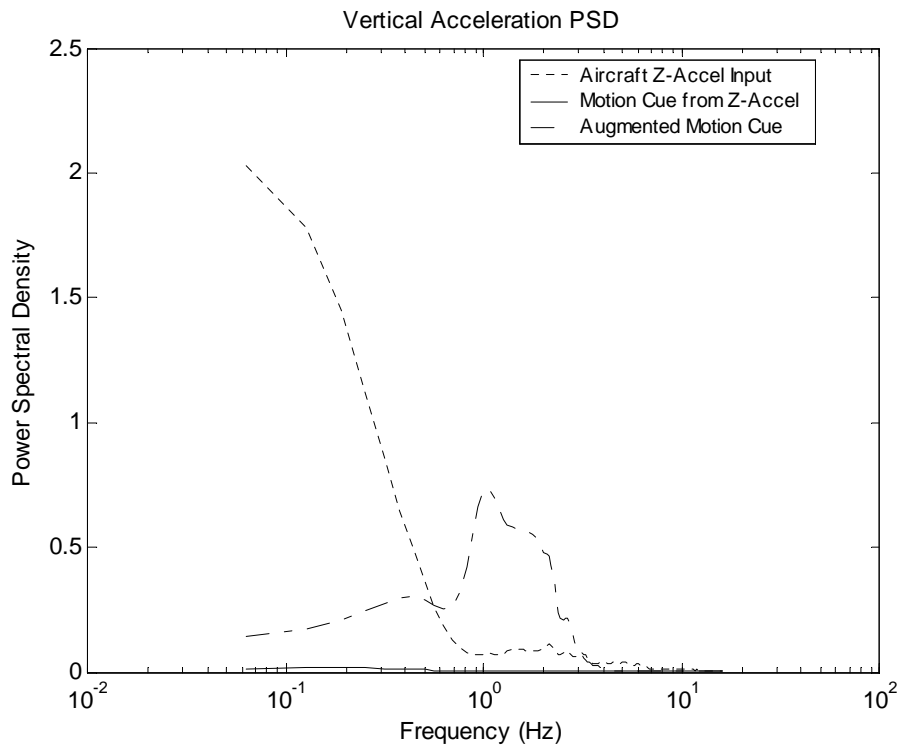**Figure 6.24. Nonlinear Algorithm Motion Cues Due to Turbulence.**

Figure 6.25. Power Spectral Density of Nonlinear Algorithm Motion Cues.

6.8. Summary of Results

The inclusion of the integrated perception model to the linear algorithm formulation will, in general, sustain the motion cues longer compared to the formulation solely based on the vestibular system. However, this would result in excessive simulator displacements that could exceed the motion system hardware limits. The addition of the nonlinear control law with a time-varying feedback matrix based upon simulator motion allows the large displacements that result from high magnitude motion cues to be washed out more quickly compared to cues of lower magnitude. The neurocomputing approach provides an effective means of updating the solution of the Riccati equation at each time step. Reducing the number of sub-iterations of the presentation vector $\mathbf{z(t)}$ results in the computation meeting the real time requirement, without degradation of the quality of the resulting motion cues.

The vertical mode responses from the nonlinear algorithm produce a washout of the motion cues that significantly reduces the z-axis displacement without requiring additional scaling of the simulated aircraft inputs. For the longitudinal mode response to a surge input, the nonlinear algorithm does not produce any difference in the specific force cue, but shows a reduction in the x-axis displacement; the percentage reduction of which compared to the linear algorithm will increase with increasing aircraft inputs. The specific force responses shown for a large half-sine sway input to the lateral mode are unchanged, but again show a significant reduction with the y-axis displacement.

The effect of the nonlinear algorithm on the yaw mode differs from the translational modes as the duration of the angular velocity cue is increased and a false cue is decreased; both effects increasing the simulator yaw displacement. A maximum limit

was needed on the nonlinearity α to control this increase in displacement. For pitch and roll degree-of-freedom inputs, the nonlinear algorithm could not yield any change in the motion cues. A unity-gain filter replaced the respective state space motion cueing filter in the longitudinal and lateral modes.

The responses to single degree-of-freedom aircraft inputs were compared with the NASA adaptive algorithm and the optimal algorithm. Results for the vertical mode show the nonlinear algorithm producing a motion cue with a time-varying washout, sustaining small cues for a longer duration and washing out larger cues more quickly compared to the optimal algorithm. The longitudinal mode response to a surge input results in a specific force response with no steady-state washout due to the addition of the integrated perception model in the algorithm formulation. The onset of the surge response eliminates the false cue that persists with the adaptive algorithm. The lateral mode response to a sway input reveals a motion cue without the false cue or distorted shape observed with the adaptive algorithm, and a larger magnitude compared to the optimal algorithm. Yaw mode responses reveal that the nonlinear algorithm improves the motion cues by reducing the magnitude of negative cues and increasing the cue duration.

In order that takeoff maneuvers be successfully completed within the motion system hardware limits, pilot tuning resulted in reduction of the nonlinear gain of the surge degree-of-freedom. This resulted in less steady-state specific force cue compared to the adaptive algorithm. The pitch degree-of-freedom nonlinear gain was also reduced, resulting in less angular velocity cues compared to the optimal algorithm. These results are investigated further with pilot performance testing [66].

This page intentionally left blank.

7. Conclusions and Future Research

7.1. Conclusions

An improved linear optimal algorithm was developed that incorporates the latest research on human vestibular sensation models. Using these new models, a set of linear motion cueing filters were synthesized and tuned using optimal control techniques. Preliminary pilot tests revealed unsatisfactory perception of turbulence effects. A filter for the vertical mode based upon a revised otolith model resulted in a significant increase in the magnitude of the high-frequency gain, resulting in faster responding heave cues. A filter for the longitudinal mode was designed with the new otolith model and resulted in faster responding surge cues with a reduction in the tilt coordination rate.

The revised otolith sensation model, derived from prior research, was formulated with a short time constant obtained from research with afferent responses that shows one order-of-magnitude reduction from past work with ocular torsion responses. The physiological experiments from the literature produced transfer functions with a fractional exponent in the lead operator. By applying fractional calculus, transient responses to impulse and step inputs have been derived. Comparison of the transient response of the revised model with these responses clearly shows that a less complex model can generate a response that is a reasonable approximation between responses from the regular and irregular units.

An integrated model of human motion perception was developed. This model includes models of both vestibular and visual motion sensation and incorporates the nonlinear interaction between the vestibular and visual stimuli. The visual estimate of perceived self-motion is modeled as an optokinetic influence that filters the difference

between the cues through a first-order low-pass filter that represents the gradual build-up of self-velocity. A conflict signal estimator is used to control the optokinetic influence gain. Models for both rotational and translational motion were developed, producing responses that explain the characteristics of self-motion observed in the literature.

A nonlinear motion cueing algorithm was developed that combines features of the adaptive and linear optimal algorithms, and incorporates the vestibular and integrated perception models. A nonlinear control law was implemented that requires the solution of the Riccati equation in real time. The neurocomputing approach implemented for this task yields responses that are robust with respect to the closed-loop eigenvalues, with less computational burden compared to a second neurocomputing solver and a Newton-Raphson implementation.

Results for the vertical mode show the nonlinear algorithm producing a motion cue with a time-varying washout, sustaining small cues for a longer duration and washing out larger cues more quickly. The addition of the integrated perception model was shown to improve the response to a surge input, producing a specific force response with no steady-state washout. Improved cues are also observed for responses to a sway input. The false longitudinal and lateral cues observed with the NASA adaptive algorithm were absent. Yaw mode responses reveal that the nonlinear algorithm improves the motion cues by reducing the magnitude of negative cues closer to perceptual thresholds. The addition of the augmented turbulence cue to the heave mode for both the optimal and nonlinear algorithms increases the turbulence sensation significantly so that pilot control inputs are influenced.

7.2. Suggested Future Research

Both the optimal and nonlinear algorithm formulations resulted in rotational pitch filters with frequency characteristics very close to a unity-gain filter. For large aircraft inputs, these filters produce strong pitch cues with large pitch angles that do not wash out. This can result in either the simulation being stopped due to the motion limits being exceeded, or the motion cues being further restrained by a limiting or braking algorithm. Modifying the pitch filter to provide washout capability would allow large pitch angles to gradually decrease to a neutral position and increase the likelihood that simulations with large pitch angles such as takeoff be successfully completed. The pitch filter in the optimal algorithm longitudinal mode formulation can be modified to produce washout by reducing the weight component $\mathbf{R}_d(4,4)$ that constrains the simulator pitch angle from Eq. (4.17).

For the nonlinear algorithm, the corresponding weight component $\mathbf{R}_d(4,4)$ was removed from the cost function to eliminate a zero closed-loop eigenvalue, resulting in improved convergence of the Riccati equation neurocomputing solver. Producing washout capability with the pitch filter would require additional research with the neurocomputing solver to improve convergence with a closed-loop eigenvalue of zero, or an augmented approach that would address this problem separately.

A braking algorithm developed by Wu [13] was implemented for both algorithms and is presented with the motion cueing program implementation [64]. This braking algorithm did an adequate job of restraining the simulator motion as the hardware limits were approached, but performed poorly in returning motion control to the cueing algorithm. An improved algorithm that is effective in both restraining large excursions

and resuming regular simulator motion would allow increased nonlinear gains and improve motion cueing performance. One approach that is suggested is the algorithm developed by McFarland [67] for NASA Ames.

The performance of the nonlinear algorithm will improve when implemented on a new motion system with improved actuator extensions and bandwidth. Surge and pitch gains can be increased to improve pilot performance. Due to the algorithm producing faster washout with large motion cues, the necessity for a braking algorithm to address large excursions may be minimal. The addition of a pitch filter with washout would further improve the available motion cues. This improved nonlinear algorithm could then be evaluated with a large homogeneous group of test pilots using the same state of the art techniques [66] developed for this research.

Appendix A. Fractional Exponent Derivation

Because of the fractional exponent in the transfer function of Eq. (3.22), an elementary solution to its response cannot be readily obtained. However, an approximate solution to the response can be derived through the application of fractional calculus [32].

By first substituting the regular unit parameters into Eq. (3.22) and then implementing partial fraction expansion, Eq. (3.22) becomes

$$H(s) = \frac{1792.056}{s+62.5} + 674.058 \frac{s^{0.188}}{s+62.5} - \frac{0.044538}{s+0.0145} - 0.016752 \frac{s^{0.188}}{s+0.0145}. \quad (A.1)$$

In Eq. (A.1), there are two groups of two transfer functions. Each group is related to either the otolith mechanics ("fast") time constant τ_M or the adaptation ("slow") time constant τ_A, with one of the two transfer functions including an exponent that represents a fractional derivative. For the first group, the solution to the term without the fractional exponent can be easily obtained by taking the inverse Laplace transform of the response:

$$L^{-1}\left(\frac{1}{s+62.5}\right) = e^{-62.5t}. \quad (A.2)$$

To derive a solution to the fractional exponent term, The inverse Laplace transform is first obtained by applying fractional calculus [32]:

$$L^{-1}\left(\frac{s^{-\nu}}{s-a}\right) = E_t(\nu, a), \quad (A.3)$$

where $a = $ -62.5, $\nu = $ -0.188, and the term $E_t(\nu, a) = t^\nu e^{at} \gamma^*(\nu, at)$, with γ^* being the incomplete gamma function, a transcendental function that can be expressed as

$$\gamma^*(\nu, at) = t^{-at} \sum_{k=0}^{\infty} \frac{(at)^k}{\Gamma(\nu+k+1)}. \quad (A.4)$$

Substituting Eq. (A.4) into Eq. (A.3) will result in

143

$$L^{-1}\left(\frac{s^{-\nu}}{s-a}\right) = E_t(\nu, a) = t^{\nu}\sum_{k=0}^{\infty}\frac{(at)^k}{\Gamma(\nu+k+1)}. \qquad (A.5)$$

Eq. (A.5) is an infinite series, which for $\nu = 0$ will reduce to the Taylor series expansion of the exponential function:

$$L^{-1}\left(\frac{s^0}{s-a}\right) = L^{-1}\left(\frac{1}{s-a}\right) = E_t(0, a) = \sum_{k=0}^{\infty}\frac{(at)^k}{\Gamma(k+1)} = e^{at}, \qquad (A.6)$$

where for $a = -62.5$, the solution is the same as Eq. (A.2).

$$f'(t) = t^{\nu-1}\sum_{k=0}^{\infty}\frac{(at)^k}{\Gamma(\nu+k)}, \qquad (A.7)$$

where $f(t)$ satisfies the first-order ordinary differential equation

$$f'(t) - af(t) = t^{\nu-1}/\Gamma(\nu), \qquad (A.8)$$

with the solution

$$f(t) = E_t(\nu, a) = \frac{e^{at}\int_0^t e^{-au}u^{\nu-1}du}{\Gamma(\nu)}, \nu \geq 1, \qquad (A.9)$$

Note that in Eq. (A.9) the integral does not exist when ν - 1 is less than 0. To overcome this problem, we use the recursion formula

$$E_t(\nu, a) = \frac{t^{\nu}}{\Gamma(\nu+1)} + aE_t(\nu+1, a)$$

$$= \frac{t^{\nu}}{\Gamma(\nu+1)} + \frac{at^{\nu+1}}{\Gamma(\nu+2)} + \frac{a^2 e^{at}}{\Gamma(\nu+2)}E_t(\nu+2, a) \qquad (A.10)$$

$$= \frac{t^{\nu}}{\Gamma(\nu+1)} + \frac{at^{\nu+1}}{\Gamma(\nu+2)} + \frac{a^2 e^{at}}{\Gamma(\nu+2)}\int_0^t e^{-au}u^{\nu+1}du.$$

Note that the integral in Eq. (A.10) now exists since $\nu + 1$ is greater than 0. Eq. (A.10) can now be used to compute the responses of the two fractional exponent transfer

144

functions given in Eq. (A.1). For each of these transfer functions, three terms are computed. The first two terms are analytical functions with the third term including an integral that requires an approximate solution.

To evaluate the integral in Eq. (A.10), the integral can be rewritten as

$$
\begin{aligned}
I(t) &= e^{-at}\int_0^t e^{-a(u-t)}u^{v+1}du \\
&= e^{-at}\int_0^1 e^{-at(z-1)}t^{v+1}z^{v+1}dz \\
&= t^{v+2}e^{-at}\tilde{I}(t),
\end{aligned}
\tag{A.11}
$$

where $\tilde{I}(t) = \int_0^1 e^{at(1-z)}z^{v+1}dz$. Note that as $at \to -\infty$, the integrand in $\tilde{I}(t)$ approaches 0 for $0 \le z \le 1$, and 1 for $z = 1$. Also, for z near $z = 1$, we can write

$$
z^{v+1} = 1 + (v+1)(z-1) + \frac{(v+1)v(z-1)^2}{2!} + \cdots = \sum_{j=0}^{\infty} C_j(z-1)^j.
\tag{A.12}
$$

This suggests we can write the integrand in $\tilde{I}(t)$ as

$$
f(z) = e^{at(1-z)}\left(\sum_{j=0}^{N} C_j(z-1)^j + z^{v+1} - \sum_{j=0}^{N} C_j(z-1)^j \right),
\tag{A.13}
$$

and therefore $\tilde{I}(t)$ can be rewritten as

$$
\tilde{I}(t) = \sum_{j=0}^{N} C_j \int_0^1 e^{at(1-z)}(z-1)^j \, dz + R_N(t),
\tag{A.14}
$$

where

$$
R_N(t) = \int_0^1 e^{at(1-z)}\left(z^{v+1} - \sum_{j=0}^{N} C_j(z-1)^j \right)dz,
\tag{A.15}
$$

and $|R_N(t)| \le K/(-at)^{N+1}$ as $at \to -\infty$, where K is a constant. The integral $I(t)$ in Eqn. (A.11) can now be evaluated as

$$I(t) = t^{\nu+2} e^{-at} \left\{ \sum_{j=0}^{N} C_j \int_0^1 e^{at(1-z)} (z-1)^j \, dz \; + \; O\left(\frac{1}{(-at)^{N+1}} \right) \right\} \qquad \text{(A.16)}$$

By taking the inverse Laplace transform of Eq. (A.1) and applying Eqs. (A.10) and (A.16) to the transfer functions with fractional exponents results in the impulse response $h(t)$:

$$h(t) = 1792.056 e^{-62.5t} + 674.058 \, E_t(-0.188, -62.5)$$
$$- 0.044538 e^{-0.0145t} - 0.016752 \, E_t(-0.188, -0.0145) \qquad \text{(A.17)}$$

The response to a unit step input will now be considered. Given a system with the initial conditions $x = 0$ and $\dot{x} = 0$ when $t = 0$, and an arbitrary input $u(t)$, we look for a solution in the form

$$x(t) = \int_0^t h(x, \tau) u(\tau) d\tau, \qquad \text{(A.18)}$$

where $h(x, \tau)$ is Green's function, i.e. the system response to an impulse input, and has already been derived for the regular and unit transfer function in Eq. (A.17). If we consider the response to a unit step, i.e. $u(\tau) = 1$ for t > 0, the response for a term without the fractional exponent is simply $\int_0^t e^{a\tau} d\tau = \frac{1}{a}(e^{at} - 1)$, while the response for a term with the fractional exponent from Eq. (A.10) is

$$\int_0^t E_\tau(\nu, a) \, d\tau = E_t(\nu + 1, a), \qquad \text{(A.19)}$$

and applying the recursion formula in Eq. (A.19) results in

$$E_t(\nu + 1, a) = \frac{1}{a}\left(E_t(\nu, a) - \frac{t^\nu}{\Gamma(\nu + 1)} \right). \qquad \text{(A.20)}$$

Applying Eqs. (A.18) and (A.20) to the impulse response for the regular unit parameters given in Table 3.1 and combining terms results in the response to a unit step:

$$
\begin{aligned}
x(t) = {}& 25.601 - 28.673e^{-62.5t} + 3.073e^{-0.014493t} \\
& - 10.786E_t(-0.188, -62.5) + 1.156E_t(-0.188, -0.014493) \quad\quad \text{(A.21)} \\
& + 9.629\frac{t^{\nu}}{\Gamma(\nu+1)}.
\end{aligned}
$$

This page intentionally left blank.

Appendix B. Optimal Algorithm System Parameters and Filter Characteristics

Table B.1. Optimal Algorithm System Parameters

Parameter	Pitch/Surge	Roll/Sway	Yaw	Heave
Semicircular Canals				
Threshold (deg/sec)	2.0	2.0	1.6	
τ_1 (sec)	5.73	5.73	5.73	
τ_2 (sec)	0.005	0.005	0.005	
τ_a (sec)	80	80	80	
τ_L (sec)	0.06	0.06	0.06	
G_{SCC} (Threshold Units)	28.6479	28.6479	35.8099	
Otolith				
Threshold (m/sec^2)	0.17	0.17		0.28
A_O (sec^{-1})	0.1	0.1		0.1
B_O (sec^{-1})	0.2	0.2		0.2
B_1 (sec^{-1})	62.5	62.5		
G_{OTO} (Threshold Units)	4.7059* B_1	4.7059* B_1		2.8571
Filtered White Noise Break Frequency				
$A_n(1,1)$	1	1	1	1
$A_n(2,2)$	π	π		
Penalty Weights				
$Q(1,1)$	1	1	1	1
$Q(2,2)$	10	10		
$R_d(1,1)$	8	8	0.1	0.1
$R_d(2,2)$	4	4	300	4
$R_d(3,3)$	1	1		1
$R_d(4,4)$	250	250		
$R(1,1)$	1	1	1	1
$R(2,2)$	1	1		

Table B.2. Optimal Algorithm Filters with Young-Meiry Otolith Model.

Poles	$W_{11}(s)$ Zeros	$W_{12}(s)$ Zeros	$W_{22}(s)$ Zeros
Longitudinal (Pitch/Surge) Filter			
-68.1595	-68.7884	-200	-83.3944
-7.0133	-6.5825	-11.0387-14.9159i	-13.4373
-0.6401-0.9364i	-0.6880-0.9932i	-11.0387+14.9159i	-1.9681
-0.6401+0.9364i	-0.6880+0.9932i	-0.3930-0.3584i	0
-1.1077-0.1855i	-1.0203-0.3224i	-0.3930+0.3584i	0
-1.1077+0.1855i	-1.0203+0.3224i	-0.0468	0
-0.0774	-0.0753	0	0
Lateral (Roll/Sway) Filter			
-59.9780	-60.4781	-200	-77.7778
-7.9333	-7.4642	-11.7349-13.9453i	-13.6704
-0.6034-0.9274i	-0.6391-0.9757i	-11.7349+13.9453i	-1.9129
-0.6034+0.9274i	-0.6391+0.9757i	-0.3862-0.3524i	0
-1.0354-0.2332i	-0.9707-0.3186i	-0.3862+0.3524i	0
-1.0354+0.2332i	-0.9707+0.3186i	-0.0440	0
-0.0774	-0.0753	0	0
Vertical (Heave) Filter			
-5.6454			-48.1817
-0.5503-0.4841i			-0.1827
-0.5503+0.4841i			0
-0.1865			0
-0.1587			0
Yaw Filter			
-16.6776	-11.8526		
-0.4070	-0.1429		
-0.1944	0		
-0.0316	0		

Table B.3. Optimal Algorithm Filters with New Otolith Model.

Poles	$W_{11}(s)$ Zeros	$W_{12}(s)$ Zeros	$W_{22}(s)$ Zeros
Longitudinal (Pitch/Surge) Filter			
-13.4477	-13.0429	-1436	-5.5720
-0.5214-0.8914i	-0.5317-0.9162i	-3.2046	-1.5649
-0.5214+0.8914i	-0.5317+0.9162i	-0.3868-0.3566i	0
-0.9031-0.2666i	-0.8718-0.2961i	-0.3868+0.3566i	0
-0.9031+0.2666i	-0.8718+0.2961i	-0.0762	0
-0.1018	-0.0995	0	0
Lateral (Roll/Sway) Filter			
-13.4477	-13.0429	-1436	-5.5720
-0.5214-0.8914i	-0.5317-0.9162i	-3.2046	-1.5649
-0.5214+0.8914i	-0.5317+0.9162i	-0.3868-0.3566i	0
-0.9031-0.2666i	-0.8718-0.2961i	-0.3868+0.3566i	0
-0.9031+0.2666i	-0.8718+0.2961i	-0.0762	0
-0.1018	-0.0995	0	0
Vertical (Heave) Filter			
-0.5870-0.5120i			-0.1943
-0.5870+0.5120i			0
-0.1993			0
-0.1587			0
Yaw Filter			
-16.6662	-11.7582		
-0.4429	-0.1420		
-0.1506	0		
-0.0183	0		

Appendix C. Nonlinear Algorithm System Parameters

Table C.1. Nonlinear Algorithm System Parameters

Parameter	Pitch/Surge	Roll/Sway	Yaw	Heave
Semicircular Canals				
Threshold (deg/sec)	2.0	2.0	1.6	
τ_1 (sec)	5.73	5.73	5.73	
τ_A (sec)	80	80	80	
G_{SCC} (Threshold Units)	28.6479	28.6479	35.8099	
τ_{OK} (sec)	2.0	2.0	2.0	
Otolith				
Threshold (m/sec^2)	0.17	0.17		0.28
A_O (sec^{-1})	0.1	0.1		0.1
B_O (sec^{-1})	0.2	0.2		0.2
B_1 (sec^{-1})	62.5	62.5		
G_{OTO} (Threshold Units)	4.7059* B_1	4.7059* B_1		2.8571
τ_{OK} (sec)	2.0	2.0		2.0
Filtered White Noise Break Frequency				
A_{n11}	1	1	1	20π
A_{n22}	π	π		
Linear Weights				
$Q(1,1)$	1	1	1	1
$Q(2,2)$	300	300		
$R_d(1,1)$	8	8	0.1	40
$R_d(2,2)$	4	4	300	400
$R_d(3,3)$	1	1		40
$R(1,1)$	1	1	1	200
$R(2,2)$	1	1		
Nonlinear Parameters				
μ	2.0×10^{-6}	2.0×10^{-6}	2.0×10^{-6}	2.0×10^{-7}
$Q_2(1,1)$	0	0	1.0	1.0
$Q_2(2,2)$	0.6	0.8		2.0
α_{max}	1.0	1.0	1.0	0.2

Appendix D. Optimal and Nonlinear Algorithm Comparison Figures
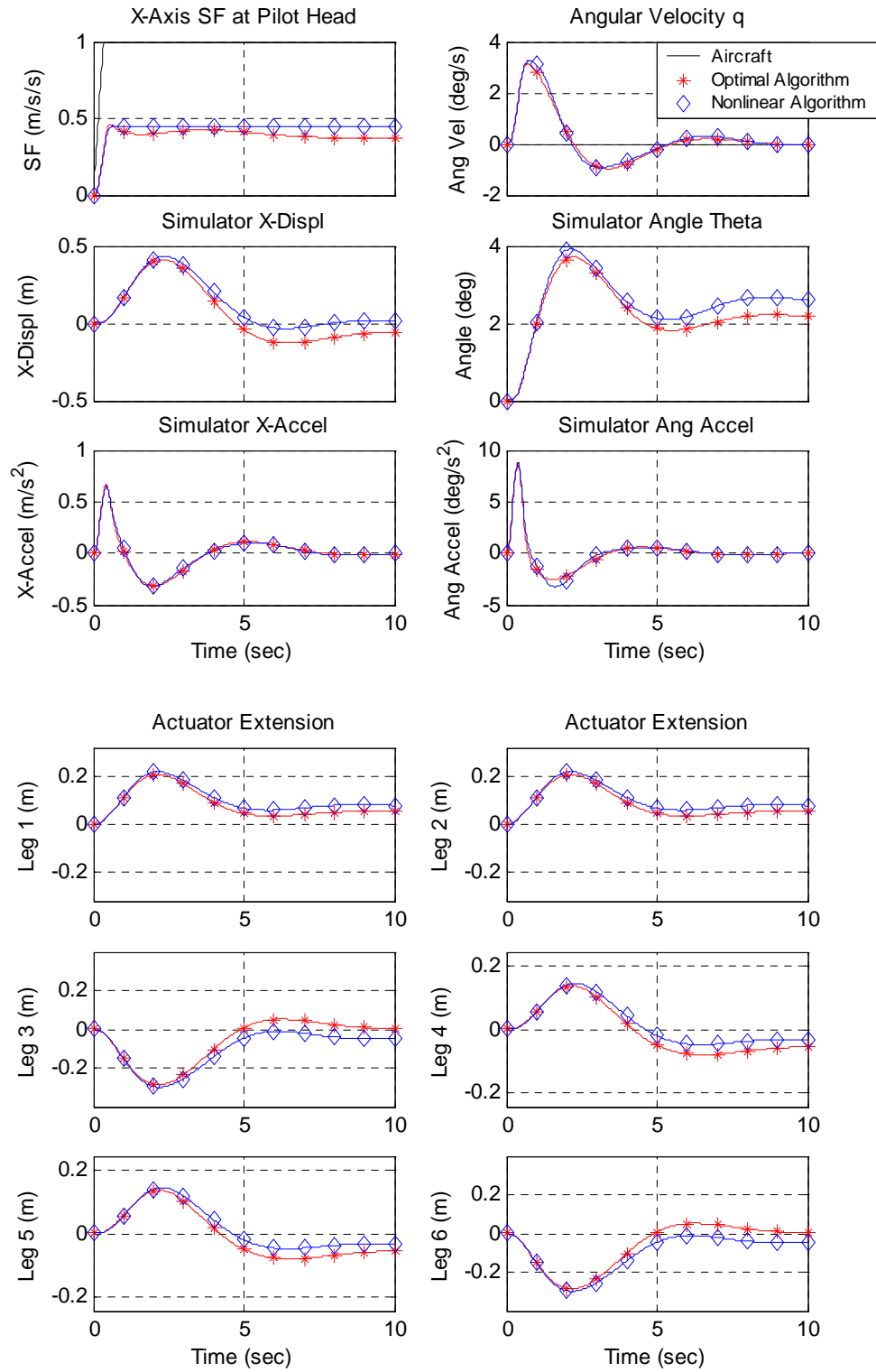

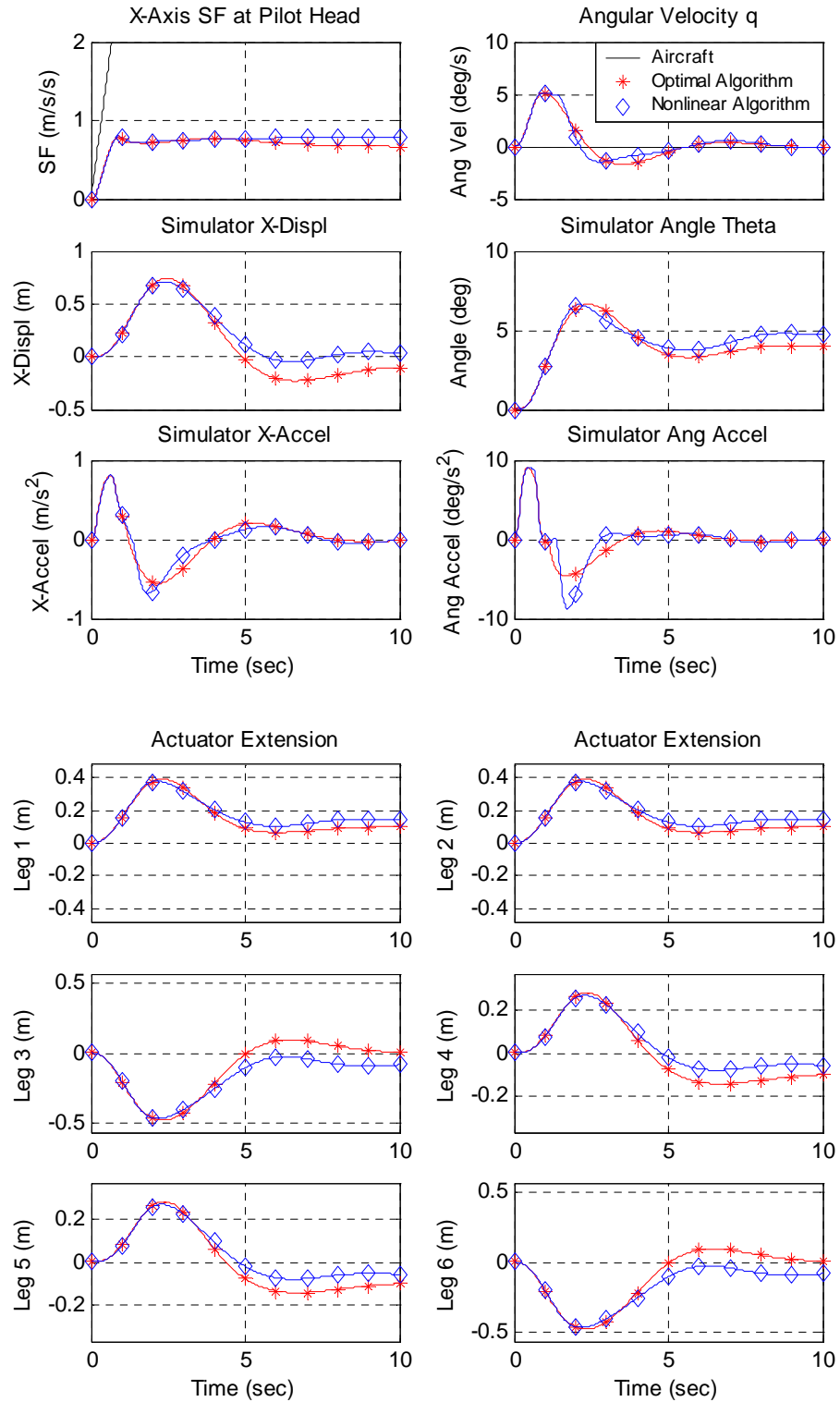**Figure D.1. Surge Ramp to Step, 1 m/s² Magnitude, 3 m/s²/s Slope.**

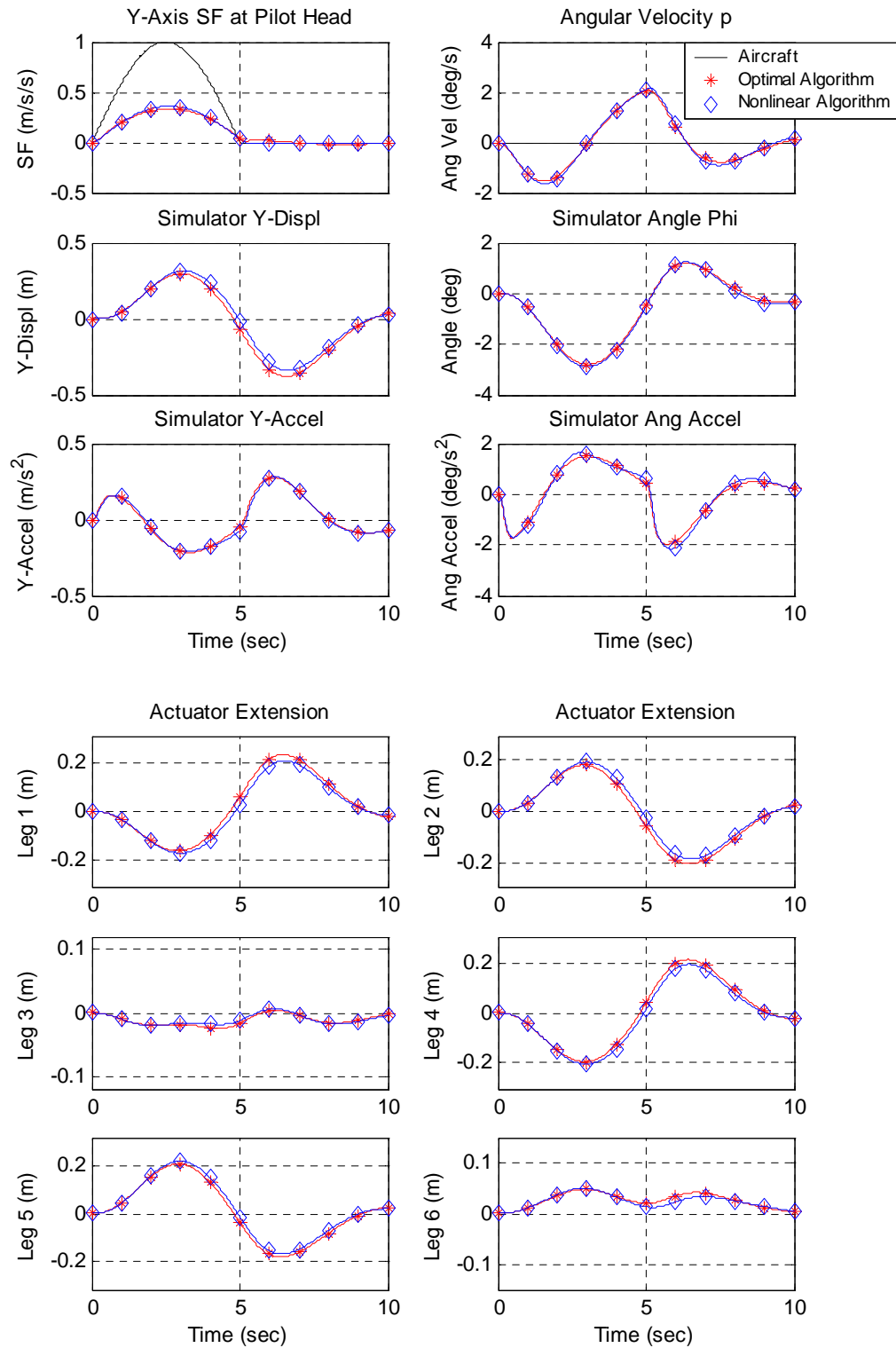**Figure D.2. Surge Ramp to Step, 2 m/s^2 Magnitude, 3 m/s^2/s Slope.**

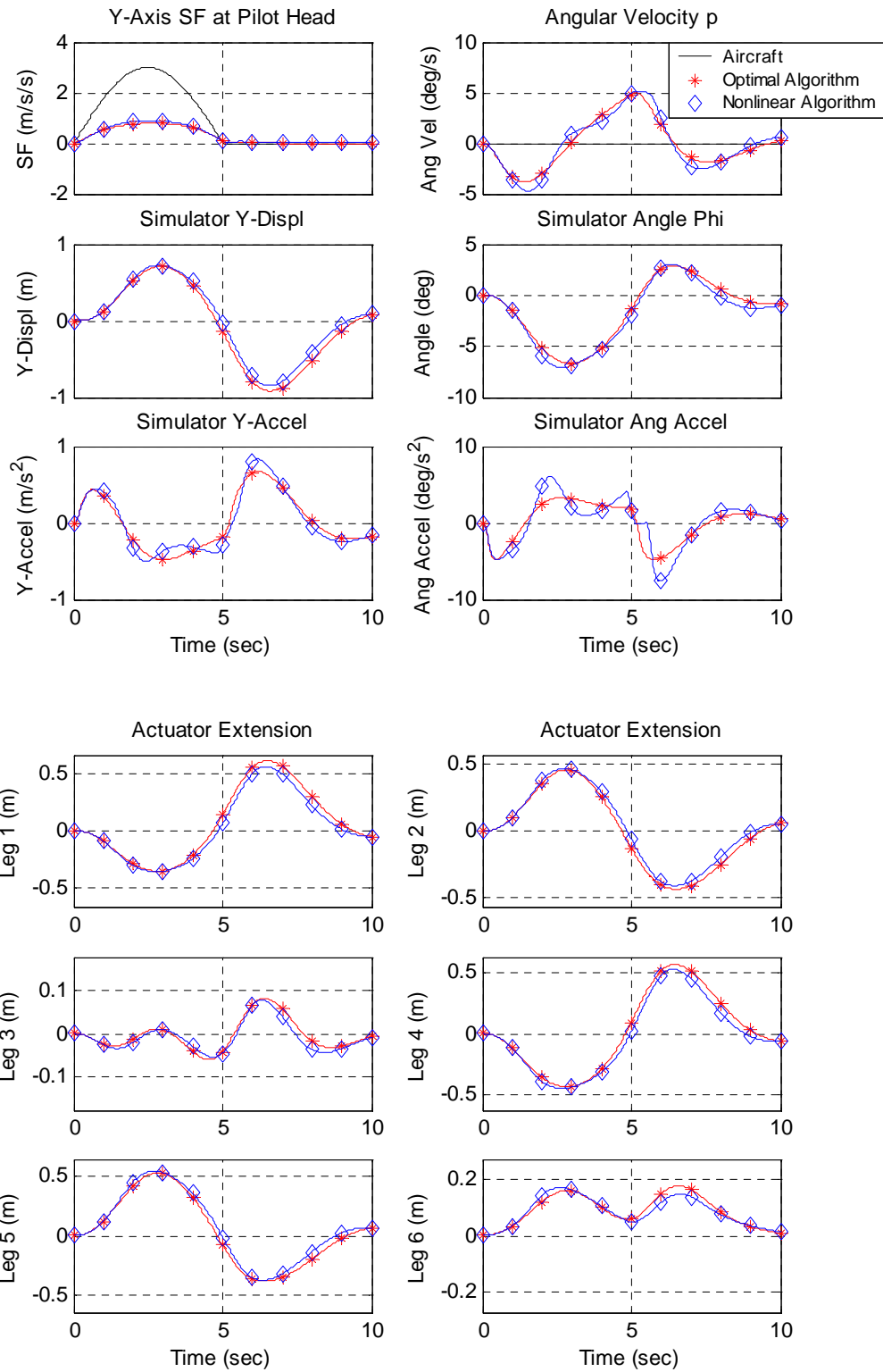**Figure D.4. Sway Half Sine, 1 m/sec^2 Magnitude, 5-Second Duration.**

Figure D.4. Sway Half Sine, 3 m/sec^2 Magnitude, 5-Second Duration.

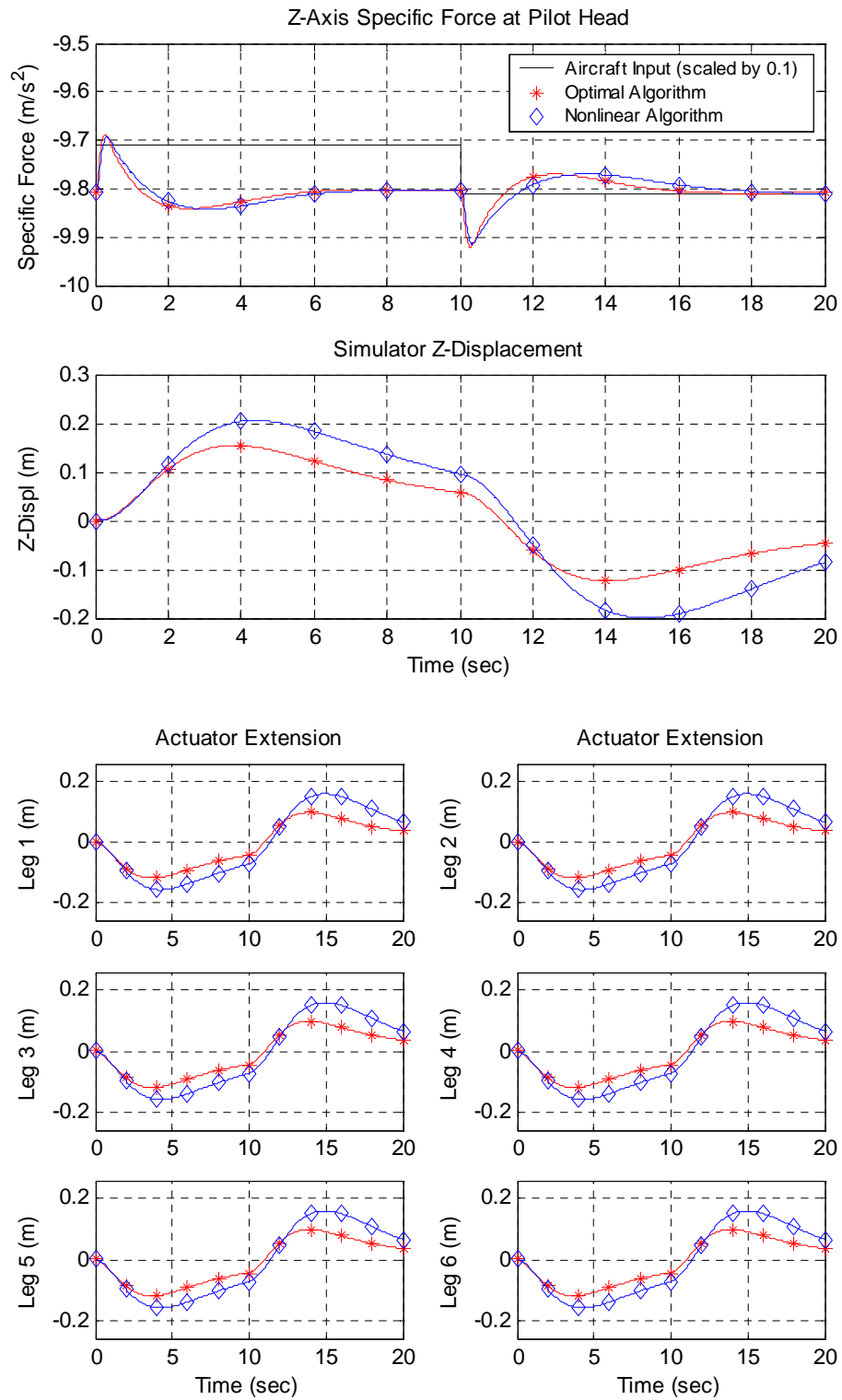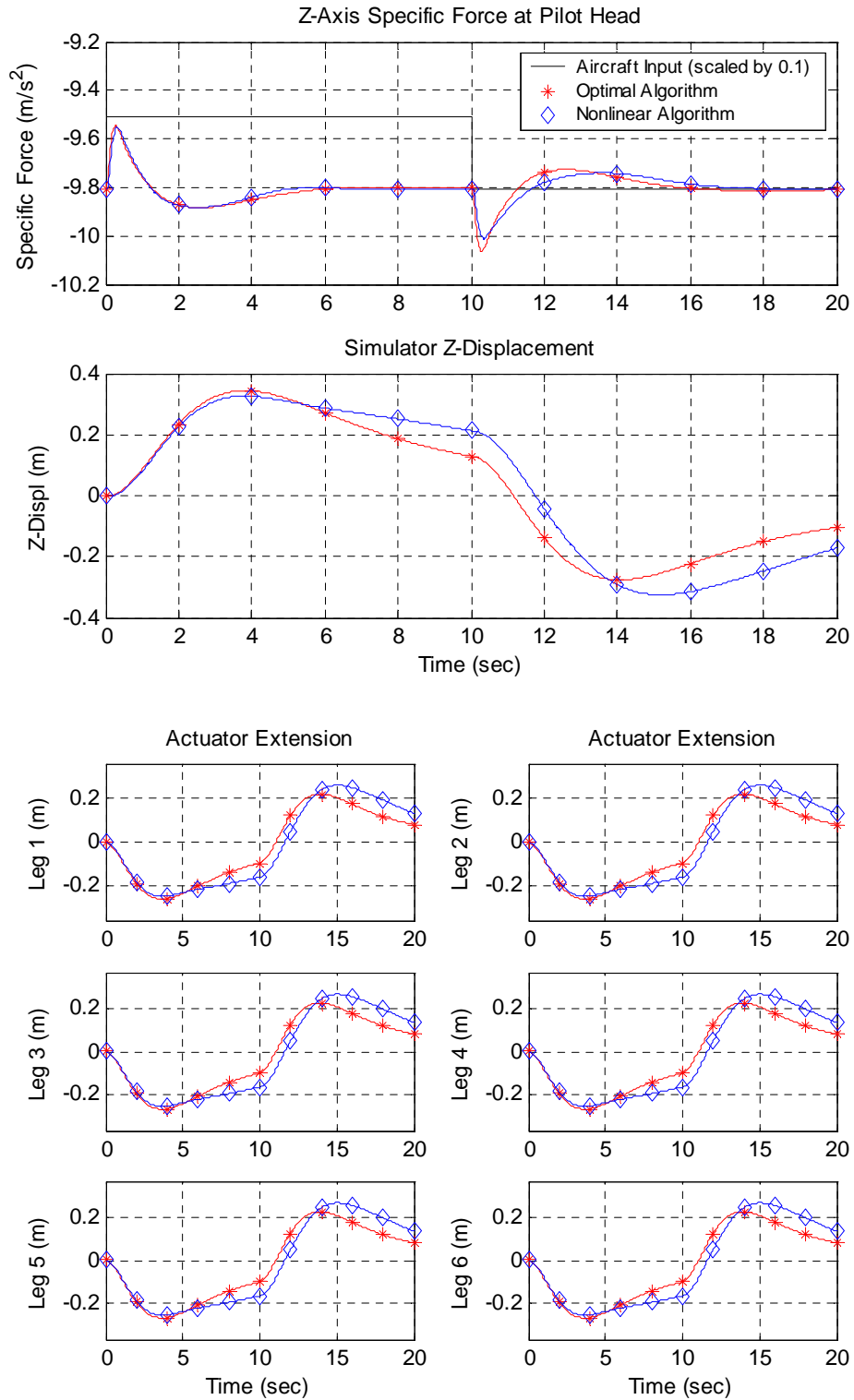**Figure D.5. Vertical Pulse, 1 m/sec² Magnitude, 10-Second Duration.**

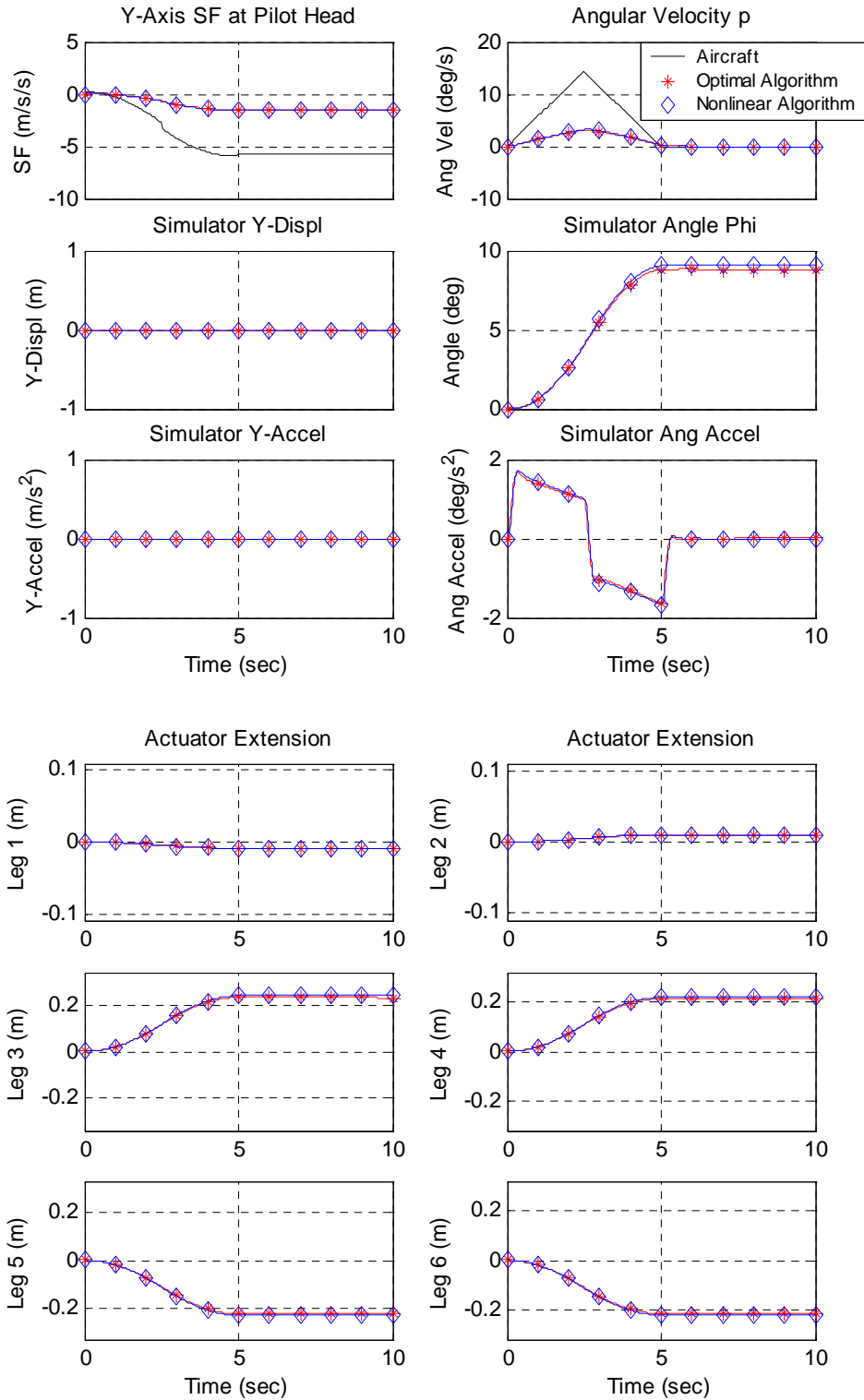**Figure D.6. Vertical Pulse, 3 m/sec² Magnitude, 10-Second Duration.**

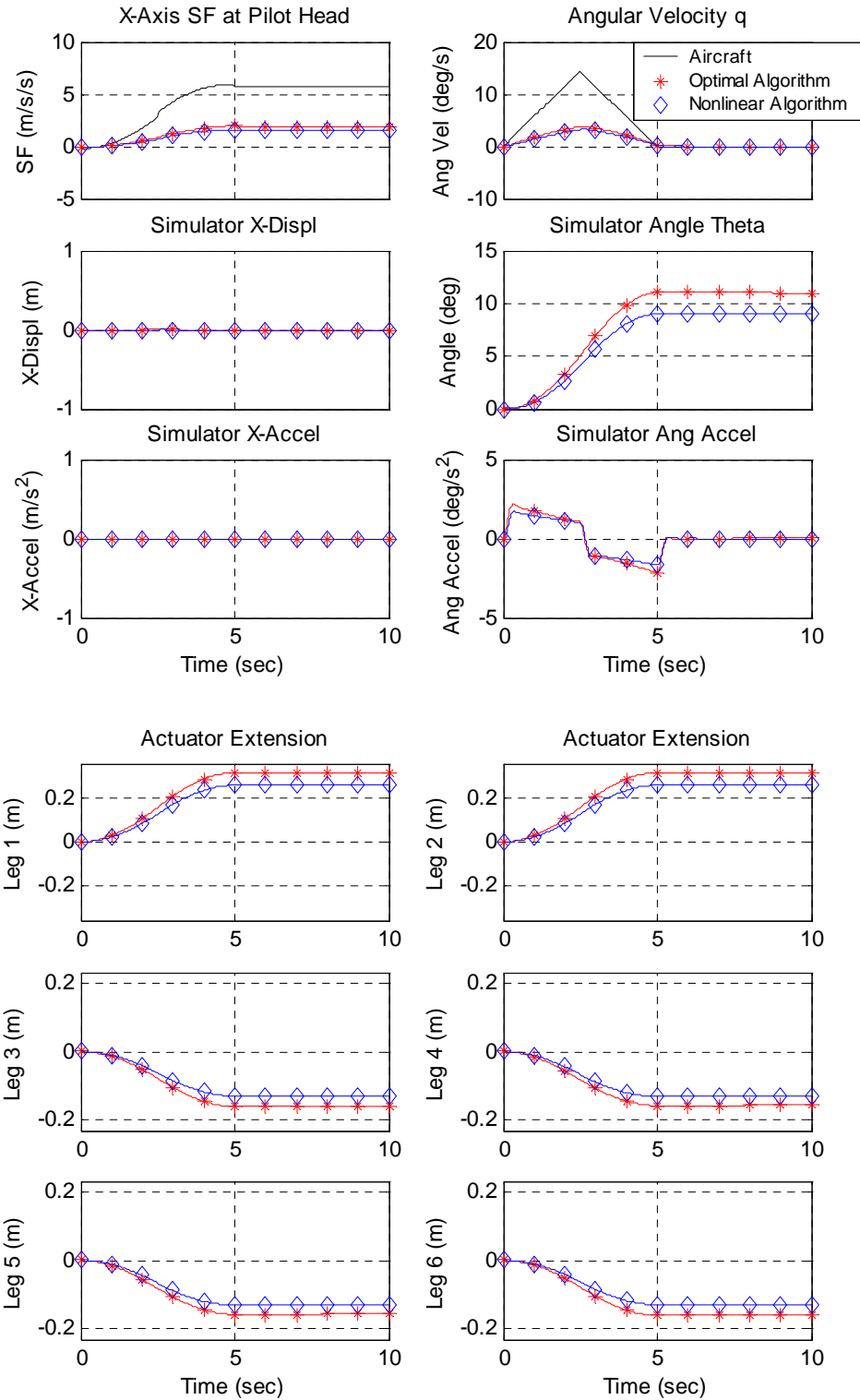**Figure D.7. Roll Doublet, 0.1 rad/sec^2 Magnitude, 5-Second Duration.**

Figure D.8. Pitch Doublet, 0.1 rad/sec^2 Magnitude, 5-Second Duration.
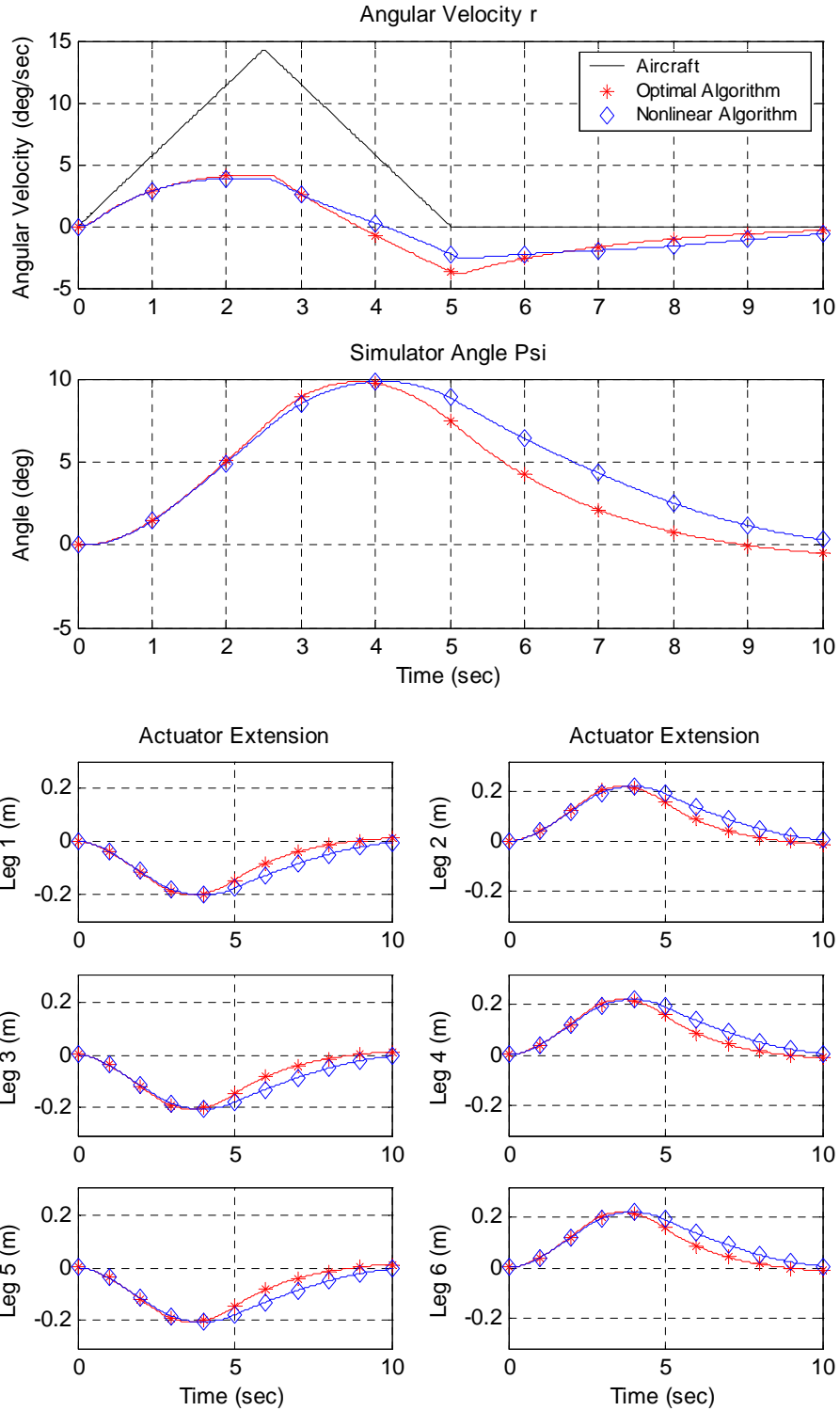
Figure D.9. Yaw Doublet, 0.1 rad/sec² Magnitude, 5-Second Duration.

This page intentionally left blank.

References

[1]   Buckingham, S.L. *Helicopter Flight Research - A Demanding Application of Piloted Simulation. International Conference on Flight Simulation of Helicopters, Proceedings of the Royal Aeronautical Society*. 1985. London.

[2]   Gundry, A.J., *Thresholds to Roll Motion in a Flight Simulator*. Journal of Aircraft, 1977. **14**(7): p. 624-631.

[3]   Scanlon, C.H., *Effect of Motion Cues During Complex Curved Approach and Landing Tasks - A Piloted Simulation Study*. 1987, Technical Paper 2773, NASA.

[4]   Schroeder, J.A., *Evaluation of Simulation Motion Fidelity Criteria in the Vertical and Directional Axes*. Journal of the American Helicopter Society, 1996. **41**(2): p. 44-57.

[5]   Hall, J.R. *Motion Versus Visual Cues in Piloted Flight Simulation. AGARD Conference Proceedings No. 249, Piloted Aircraft Environment Simulation Techniques*. 1978. Brussels, Belgium.

[6]   Wu, W., and Cardullo, F. M. *Is There an Optimum Cueing Algorithm? AIAA Modeling and Simulation Technologies Conference*. 1997. New Orleans, LA.

[7]   Martin, D.J., Jr., *A Digital Program for Motion Washout on Langley's Six-degree-of-freedom Motion Simulator*. 1977, NASA CR-145219, NASA Langley Research Center, Hampton, VA.

[8]   Sivan, R., Ish-Shalom, J., and Huang J. K., *An Optimal Control Approach to the Design of Moving Flight Simulators*. IEEE Transactions on Systems, Man, and Cybernetics, 1982. **12**(6): p. 818-827.

[9]   Reid, L.D., and Nahon, M. A, *Flight Simulation Motion-Base Drive Algorithms: Part 1 - Developing and Testing the Equations*. 1985, UTIAS Report No. 296, CN ISSN 0082-5255, Institute for Aerospace Studies, University of Toronto, Toronto, Canada.

[10]   Reid, L.D., and Nahon, M. A., *Flight Simulation Motion-Base Drive Algorithms: Part 2 - Selecting the System Parameters*. 1986, UTIAS Report No. 307, CN ISSN 0082-5255, Institute for Aerospace Studies, University of Toronto, Toronto, Canada.

[11]   Parrish, R.V., Dieudonne, J. E., and Martin, D. J., Jr., *Motion Software for a Synergistic Six-Degree-of-Freedom Motion Base*. 1973, NASA TN D-7350, NASA Langley Research Center, Hampton, VA.

[12]   Telban, R.J., Cardullo, F. M., and Houck, J. A. *Developments in Human Centered Cueing Algorithms for Control of Flight Simulator Motion Systems. AIAA Modeling and Simulation Technologies Conference*. 1999. Portland. OR.

[13]   Wu, W., *Development of Cueing Algorithm for the Control of Simulator Motion Systems*, 1997, M.S. Thesis, State University of New York at Binghamton, Binghamton, NY.

[14]   Purves, A., Fitzpatrick, Katz, LaMantia, and McNamara, *Neuroscience*. 1st ed. 1997, Sunderland, MA: Sinauer Associates.

[15]   Howard, I.P., *The Vestibular System*, in *Handbook of Perception and Human Performance, Volume I, Sensory Processes and Perception*, K.R. Boff, Kaufman, L., and Thomas, J. P, Editor, 1986, John Wiley and Sons, Inc.: New York, NY, p. 11-1 to 11-30.

[16]   Zacharias, G.L., *Motion Cue Models for Pilot-Vehicle Analysis*. 1978, AMRL-TR-78-2, Department of Defense, Alexandria, VA.

[17]   Van Egmond, A.A., Groen, J. J., and Jongkees, L. B. W., *The Mechanics of the Semicircular Canal.* Journal of Physiology, 1949. **110**: p. 1-17.

[18]   Mayne, R.A., *A Systems Concept of the Vestibular Organs*, in *Handbook of Sensory Physiology, Vestibular System*, H.H. Kornhuber, Editor, 1974, Springer-Verlag: New York, p. 493-560.

[19]   Young, L.R., and Oman, C. M., *Model for Vestibular Adaptation to Horizontal Rotation.* Aerospace Medicine, 1969. **40**(10): p. 1076-1080.

[20]   Goldberg, J.M., and Fernandez, C., *Physiology of Peripheral Neurons Innervating Semicircular Canals of the Squirrel Monkey.   II.   Response to Sinusoidal Stimulation and Dynamics of Peripheral Vestibular System.* Journal of Neurophysiology, 1971. **34**(4): p. 661-675.

[21]   Hosman, R.J., and Van der Vaart, J. C., *Vestibular Models and Thresholds of Motion Perception. Results of Tests in a Flight Simulator*. 1978, LR-265, Delft University of Technology, Department of Aerospace Engineering.

[22]   Young, L.R., *Perception of the Body in Space: Mechanisms*, in *Handbook of Physiology - The Nervous System III*, 1982, p. 1023-1066.

[23]   Fernandez, C., and Goldberg, J. M., *Physiology of Peripheral Neurons Innervating Otolith Organs of the Squirrel Units, III. Response Dynamics.* Journal of Neurophysiology, 1976. **39**(5): p. 996-1008.

[24]   Fernandez, C., and Goldberg, J. M., *Physiology of Peripheral Neurons Innervating Otolith Organs of the Squirrel Monkey, I. Response to Static Tilts and to Long-Duration Centrifugal Force.* Journal of Neurophysiology, 1976. **39**(5): p. 970-983.

[25]   Young, L.R., and Meiry, J. L., *A Revised Dynamic Otolith Model.* Aerospace Medicine, 1968. **39**(6): p. 606-608.

[26]   Ormsby, C.C., *Model of Human Dynamic Orientation*, 1974, Ph.D. Thesis, Massachusetts Institute of Technology, Cambridge, MA.

[27]   Grant, J.W., Best, W.A., and LoNigro, R., *Governing Equations of Motion for the Otolith Organs and their Response to a Step Change in Velocity of the Skull.* Journal of Biomechanical Engineering, Transactions of the ASME, 1984. **106**(4): p. 302-308.

[28]   Grant, J.W., and Best, W. A., *Mechanics of the Otolith Organ - Dynamic Response.* Annals of Biomedical Engineering, 1986. **14**: p. 241-256.

[29]   Grant, J.W., and Best, W. A., *Otolith-Organ Mechanics: Lumped Parameter Model and Dynamic Response.* Aviation, Space, and Environmental Medicine, 1987: p. 970-976.

[30]   Grant, J.W., and Best, W. A., *Viscoelastic Effects in Distributed Parameter Otolith Modeling.* ASME Applied Mechanics Division Symposia Series, 1987. **84**: p. 299-302.

[31]   Pierre, D.A., *Optimization Theory with Applications*. 1986, New York: Dover Publications.

[32]   Miller, K.S., and Ross, B., *An Introduction to the Fractional Calculus and Fractional Differential Equations*. 1993, New York: John Wiley and Sons.

[33] Hosman, R.J., *Pilot's Perception and Control of Aircraft Motions*, 1996, Ph.D. Thesis, Delft University of Technology, Delft, The Netherlands.

[34] Clark, B., and Stewart, J. D., *Effects of Angular Acceleration on Man: Thresholds for the Perception of Rotation and the Oculogyral Illusion.* Aerospace Medicine, 1969. **40**(9): p. 952-956.

[35] Clark, B., and Stewart, J. D. *Thresholds for the Perception of Angular Acceleration About the Three Major Body Axes. Fourth NASA Symposium on the Role of the Vestibular Organs in Space Exploration*. 1968. NASA SP-187.

[36] Meiry, J.L., *The Vestibular System and Human Dynamic Space Orientation*, 1965, Sc.D. Thesis, Massachusetts Institute of Technology, Cambridge, MA.

[37] Benson, A.J., Hutt, E. C. B., and Brown, S. F., *Thresholds for the Perception of Whole Body Angular Movement About a Vertical Axis.* Aviation, Space, and Environmental Medicine, 1989. **60**: p. 205-213.

[38] Benson, A.J., Spencer, M. B., and Stott, J. R. R., *Thresholds for the Detection of the Direction of Whole-Body, Linear Movement in the Horizontal Plane.* Aviation, Space, and Environmental Medicine, 1986. **57**: p. 1088-1096.

[39] Kwakernaak, H., and Sivan, R., *Linear Optimal Control Systems.* 1972, New York: John Wiley and Sons. 253-255.

[40] Arnold, W.F., and Laub, A. J., *Generalized Eigenproblem Algorithms and Software for Algebraic Riccati Equations.* Proceedings of the IEEE, 1984. **72**(12): p. 1746-1754.

[41] Brogan, W.L., *Modern Control Theory*. 3rd ed. 1991, Upper Saddle River, NJ: Prentice-Hall.

[42] Young, L.R. *Visual-Vestibular Interaction. Sixth International Symposium on Biocybernetics*. 1977. Leipzig, East Germany.

[43] Young, L.R. *Visually Induced Motion in Flight Simulation. AGARD Symposium on Flight Simulation*. 1978. Brussels, Belgium.

[44] Brandt, T., Dichgans, J., and Koenig, E., *Differential Aspects of Central Versus Peripheral Vision on Egocentric and Exocentric Perception.* Experimental Brain Research, 1973. **16**: p. 476-491.

[45] Brandt, T., Wist, E. R., and Dichgans, J., *Foreground and Background in Dynamic Spatial Orientation.* Perception & Psychophysics, 1975. **17**(5): p. 497-503.

[46] Howard, I.P., and Howard, A., *Vection: The Contributions of Absolute and Relative Motion.* Perception, 1994. **23**: p. 745-751.

[47] Held, R., Dichgans, J., and Bauer, J., *Characteristics of Moving Visual Scenes Influencing Spatial Orientation.* Vision Research, 1975. **15**: p. 357-365.

[48] Young, L.R., and Oman, C. M. *Influence of Head Position and Field on Visually Induced Motion Effects in Three Axes of Rotation. Proceedings of the 10th Annual Conference on Manual Control*. 1974.

[49] Berthoz, A., Pavard, B., and Young, L. R., *Perception of Linear Horzontal Self-Motion Induced by Peripheral Vision (Linearvection).* Experimental Brain Research, 1975. **23**: p. 471-489.

[50] Huang, J.K., and Young, L. R., *Visual Field Influence on Manual Roll and Pitch Stabilization.* Aviation, Space, and Environmental Medicine, 1988. **59**: p. 611-619.

[51] Van der Steen, H., *Self-Motion Perception*, 1998, Ph.D. Thesis, Delft University of Technology, Delft, The Netherlands.

[52] Zacharias, G.L., *Motion Sensation Dependence on Visual and Vestibular Cues*, 1977, Ph.D. Thesis, Massachusetts Institute of Technology, Cambridge, MA.

[53] Young, L.R. *On Visual-Vestibular Interaction. Fifth Symposium on the Role of the Vestibular Organs in Space Exploration*. 1970. Pensacola, FL.

[54] Borah, J., Young, L. R., and Curry, R. E., *Optimal Estimator Model for Human Spatial Orientation: Representation of Three-Dimensional Space in the Vestibular, Ocolumotor, and Visual Systems*, in *The New York Academy of Sciences*, 1988: New York, New York, p. 51-73.

[55] Hosman, R.J., and Van der Vaart, J. C. *Perception of Roll Rate from an Artificial Horizon and Peripheral Displays. 19th Annual Conference on Manual Control*. 1983. Cambridge, MA.

[56] Cardullo, F.M., and Kosut, R. L. *Old Problem/New Solutions: Motion Cuing Problems Revisited. AIAA Flight Simulation Technologies Conference*. 1983. Niagara Falls. NY.

[57] Ish-Shalom, J., *Design of Optimal Motion for Flight Simulators*, 1982, Ph. D. Thesis, Massachusetts Institute of Technology, Cambridge, MA.

[58] Anderson, B.D., and Moore, J. B., *Linear Optimal Control*. 1971, Englewood Cliffs, NJ: Prentice-Hall. 50-61.

[59] Blackburn, T.R., *Solution of the Algebraic Riccati Equation via Newton-Raphsen Iteration.* AIAA Journal, 1969. **6**(5): p. 951-953.

[60] Wang, L., and Mendel, J. M. *Structured Trainable Networks for Matrix Algebra. Proceedings of the IEEE Interntional Joint Conference on Neural Networks*. 1990.

[61] Ham, F.M., and Kostanic, I., *Principles of Neurocomputing for Science and Engineering*. 2001, New York: McGraw-Hill.

[62] Ham, F.M., and Collins, E. G. *A Neurocomputing Approach for Solving the Algebraic Matrix Riccati Equation. IEEE International Conference on Neural Networks*. 1996.

[63] Wang, J., and Wu, G., *A Multilayer Recurrent Neural Network for Solving Continuous-Time Algebraic Riccati Equations.* Neural Networks, 1998. **11**: p. 939-950.

[64] Telban, R.J., Cardullo, F. M., and Kelly, L. C., *Motion Cueing Algorithm Development: New Motion Cueing Program Implementation and Tuning*. 2005, NASA CR-2005-213746, NASA Langley Research Center, Hampton, VA.

[65] Reid, L.D., and Robinson, P. A., *Augmenting Flight Simulator Motion Response to Turbulence.* Journal of Aircraft, 1989. **27**(4): p. 306-311.

[66] Telban, R.J., Cardullo, F. M., and Kelly, L. C., *Motion Cueing Algorithm Development: Piloted Performace Testing of the Cueing Algorithms*. 2005, NASA CR-2005-213748, NASA Langley Research Center, Hampton, VA.

[67] McFarland, R.E. *Adjustable Limiting Algorithms for Robust Motion Simulation. AIAA Modeling and Simulation Technologies Conference*. 2001. Montreal, Canada.

REPORT DOCUMENTATION PAGE

1. REPORT DATE *(DD-MM-YYYY)*	2. REPORT TYPE	3. DATES COVERED *(From - To)*
01- 05 - 2005	Contractor Report	

4. TITLE AND SUBTITLE

Motion Cueing Algorithm Development: Human-Centered Linear and Nonlinear Approaches

5a. CONTRACT NUMBER

5b. GRANT NUMBER

5c. PROGRAM ELEMENT NUMBER

6. AUTHOR(S)

Telban, Robert J.; and Cardullo, Frank M.

5d. PROJECT NUMBER

L70823D

5e. TASK NUMBER

5f. WORK UNIT NUMBER

23-090-70-10

7. PERFORMING ORGANIZATION NAME(S) AND ADDRESS(ES)

State University of New York - Binghamton
Binghamton, NY 13902-6000

8. PERFORMING ORGANIZATION REPORT NUMBER

9. SPONSORING/MONITORING AGENCY NAME(S) AND ADDRESS(ES)

National Aeronautics and Space Administration
Langley Research Center
Hampton, VA 23681-2199

10. SPONSOR/MONITOR'S ACRONYM(S)

NASA

11. SPONSOR/MONITOR'S REPORT NUMBER(S)

NASA/CR-2005-213747

12. DISTRIBUTION/AVAILABILITY STATEMENT

Unclassified - Unlimited
Subject Category 54
Availability: NASA CASI (301) 621-0390

13. SUPPLEMENTARY NOTES

Prepared by the State University of New York - Binghamton for NASA Langley Research Center under subcontract to Unisys Corporation. NASA Langley Research Center Technical Monitor: Jacob A. Houck.
An electronic version can be found at http://ntrs.nasa.gov

14. ABSTRACT

While the performance of flight simulator motion system hardware has advanced substantially, the development of the motion cueing algorithm has not kept pace. Prior research identified viable features from two algorithms: the nonlinear "adaptive algorithm", and the "optimal algorithm" that incorporates human vestibular models. A novel approach to motion cueing, the "nonlinear algorithm" is introduced that combines features from both approaches. This algorithm is formulated by optimal control, and incorporates a new integrated perception model that includes both visual and vestibular sensation and the interaction between the stimuli. Using a time-varying control law, the matrix Riccati equation is updated in real time by a neurocomputing approach. The nonlinear algorithm vertical mode produced a motion cue with a time-varying washout, sustaining small cues for longer durations and washing out large cues more quickly compared to the optimal algorithm. The inclusion of the integrated perception model improved the responses to longitudinal and lateral cues. False cues observed with the NASA adaptive slgorithm were absent. The neurocomputing approach was crucial in that the number of presentations of an input vector could be reduced to meet the real time requirement without degrading the quality of the motion cues.

15. SUBJECT TERMS

Flight Simulation, Simulators, Motion Systems, Cueing Algorithms, Motion Perception

16. SECURITY CLASSIFICATION OF:			17. LIMITATION OF ABSTRACT	18. NUMBER OF PAGES	19a. NAME OF RESPONSIBLE PERSON
a. REPORT	b. ABSTRACT	c. THIS PAGE			STI Help Desk (email: help@sti.nasa.gov)
U	U	U	UU	183	19b. TELEPHONE NUMBER *(Include area code)* (301) 621-0390